Aus dem Deutschen Krebsforschungszentrum (DKFZ) Heidelberg
Wissenschaftlicher Vorstand: Prof. Dr. med. Michael Baumann
Abteilung Radiologie
Leitung: Prof. Dr. med. Dipl.-Phys. Heinz-Peter Schlemmer

Diffusion kurtosis imaging and diffusion-weighted imaging of suspicious breast and ovarian lesions: development of phantoms and optimized data evaluation routines

Inauguraldissertation
zur Erlangung des Doctor scientiarum humanarum (Dr. sc. hum.)
an der
Medizinischen Fakultät Heidelberg
der
Ruprecht-Karls-Universität

vorgelegt von
Anna Młynarska-Bujny
aus
Kattowitz, Polen
2023

Dekan: Herr Prof. Dr. med. Hans-Georg Kräusslich

Doktorvater: Herr Prof. Dr. med. Dipl.-Phys. Heinz-Peter Schlemmer

Table of Contents

List of Figures

List of Tables

Abbreviations

3D	3-Dimensional
ADC	Apparent Diffusion Coefficient
AUC	Area Under the receiver-operating characteristic Curve
CI	Confidence Interval
CV	Coefficient of Variation
D_{app}	Apparent Diffusion Coefficient derived from diffusion kurtosis imaging
$D_1 - D_5$	Apparent Diffusion Coefficients derived from different fitting methods
DCE	Dynamic Contrast-Enhanced
DKI	Diffusion Kurtosis Imaging
DWI	Diffusion-Weighted Imaging
EPI	Echo-Planar Imaging
FOV	Field Of View
GRAPPA	Generalized Autocalibrating Partially Parallel Acquisition
K_{app}	Apparent Kurtosis Coefficient
$K_2 - K_5$	Apparent Kurtosis Coefficients derived from different fitting methods
MITK	Medical Image Interaction Toolkit
MRI	Magnetic Resonance Imaging
RESOLVE	Read-Out Segmented Echo-Planar Imaging
ROC	Receiver-Operating Characteristic
ROI	Region Of Interest
SPAIR	Spectral Attenuated Inversion Recovery
SS-EPI	Single-Shot Echo-Planar Imaging
TE	Echo Time
TR	Repetition Time

1 Introduction

Diffusion is a process of the random motion of the molecules, which depends on their thermal energy. In the human body, the molecular diffusion can be measured by diffusion-weighted imaging (DWI), which is a specialized acquisition scheme of magnetic resonance imaging (MRI). Within the tissue microenvironment, the water molecules are in a constant motion and interact with cell walls and other cellular compartments. In general, the higher the degree of cellularity of the tissue, the more restricted the diffusion. Thus, cancerous tissue, hypercellular metastases, and fibrosis are usually manifested by impeded diffusion in comparison to the healthy tissue (Malayeri et al. 2011). Conversely, damaged cell membranes and lower degree of cellularity of the tissue facilitate the water molecules to move more freely (Qayyum 2009). Therefore, DWI is a useful method for visualization of the pathological states of the tissue, which are often manifested by alterations in water diffusion (Woodhams et al. 2011). For conventional DWI sequences, the restrictions in the Brownian motion of the water molecules in the tissue can be estimated quantitatively by the apparent diffusion coefficient (*ADC*) derived from the signal intensity in the diffusion-weighted images.

One of the first clinical applications of DWI was diagnosis of neurologic diseases, primarily acute brain ischemia. After the onset of an ischemic stroke, the brain cells start to swell due to the cell membrane damages and accumulation of intracellular fluid. The observed decrease in the *ADC* with concomitant bright signal on diffusion-weighted images was linked to the cytotoxic edema causing restrictions of interstitial flow, and reduction in extracellular volume due to the increase in intracellular volume (van Everdingen et al. 1998). While cell swelling cannot fully explain the changes in *ADC*, membrane permeability changes are also likely to contribute. In the field of oncology, DWI gains increasing interest in applications like lesion detection, differentiation between benignancy and malignancy, or cancer treatment response surveillance (Hedayati et al. 2014).

In order to visualize the tumor tissue, the alteration in water diffusion is often used as a distinctive feature, as tumor tissue is characterized by higher cellularity that restricts the movement of water molecules due to the limited intercellular space. DWI was reported as a promising tool for imaging and evaluation of lesions in an area of the body including brain, head and neck, breast, liver, pancreas, prostate, female pelvis, like also for whole-body imaging in patients with lymphoma (Hedayati et al. 2014; Iima and Le Bihan 2016; Messina et al. 2020).

Technical improvements in DWI acquisition allowed a development of more advanced imaging techniques. One of them is diffusion tensor imaging, enabling the quantitative assessment of diffusion anisotropy in the tissue with organized structure like brain white matter or muscles (Mori and van Zijl 2002), in which water diffusion occurs more preferentially along the fibers long axis and is hindered in the perpendicular direction. Another advanced method is intravoxel incoherent motion (IVIM) imaging. IVIM quantifies the diffusion of water molecules as well as microcirculation of blood in the randomly oriented capillaries, leading to a faster signal drop due to intravoxel dephasing as a result of this pseudo-diffusion process (Bihan et al. 1988). However, the additional signal attenuation due to perfusion can be observed only using very low diffusion weightings (Iima and Le Bihan 2016). In contrast, the application of high diffusion weightings in diffusion kurtosis imaging (DKI) enables assessment of the non-Gaussian diffusion, which occurs in the tissue due to the presence of barriers and obstacles, e.g., cell membranes (Jensen and Helpern 2010).

This dissertation focusses on applications of DWI and DKI for characterization of suspicious breast findings and sonographically indeterminate ovarian lesions. In the context of the breast DWI, the special attention was paid to phantoms for quality control of the quantitative parameters derived from diffusion weighted images.

2 Fundamentals

2.1 Basic Concepts of Magnetic Resonance Imaging

The principle of MRI is based on the use of the natural magnetic properties of biological tissues. The human body is composed mostly of water. Therefore, the clinical MRI uses primarily the signal emitted by the excited hydrogen nuclei. In the presence of the strong magnetic field inside the scanner, the excited proton spins forming the macroscopic magnetization precesses about the field direction with the Larmor frequency proportional to the strength of this external field, that is:

$$\omega_0 = \gamma B_0, \tag{2.1}$$

where γ is a gyromagnetic ratio and B_0 is a static magnetic field. To simplify the description of the spin motion, a concept of the rotating frame of reference is used, with coordinate system precessing with the same frequency ω_0 about the direction of field B_0. This transformation results in stationary net magnetization in the rotating frame of reference.

In the clinical routine, the most commonly used MRI technique is two-dimensional imaging, based on the two-dimensional Fourier transformation (Martí-Bonmatí 2002). To obtain a series of cross-sectional images of the body, three gradients in orthogonal directions are applied. The first linear gradient is used for slice selection. An application of a radiofrequency (RF) pulse of selected bandwidth causes rotation of the magnetization in the corresponding slice. The precession of the transverse magnetization generates the signal in the coil. The position of the spins in the selected slice is encoded by the phase and frequency encoding gradients. The acquired signal is stored in a raw data matrix called *k*-space. To reconstruct an image, an inverse Fourier transform of the *k*-space data is performed.

In general, the strength of the measured signal depends on two time constants, T_1 and T_2, which are distinctive for each tissue type. The longitudinal relaxation time T_1, connected with the release of energy to the atomic neighborhood, characterizes the regrowth of the magnetization along the direction of the external static magnetic field. T_2 refers to the dephasing of the spins caused by their mutual influence leading to the local changes in the magnetic field, and therefore to the changes in the local Larmor frequencies. The third characteristic tissue parameter is the spin density, which refers to the number of protons contained in the image voxel. Using the spin-echo sequence, which is one of the fundamental MRI pulse sequences, the signal intensity can be described by the following expression:

$$S = k\rho\left(1 - e^{-\frac{TR}{T_1}}\right) \cdot e^{-\frac{TE}{T_2}} \tag{2.2}$$

where k is a proportionality constant, ρ is a proton density, T_1 is the longitudinal relaxation time, T_2 is the 'spin-spin' relaxation time, TR is a repetition time, and TE echo time. By adjusting the value of *TR* and *TE*, different types of image contrast can be achieved. Whereas the choice of TR controls the relaxation of the longitudinal magnetization and therefore the degree of T_1-weighting in the image, *TE* controls the degree of T_2-weighting. To obtain T_1-weighted image, short *TR* and short *TE* are chosen, which minimizes the T_2-weighting. In contrast, T_2-weigted image requires long *TR* and long *TE*, which gives a strong recovery of the longitudinal magnetization. ρ-weighted image can obtained by using long *TR* and short *TE*, when the impact of both T_1 and T_2 relaxation time is considerably reduced. The following Section 2.2 presents more detailed description of the spin-echo sequence used in DWI. For more details about fundamental theory of MRI, please refer to (Bernstein et al. 2004) or (E. Mark Haacke 1999).

2.2 Principles of Diffusion-Weighted Imaging

DWI is a specialized acquisition scheme of MRI based on the measurements of the Brownian motion of the water molecules. In DWI a pair of gradient pulses is applied to visualize the impact of diffusion restrictions. If the molecules diffuse in the time interval between the two gradients then the spins will not fully rephrase and a signal loss will be observed. However, if on the way of the diffusing molecule numerous obstacles are present, the diffusing molecules will get trapped between the barriers. The resulting smaller diffusion distance will lead to less signal loss compared to free diffusion. Figure 1 shows a scheme of a diffusion-weighted spin-echo sequence which is currently the most widespread sequence used in diffusion measurements. In the MRI scanner, the spins are aligning with the static magnetic field, which creates net magnetization. The DWI spin-echo sequence starts with a 90° radiofrequency (RF) pulse which flips longitudinal magnetization and produces transversal magnetization. This is done because only transversal magnetization can be measured. Then the first diffusion gradient dephases the spins. By applying the 180° refocusing RF pulse the phases of spin packets are inverted and a spin echo is generated. Subsequently, the second diffusion gradient with the same strength as the first one rephases the spins. However, the molecules are moving in the time interval between the diffusion-weighting gradients due to Brownian motion and the spins are not fully rephased and therefore a signal loss is observed. The diffusion weighting depends on the time interval between the application of the two sensitizing gradients (Δ), their duration (δ) and strength (G). Usually, the amount of diffusion weighting is controlled by the gradient strength which ensures the same echo time for different diffusion weightings so that the influence of T_2-relaxation remains the same (Mori 2007).

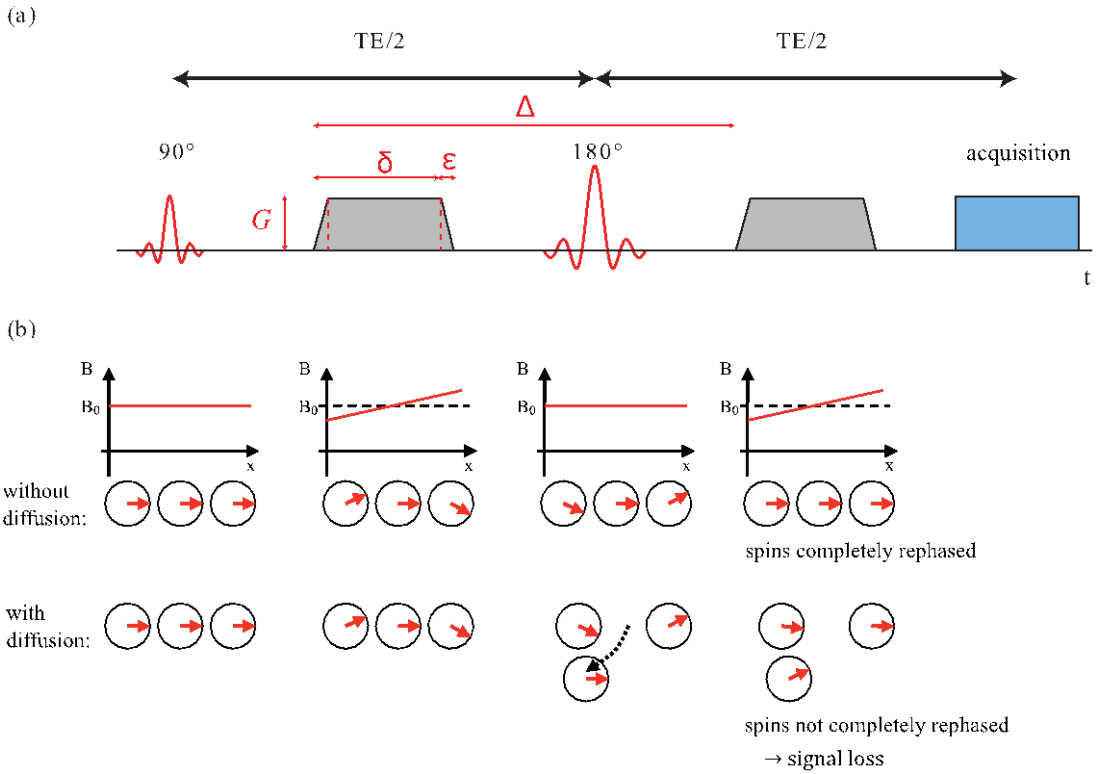

Figure 1. (a) Simplified pulse diagram of the diffusion-weighted spin echo sequence. G denotes the amplitude of the diffusion gradients, δ their duration, ε rise time, and Δ the delay time between the diffusion gradients. (b) Schematic spatial dependence of the magnetic moment, depicted by the red arrows (second and third row). The first row shows the corresponding local magnetic field. When 90° excitation pulse is applied, the magnetic moment is tipped away by a 90° flip angle from longitudinal into transverse plane. The first diffusion gradient dephases the spins according to their location along the gradient direction. Next, the 180° refocusing pulse is applied at *TE*/2, which inverts the magnetization to regain the coherence of the spin isochromats lost due to the magnetic field inhomogeneities and susceptibility effects. The second diffusion gradient rephases the spins. At echo time the signal is acquired. However, if the spins have changed their position and moved in the time interval between the application of the two diffusion gradients, the second gradient does not fully rephrase the spins, and therefore the measured signal is a signal of smaller magnitude. Spatial encoding steps are not included in this pulse diagram. Adapted with permission from (Kuder 2014).

For free diffusion, the probability that a molecule moves from the initial point ($x = 0$) to another location x in one dimension in a given time interval t is described by diffusion propagator which follows a Gaussian distribution:

$$P(x,t) = \frac{1}{\sqrt{4\pi Dt}} e^{-\frac{x^2}{4Dt}}, \tag{2.3}$$

where $\sqrt{2Dt}$ is the average diffusion distance in one dimension and D is diffusion constant. The intensity of the diffusion-weighted signal is represented by a mono-exponential equation:

$$S = S_0 e^{-bD}, \tag{2.4}$$

which can be transformed into the logarithmic form as follows:

$$\ln(S) = \ln(S_0) - bD. \tag{2.5}$$

In Equations (2.4) and (2.5) S is a diffusion-weighted signal, S_0 is a signal without diffusion-weighting, and b is a sensitizing factor called *b*-value. For trapezoidal diffusion gradient, like the one depicted in Figure 1, *b*-value can be expressed as:

$$b = \gamma^2 G^2 \left(\delta^2 \left(\Delta - \frac{\delta}{3} \right) + \frac{\varepsilon^3}{30} - \frac{\delta \varepsilon^2}{6} \right), \tag{2.6}$$

where γ is a gyromagnetic ratio, which for hydrogen nucleus equals $26.8 \cdot 10^8 \frac{\mathrm{T}}{\mathrm{s}}$, G is the gradient amplitude, δ is the gradient duration, and Δ is the time interval between the diffusion-sensitizing gradients.

For rectangular diffusion gradient the expression for *b*-value takes a form:

$$b = \gamma^2 G^2 \delta^2 \left(\Delta - \frac{\delta}{3} \right). \tag{2.7}$$

In general, the signal intensity of the diffusion-weighted image, obtained using a spin-echo sequence, is given by equation:

$$S = k\rho \left(1 - e^{-\frac{TR}{T_1}} \right) \cdot e^{-\frac{TE}{T_2}} \cdot e^{-bD}, \tag{2.8}$$

where k is a proportionality constant, ρ is a proton density, T_1 is the longitudinal relaxation time, T_2 is the 'spin-spin' relaxation time.

Usually the amount of diffusion weighting is controlled by the gradient strength which ensures the same echo time and results in signal loss being influenced only by diffusion process and free of T_1- and T_2-weighting (Mori 2007).

In principle, in the clinical practice, free diffusion in MRI can be observed only for a phantom filled with a homogeneous liquid solution. In biological tissue, the random motion of water molecules is restricted due to the presence of natural barriers and compartments, mainly assignable to cell membranes (Stieltjes et al. 2013). Moreover, tumor tissue is characterized by higher cellularity than normal tissue and therefore diffusion is in principle more hindered in tumors (Woodhams et al. 2011). The motion of water molecules, affected by the local tissue environment, is reflected by signal intensity in diffusion-weighted images. High cellular density is manifested by more restricted diffusion and weaker signal attenuation as in the tissue with low cellular density. Although the diffusion in the biological tissue is not free, if *b*-values in the intermediate range are used for in vivo measurements, signal decay can be

still well enough represented by a mono-exponential function (Partridge et al. 2017). However, the coefficient obtained by fitting the mono-exponential function to the measured diffusion-weighted signal is only an estimate and therefore is called *apparent diffusion coefficient* (*ADC*). As a rule, the *ADC* values measured in malignant tumors are lower than *ADC* measured in the benign tumors or normal tissue (Zhou et al. 2019). However, there is an overlap in these values (Partridge and McDonald 2013) .

2.3 Principles of Diffusion Kurtosis Imaging

Whereas conventional DWI assumes that the molecular displacement probability function follows the normal distribution, DKI takes into account that the complex structure of the tissue may result in non-Gaussian water diffusion. When imaging the human body using higher diffusion weightings, an increasing deviation from the mono-exponential signal decay can be observed. The deviation of the diffusion propagator from the Gaussian distribution can be measured by the kurtosis.

In statistics, the excess kurtosis is defined as the normalized fourth moment minus 3:

$$E\left[\left(\frac{X-\mu}{\sigma}\right)^4\right] - 3 = \frac{E[(X-\mu)^4]}{(E[(X-\mu)^2])^2} - 3 = \frac{\mu_4}{\sigma^2} - 3, \tag{2.9}$$

where X is a random variable, μ the mean value, μ_4 the fourth central moment and σ the standard deviation. E denotes the expectation value operator. In DKI, the considered random variable is the particle displacement during the diffusion time.

In the literature about DKI the term *excess kurtosis* is usually shortened to *kurtosis*. Therefore, from here on in this work, to be consistent with the terminology used in other publications, diffusional kurtosis will be defined as described by the Equation (2.10). In terms of diffusion-weighted MRI, the diffusional kurtosis has to be defined along the particular gradient direction used for the measurement which is denoted here by the normalized gradient vector:

$$K(t) = \frac{\langle(\boldsymbol{n}\cdot\boldsymbol{x}(t))^4\rangle}{\langle(\boldsymbol{n}\cdot\boldsymbol{x}(t))^2\rangle^2} - 3, \tag{2.10}$$

where $\boldsymbol{x}$ denotes the particle displacement during the diffusion time t (Jensen et al. 2005; Lu et al. 2006). The angled brackets symbolize the averaging over all possible random trajectories in the confining geometry.

In general, for free diffusion, described by a Gaussian probability distribution, $K = 0$ is valid. In contrast, for restricted diffusion, at least some of the molecules get partially trapped and travel less far leading to deviations from the free Gaussian diffusion and thus $K \neq 0$.

While both positive and negative values are in general possible, only $K > 0$ has been observed in biological tissue.

To measure the approximation of diffusional kurtosis, the standard sequence as presented in Figure 1 can be used. The method of quantification of non-Gaussian diffusion presented by Jensen et al. (2005) is based on a Taylor expansion of the natural logarithm of the measured signal in powers of *b*, the so-called cumulant expansion, which up to the first three terms is given by expression:

$$\ln(S) = \ln(S_0) - bD_{\text{app}} + \frac{1}{6}b^2 D_{\text{app}}^2 K_{\text{app}} + O(b^3), \tag{2.11}$$

where S is the diffusion-weighted signal, S_0 is the signal without diffusion-weighting, b is the *b*-value, D_{app} is the apparent diffusion coefficient corrected for the kurtosis effect and K_{app} in the apparent diffusional kurtosis. Again, it should be noted that the measured kurtosis K_{app} in the equation above deviates from the true kurtosis of the propagator which leads to the additional term "apparent".

Based on this approach, the signal decay in DKI can be described by the following equation (Jensen and Helpern 2010):

$$S(b) = S_0\, e^{-bD_{\text{app}} + \frac{1}{6}b^2 D_{\text{app}}^2 K_{\text{app}}}. \tag{2.12}$$

Taking the plot of the logarithmized signal intensity against various *b*-values, to capture the deviation from the straight line characteristic for free diffusion and obtain the value of diffusional kurtosis parameter, requires higher *b*-values than usually used in DWI (Jensen and Helpern 2010). Whereas for small *b*-values the b^2-term is negligible, its influence becomes increasingly dominant with higher *b*-values (Stieltjes et al. 2013).

Figure 2 visualizes the additional information that may be contained in the kurtosis coefficient using diffusion propagator for free diffusion and restricted diffusion, displayed as schematic examples; the lower row sketches the corresponding plots of signal decay on the semi-logarithmic scale. The *ADC* value measured in a liquid with a high viscosity (Figure 2a) is smaller than *ADC* measured in liquid with a low viscosity (Figure 2b). In both cases of free diffusion the kurtosis value equals zero. For restricted diffusion (Figure 2c) the *ADC* value is also reduced, but the kurtosis is greater than zero. Based only on *ADC* values we cannot distinguish between (b) and (c), but this is possible using the apparent kurtosis coefficient so that the kurtosis may contain in principle additional independent information.

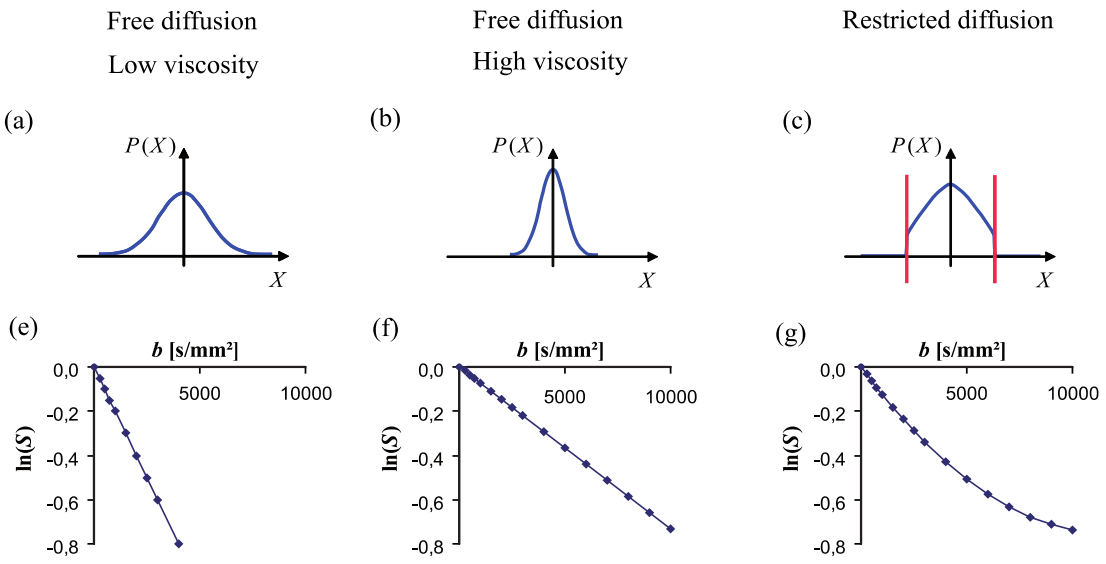

Figure 2. Schematic representation of Gaussian diffusion propagator for free diffusion in low (a) and high viscous liquid (b) and non-Gaussian diffusion propagator for restricted diffusion (c); corresponding scheme of the semi-logarithmic plot of the signal attenuation presented below (e-g). Higher viscosity results in lower diffusion coefficient, depicted as a slope (f), in comparison to lower viscosity (e). In this both cases of free diffusion diffusional kurtosis equals zero. In the case of the hindered diffusion, due to the presence of the obstacles, the diffusion coefficient is also reduced, but the kurtosis coefficient is non-zero, which is depicted by the plot curvature at the higher *b*-values (g). Adapted with permission from (Kuder 2014).

2.4 Noise Correction in Diffusion Kurtosis Imaging

The assessment of the quality of the acquired magnetic resonance image and quantification of the MRI system performance is often based on the estimation of the ratio of the true signal to the level of the background noise, known as the signal-to-noise ratio (SNR). As suggested in the work by Dietrich et al. (2001), the diagnostic quality of the quantitative parameters derived by diffusion-weighted MRI is contingent on the level of SNR. Hereinto, high diffusion weighting and prolonged echo time in DKI cause the decrease in the signal intensity and therefore result in a lower SNR of an image. Since for DWI, always magnitude images are evaluated and – in the case of averaging – the magnitude is first calculated before averaging, the signal noise will lead to a bias in the magnitude signal. This noise-induced bias, especially relevant for low SNR values, may distort the kurtosis coefficient obtained by the fitting Equation (2.12) to the measured signal $S(b)$.

It was reported that in the presence of noise the signal intensity in the magnitude images follows the Rician distribution (Gudbjartsson and Patz 1995). Taking into account that for SNR ≥ 3 a Gaussian distribution can be used as an approximation of the Rician distribution, Gudbjartsson and Patz (1995) suggested a correction approach to mitigate the bias arising from background noise in the signal of magnitude:

$$A = \sqrt{|M^2 - \sigma^2|}, \tag{2.13}$$

where A is an estimation of the noiseless signal intensity, M is the measured signal intensity and σ is the standard deviation of the Gaussian noise.

Based on this approach, Jensen et al. (2005) published a modified formula for estimation of *DKI*-derived parameters which accounts for the background noise, which is more accurate for very low *SNR*:

$$S(b) = \sqrt{\left(S_0\, e^{-bD_{\mathrm{app}}+\frac{1}{6}b^2 D_{\mathrm{app}}^2 K_{\mathrm{app}}}\right)^2 + \eta^2}, \tag{2.14}$$

where D_{app} is the apparent diffusion coefficient, K_{app} is the apparent diffusional kurtosis and η is the background noise level, estimated by calculating the mean signal intensity in the air outside the human body.

For high *b*-values, fitting of the diffusion kurtosis equation without this correction may result an overestimation of the kurtosis, especially in regions with high diffusion coefficients, where the signal already drops to the noise level at relatively low *b*-values.

2.5 Intravoxel Incoherent Motion

In biological tissue in the low *b*-value regime, the signal decay is more rapid at very low *b*-values as it would be expected from the mono-exponential equation. This additional signal attenuation is caused by perfusion, that is blood microcirculation in the randomly oriented capillaries building a network. The signal decay caused by perfusion depends on the velocity of blood flowing in the capillary segments and the geometry of the capillaries (Bihan et al. 1988). The term "Intravoxel incoherent motion (IVIM)" covers both perfusion and molecular diffusion of water. The signal decay is given by the following equation:

$$\frac{S}{S_0} = f_{\mathrm{IVIM}} e^{-b(D^* + D_{\mathrm{blood}})} + (1 - f_{\mathrm{IVIM}}) e^{-bD_{\mathrm{tissue}}}, \tag{2.15}$$

where f_{IVIM} is the signal fraction of the blood flowing in the capillaries, D^* is the pseudo-diffusion coefficient related to the blood flow in capillaries, D_{blood} is the diffusion coefficient measured in blood, D_{tissue} is diffusion coefficient measured in tissue. Taking into account that pseudo-diffusion coefficient D^* is approximately 10 times greater than tissue diffusion coefficient D, the blood microcirculation contributes substantially only in low *b*-value regime to the signal decay driven by diffusion; above a particular *b*-value threshold, the contribution of the capillary blood compartment is negligible.

2.6 Technical Aspects of Selected Pulse Sequences

The most common method used for DWI is echo-planar imaging (EPI), characterized by extremely fast acquisition time due to the possible sampling the data for image reconstruction by only one RF pulse. Rapidly switched frequency-encoding gradients with alternating polarity produce the gradient echo train. Each gradient echo is assigned to individual *k*-space line according to the phase-encoding gradient. The advantage of the short acquisition time of 50–100 ms (Stehling et al. 1991) is a reduction of errors induced by physiologic motion (Bammer 2003). Especially single-shot techniques solve the problem of phase instabilities between k-space lines induced by the strong weighting of the diffusion gradients on translational motion. On the other hand, the imperfections during the fast switching of the frequency-encoding gradient polarity and the long echo train makes EPI prone to artifacts such as ghosting and various off-resonance effects. Single-shot EPI images exhibits often high temporal resolution at the cost of limited spatial resolution and small SNR (Bernstein et al. 2004). Moreover, fat suppression techniques are needed to reduce the chemical shift artifacts, appearing in the phase-encoding direction (Bushong and Clarke 2015).

To improve the image quality, DWI-EPI can be combined with parallel imaging techniques (Bammer 2003) which reduce the needed number of phase-encoding steps and decrease the echo train length. One method using reconstruction in image space domain is SENSitivity Encoding (SENSE). In SENSE, each coil element acquires a different image using a reduced field of view and afterwards the signals are merged according to the coil sensitivity information (Blaimer et al. 2004). In the second method, named GeneRalized Autocalibrating Partially Parallel Acquisitions (GRAPPA), the reconstruction is done in *k*-space domain. The missing *k*-space lines are calculated for each coil element before the Fourier transformation. Due to the acqusition of additional autocalibration lines, the GRAPPA is more resistant to severe EPI distortions than SENSE (Griswold et al. 2002). Another form of the EPI sequence is read-out segmented EPI where the *k*-space is divided into several segments along the frequency-encoding direction. The data from the subsequent fractions of *k*-space is acquired in the separate RF excitations to reduce the susceptibility artifacts and spatial blurring caused by T2* signal decay (Porter and Heidemann 2009). However, the readout segments distributed over several TR, in comparison to single-shot EPI, result in higher sensitivity to motion-induced artifacts. To mitigate this problem, additional navigator data acquired from the central part of each *k*-space segment are used for phase correction.

Another technical aspect worth mentioning is the utilization of bipolar and monopolar gradients. High amplitude and fast slew rate of diffusion gradients make diffusion weighted images prone to eddy current artifacts (Alexander et al. 1997). Rapid switching of diffusion gradient pulses induces current in conducting surfaces of the MR scanner. This results in eddy-current-induced gradients which distort the shape of diffusion gradient pulses (Le Bihan et al. 2006). To mitigate this problem, the bipolar gradients may be applied, thus each unipolar

diffusion gradient is split into two bipolar gradients by a refocusing pulse (Reese et al. 1998). Therefore, in the sequence with bipolar gradients, two 180° refocusing pulses are used instead of one in a sequence with monopolar diffusion gradients.

2.7 Fat Suppression Techniques

Free water protons resonate at a different frequency than hydrogen protons contained in fat molecules, which results in a chemical shift. The difference in resonance frequency is 3.35 ppm for the dominant groups of fat molecules. The ppm scale is a ratio of frequency difference between two measured peaks to the frequency of a particular peak, multiplied by 1 million. It means that in the static magnetic field $B_0 = 1.5$ T, free fat protons resonate at a frequency 214 Hz lower than free water protons. For $B_0 = 3$ T, the frequency is shifted down by 447 Hz. This discrepancy in resonance frequency relates to variation in a local magnetic field between protons in water and protons in a compound that contains fat or lipids caused by different configurations of electrons in these molecules (E. Mark Haacke 1999). Moreover, in comparison to other tissues, fat has a short T_1 time and therefore, in measurements with short TR, the signal from fat can significantly exceed the measured signal from water. Furthermore, the fat spectral peak is broader than the water spectral peak because in fat there are various types of chemical bonds with hydrogen whereas in water there is only one type of chemical bond. Approximately 80% of the MRI signal measured in white fat is coming from protons in lipids whereas almost 20% from hydrogen protons from water in loose connective tissue (Delfaut et al. 1999). Selected fat suppression techniques which are used to reduce the chemical shift artifacts, are described below.

Spectral fat saturation is a technique in which a frequency-selective RF pulse is applied to saturate the magnetization of fat protons. First, the fat saturation pulse of the frequency corresponding to resonance frequency of the lipids is applied and the generated transverse magnetization is dephased. After a short period of time during which the longitudinal fat magnetization has not regrown, the slice-selective excitation RF pulse is applied. As a result, only water longitudinal magnetization is tipped into the transverse plane and only signal from water is measured. However, the method is sensitive to inhomogeneities of the main magnetic field caused by susceptibility differences which induce shifts in resonance frequencies. As a result of the frequency discrepancies, the saturation pulse may not reflect the lipid resonance frequency or it may cause the saturation of water signal instead of fat signal (Delfaut et al. 1999).

The short inversion time (TI) inversion-recovery sequence, termed with the acronym STIR, uses the differences in T_1 relaxation time between the adipose tissue and water. At first, the longitudinal magnetization of water and fat is inverted. During succeeding recovery, the RF pulse is applied at the time-point when the fat longitudinal magnetization is crossing zero. It results in nulling the fat signal and collecting only the water signal which – for short inver-

sion time – remains large and negative due to the long T_1 of water in comparison to T_1 of fat. STIR is insensitive to magnetic field inhomogeneities. However, it results in the overall signal loss and a low signal-to-noise ratio, because at TI_{null} the longitudinal magnetization of water components is below the equilibrium value. Further, TR has to be usually prolonged. Moreover, STIR suppresses the signal not only from fat but from all tissues with T_1 equal to T_1 of fat.

Spectral Adiabatic Inversion Recovery (SPAIR) is a technique which uses a spectrally selective adiabatic inversion pulse to invert the fat longitudinal magnetization only. The advantage of adiabatic pulses is the fact that they are relatively insensitive to B_0 and B_1 variations. Due to the modulation of the amplitude and phase, the adiabatic inversion pulse is able to perfectly invert the magnetization across the slice (E. Mark Haacke 1999). Similar to STIR, an excitation pulse is applied at the moment when the fat longitudinal magnetization is crossing zero. However, due to the application of spectrally selective adiabatic inversion pulse, only fat signal is suppressed and therefore SPAIR is characterized by higher SNR than STIR. It is, however, less robust in the presence of field inhomogeneities.

In DW-EPI the chemical shift will predominantly appear in phase encoding direction. During single-shot EPI, all lines of k-space are sampled after a single 90° RF excitation pulse and a succeeding 180° RF pulse which results in rephasing of the spins and formation of a spin echo. Due to the resulting long echo train, phase errors originating form chemical shift accumulate and lead to a large shift in phase direction.

3 Aim of the Dissertation

This dissertation is focused on the potential applications of DWI and DKI in characterization of suspicious breast and ovarian lesions. To investigate the ability of the quantitative parameters, derived from the different signal representations, to differentiate between benign and malignant lesions, the following objectives were addressed in three studies:

- To start with, *ADC* is currently the most commonly used quantitative parameter in the diffusion MRI of the breast, performed for characterization of ambiguous lesions revealed on X-ray mammography. The main challenge is the wide spread of *ADC* thresholds reported in numerous publications which is in part due to the differences in the imaging protocol settings, MRI machines and equipment as well as different patient groups. Therefore, to ensure the accuracy of the estimated quantitative parameters, quality control is needed. Till now, several authors proposed various phantom designs for quantitative breast MRI. Nonetheless, there remains a deficiency in a low-cost and easy-to-use breast phantom dedicated for simultaneous *ADC* measurements in the left and right coil side, which would take into account also the *ADC* dependency on the temperature. Therefore a simplified, inexpensive and adjustable breast phantom was constructed and tested for better quality control of the *ADC* measurements.
- Secondly, if applying a stronger maximal diffusion weighting than in a standard DWI, diffusion kurtosis imaging is possible. DKI delivers the second complementary quantitative parameter – the diffusional kurtosis – which describes the degree of the non-Gaussian diffusion. The kurtosis parameter reflects more specifically the microstructure of the tissue, its heterogeneity and determines the presence of barriers restricting the diffusion. However, signal acquired at higher *b*-values is more susceptible to the influence of noise. Moreover, for breast DKI, due to the high content of adipose tissue, effective fat suppression is essential. If not achieved, the residual fat signal may potentially corrupt the signal in the lesion area, which as a result may cause an overestimation of the kurtosis parameter. To overcome this problem, various signal fitting models were proposed and analyzed in terms of the ability to differentiate between benign and malignant breast lesions.
- Lastly, in contrast to breast DKI, which gains on the popularity, DKI of ovarian lesions still remains almost unexplored. Therefore the aim was to evaluate the performance of DKI in the characterization of ovarian lesions.

The following Sections 3.1–3.3 describe in greater detail the objectives mentioned above and explain the motivation for this work.

3.1 Part I – Spatial and Temporal Variability of *ADC*

According to the report published by the International Agency for Research on Cancer (IARC), breast cancer is, at the same time, the most frequently diagnosed cancer and the leading cause of cancer-related death among women (Bray et al. 2018). Despite of the benefits, X-ray mammography screening programs result in a substantial number of false-positive findings (Stout et al. 2014). Herein about 50% of the women that are referred for biopsy because of the concern that the lesion detected on primary X-ray mammography screening might be of malignant nature, are diagnosed with a benign breast disease eventually (Kooperationsgemeinschaft Mammographie 2019). Breast MRI has been demonstrated in multiple studies to be more sensitive in the detection of breast cancer than X-ray mammography, especially in women with dense breast (Bakker et al. 2019; Comstock et al. 2020). Abbreviated MRI protocols, incorporating contrast-enhanced sequence, have shown high efficiency in characterization of breast lesions (Mann et al. 2019). However, facing increasing concerns about possible deposition of gadolinium in the body after administration of the linear and macrocylic gadolinium-based contrast agents (Murata et al. 2016; Radbruch et al. 2015), contrast agent-free diagnostic alternatives are warranted. In this context, DWI is gaining more and more interest as a contrast-free imaging modality either as a primary tool for detection of suspicious findings, or as an adjunct complementary method to characterize lesions detected by other screening methods, e.g. X-ray mammography. Besides, dynamic contrast-enhanced MRI (DCE MRI) is associated with high cost and long examination time (Amornsiripanitch et al. 2019). Therefore, incorporating a diffusion-weighted sequence instead of DCE into the MRI breast screening protocol should to be profitable also from the economical point of view.

Currently, breast DWI is mainly used as an additional sequence to the dynamic contrast-enhanced MRI (DCE MRI) to reduce the number of false positive findings (Partridge et al. 2017) and therefore to minimize the number of unnecessary biopsies of benign lesions. DWI for breast imaging is characterized by high specificity, however the sensitivity reported in many studies is lower than sensitivity of DCE MRI, although in comparison to mammography or ultrasound an enhancement in performance can be observed (Amornsiripanitch et al. 2019; Baltzer et al. 2019a). Nonetheless, the results of two large meta-analyses show the potential of breast DWI as a standalone sequence and demonstrate sensitivity comparable to the one achieved by DCE MRI (Baxter et al. 2019; Zhang et al. 2016). Moreover, a study by Bickelhaupt et al. (2016) showed that using the imaging technique based on DWI enhances correct classification of malignant lesions among women with suspicious mammogram result. The most commonly used quantitative parameter for analysis of diffusion-weighted data is *ADC*. However, the discrepancies in reported values of *ADC* thresholds for discrimination of malignant and benign breast masses between multiple studies make it difficult for use in clinical routine (Keenan et al. 2016a). Therefore, to decrease the number of unnecessary breast biopsies, the quality assurance is an important aspect of quantitative DWI.

The aim of this study was to assess the temporal and spatial consistency of the measurements of quantitative parameter *ADC*. To achieve this, the breast phantom for quality control of diffusion-weighted images was developed. Spatial and temporal variability was assessed for different diffusion-weighted sequences with various setup parameters.

3.2 Part II – Breast DKI of Suspicious Mammography Findings

As mentioned at the beginning of this chapter, diffusional kurtosis is an additional diffusion-based parameter which may contain independent information regarding pathophysiology with respect to diffusion restrictions and tissue complexity (Jensen and Helpern 2010). A possible major confounding factor for DKI in the female breast is the presence of residual fat signal.

The female breast is composed of a mix of fibroglandular and adipose tissue. The tissue composition in women varies greatly and changes as the breast ages. According to the BI-RADS lexicon, breast density on mammography can be classified into one of the four categories: almost entirely fatty, scattered areas of fibroglandular density, heterogeneously dense, or extremely dense (Spak et al. 2017). Some women might present with extremely dense breast tissue, with the fibroglandular component accounting for the vast majority of the breast volume, while other women might present with almost entirely fatty tissue and only small amounts of fibroglandular tissue. Among examined women, one in ten have almost entirely fatty breast and four in ten women have breast with scattered areas of fibroglandular density (Sickles 2013). Moreover, the mammographic breast density decreases with age already in premenopausal women, with the most pronounced decrease during menopausal transition and continued in postmenopausal years (Burton et al. 2017). Moreover, fatty tissue is characterized by significantly lower *ADC* than the *ADC* of glandular tissue (Baron et al. 2010). That is, as the diffusion-weighting increases, there is a very weak attenuation of the fat signal. Therefore, one of the key success factors in breast DWI and DKI is complete suppression of the fat signal. If the signal from adipose tissue is not fully suppressed, then its residuals can contaminate the signal from the lesion and distort quantitative parameters (Partridge and McDonald 2013).

Initial findings of the prospective study devoted to the ability of DWI in discriminating between benign and malignant lesions in patients with suspicious findings on X-ray mammography published by Bickelhaupt et al. (2016), revealed higher than expected signal intensities in the regions of glandular tissue on the high *b*-value images in the examined cohort of patients. Taking into account that the signal from glandular tissue at high *b*-value is usually almost fully suppressed (Woodhams et al. 2011), the elevated signal might be attributed to the contamination with residual fat signal, caused by chemical shift artifacts or partial volume effects. A subsequent publication by Bickelhaupt et al. (2018), in which the main focus was to investigate radiomics models, also addressed this issue. In consequence, these reports

triggered the need for a detailed investigation of the potential contamination with residual fat-related background signal. Therefore, various phenomenological fitting approaches accounting for residual signal from adipose tissue were analyzed and their diagnostic performance for lesion characterization was evaluated.

3.3 Part III – DKI of Sonographically Indeterminate Ovarian Lesions

Ovarian cancer is the eighth most commonly occurring cancer and at the same time the eighth leading cause of cancer death in women (Bray et al. 2018). The primary imaging modality used for assessment of ovarian masses is ultrasonography (ACOG 2016). The characterization of ovarian lesions is of high importance because it determines the surgical treatment approach. The management of benign ovarian lesions relies usually on minimally invasive surgical procedure or conservative treatment (Choi et al. 2016), while in case of malignant lesions the surgery may have to be conducted in specialized oncological center (Vernooij et al. 2007). However, even when using the simple rules based on ultrasound predicting model for differentiation between benign and malignant masses, established by the International Ovarian Tumor Analysis (IOTA) group, approximately one-fifth of the cases still remains indeterminate (Auekitrungrueng et al. 2019; Timmerman et al. 2010). If the character of the lesion cannot be determined using ultrasonography, MRI is used in the second line. According to the recommendations published in (Forstner et al. 2017), the further assessment of sonographically indeterminate adnexal masses using diffusion-weighted MRI, based on analysis of signal intensity on diffusion-weighted images and the value of *ADC* is particularly beneficial in specific cases, e.g., in case of non-fatty and non-haemorrhagic entirely solid masses, septate cysts, complex solid and cystic masses.

In general, the diffusion restrictions are usually manifested by high signal intensity on high *b*-value images and corresponding low *ADC* values, what may indicate the presence of malignancy. However, authors of several studies and meta-analyses examining the role of DWI in characterization of suspicious adnexal masses have demonstrated relatively low *ADC* values in specific histological types of benign ovarian lesions, like teratoma, endometrioma or hemorrhagic cysts, and therefore quantitative analysis of *ADC* values may lead to false-positive findings (Agostinho et al. 2019; Duarte et al. 2018; Kim et al. 2016). Fortunately, in majority cases of these types of benign lesions the accurate clinical diagnosis can be efficiently made based on the conventional morphological sequences like T_1-weighted, T_2-weighted or fat suppressed T_1-weighted images (Agostinho et al. 2019; Spencer et al. 2010).

Although DWI may improve the performance of MRI of ovarian masses, the use of the *ADC* as a quantitative parameter for discrimination between benign and malignant ones is limited due to the considerable overlap in *ADC* values (van Nimwegen et al. 2020). However, the diagnostic value of parameters derived by diffusion kurtosis MRI using higher diffusion

weightings in characterization of ovarian lesions remains still largely unexplored. Therefore the aim of this study is to evaluate the diagnostic ability of parameters derived by DKI in characterization of sonographically indeterminate ovarian lesions as a standalone method.

4 Materials and Methods

This chapter gives an overview of the data collection process as well as provides detailed description of the methods and tools used for data analysis conducted in this work. Section 4.1 is devoted to the DWI breast phantom dedicated for assessment of the spatial and temporal homogeneity of the *ADC* measurements with a breast coil. It describes the construction of the phantom, the acquisition of DWI data and their evaluation based on the MATLAB script. Section 4.2 specifies the improvement of the DWI breast phantom construction and describes the imaging procedure used for further assessment of *ADC* homogeneity. Section 4.3 deals with the clinical breast DWI imaging and the problem of the possible corruption of the signal with not fully suppressed fat. Various mathematical representations accounting for this contamination were conceptualized. Section 4.4 deals with the diagnostic ability of DKI in characterization of suspicious ovarian lesions. It presents the method used for analysis of correlated data.

4.1 Breast Phantom I

This section presents the method used for the assessment of homogeneity of *ADC* measured with the use of the breast coil. To achieve this, a homogeneous DWI phantom dedicated for the breast coil was constructed. Moreover, to facilitate easy data evaluation, automated analysis tool was implemented in MATLAB. The sections below describe the subsequent steps for analysis of *ADC* homogeneity .

4.1.1 Phantom Design

The fabricated breast phantom consists of two identical parts of simplified breast-mimicking volumetric shape, attached to an acrylic glass plate as shown in Figure 3. Each part was made of the Veroclear RGD810 material (Stratasys) with the use of an Objet 30pro 3D-printer. Two plastic threaded rods were screwed perpendicularly to the lid of each phantom part. The lids were made of an acrylic glass. The two phantom components can be attached to the acrylic glass plate using plastic nuts, which enables the positioning in the left and right direction of the coronal plane. Inside one of the phantom parts, a thermometer was glued parallel to the surface of the cover. Each component was filled with approximately 1300 ml of 30% (w/w) aqueous polyvinylpyrrolidone (PVP) K-30 solution (Sigma-Aldrich).

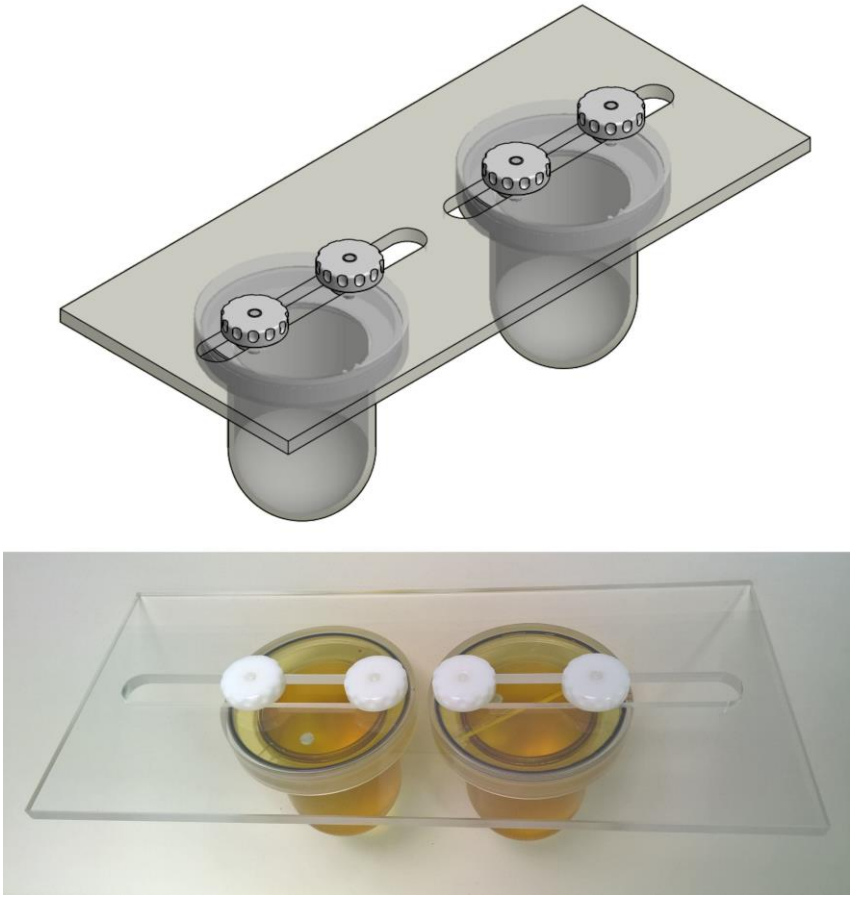

Figure 3. Isometric view of the phantom assembly design (top) and the manufactured phantom filled with aqueous 30% PVP K30 solution (bottom).

4.1.2 Imaging Protocol

The MRI images were acquired using 3T scanner (Prisma, Siemens, Erlangen, Germany) with an 18-channel breast coil. The phantom, which was stored in the scanner room, was placed in the prone position and scanned in the transversal plane. Before the start of the measurements, the temperature of the PVP-solution in the phantom was read off from the built-in thermometer. The DWI protocol consisted of 4 types of RESOLVE sequences and 6 types of single-shot EPI sequences. At the end, the acquisition of the first two types of the RESOLVE sequences was repeated. The main distinguishing features of the evaluated sequences are diffusion gradients' design (monopolar or bipolar gradients), and the acceleration factor of the parallel imaging technique GRAPPA (reduction factor R = 2,3,7 or non-parallel imaging acquisition). The common features of all the acquired sequences are: 4 *b*-values = 0,100,750,1500 s/mm^2 with number of signal averages = 1,1,1,3 respectively, field of view 240mm×480mm, acquisition matrix 72×192, slice thickness 3 mm, and number of slices = 37. Although the phantom was constructed without a fat content, the sequences were

acquired with the SPAIR technique, as in the original sequence used in the clinical routine. A saturation band was placed in the region of the phantom rim to suppress the signal from this area. Selected details of DWI sequences are summarized in Table 1. The measurements were repeated in the five subsequent days.

Table 1. Technical details of the acquired DWI sequences.

Sequence	**Gradient design**	**GRAPPA, factor**	**TR [ms]**	**TE [ms]**	**TA [min:s]**	**BW [HZ/px]**
$RESOLVE_1$	monopolar	2	16260	53	05:43	1300
$RESOLVE_2$	bipolar	2	16260	65	05:43	1300
$RESOLVE_3$	monopolar	off	16260	69	05:27	1185
$RESOLVE_4$	bipolar	off	16260	79	05:43	1185
$SS\text{-}EPI_1$	monopolar	2	16200	55	02:58	2365
$SS\text{-}EPI_2$	bipolar	2	16200	67	02:58	2365
$SS\text{-}EPI_3$	monopolar	3	16200	48	03:31	2365
$SS\text{-}EPI_4$	bipolar	3	16200	59	03:31	2365
$SS\text{-}EPI_5$	monopolar	7	16200	45	04:35	2365
$SS\text{-}EPI_6$	bipolar	7	16200	52	04:35	2365
$SS\text{-}EPI_7$	monopolar	off	16200	79	02:26	2365
$SS\text{-}EPI_8$	bipolar	off	16200	96	02:26	2365

4.1.3 *ADC* Calculations

The analysis of the diffusion-weighted images was conducted using an in-house MATLAB script. The aim was to create a tool for automatic analysis of the collected data. In order to estimate the *ADC* value for each voxel, linear regression based on Equation (2.4) and the observed signals for the *b*-values was used. First of all, a logarithmic transformation is applied to Equation (2.4). For the measured value of the diffusion-weighted signal S_1, S_2, S_3 for *b*-values 100,750,1500 s/mm^2 denoted as b_1, b_2, b_3, the system of normal equations for a case without constant takes the following form:

$$\begin{bmatrix} \ln\left(\frac{S_1}{S_0}\right) \\ \ln\left(\frac{S_2}{S_0}\right) \\ \ln\left(\frac{S_3}{S_0}\right) \end{bmatrix} = -\begin{bmatrix} b_1 \\ b_2 \\ b_3 \end{bmatrix} ADC, \tag{4.1}$$

where $S_0 = S(b_0 = 0)$ is a signal without diffusion-weighting. This can be simplified to:

$$\boldsymbol{S} = -\boldsymbol{b} ADC, \tag{4.2}$$

where $\boldsymbol{S} = \left[ln\left(\frac{S_1}{S_0}\right), ln\left(\frac{S_2}{S_0}\right), ln\left(\frac{S_3}{S_0}\right)\right]^T$, $\boldsymbol{b} = [b_1, b_2, b_3]^T$.

To estimate the value of *ADC* parameter, the following normal equations have to be solved:

$$\boldsymbol{b} \cdot \boldsymbol{b} \cdot ADC = -\boldsymbol{b} \cdot \boldsymbol{S}. \tag{4.3}$$

After transformation, the *ADC* parameter can be found by calculating the formula:

$$ADC_{\text{initial}} = \frac{-\boldsymbol{b} \cdot \boldsymbol{S}}{\boldsymbol{b} \cdot \boldsymbol{b}}. \tag{4.4}$$

In case of a negative value of the expression above, the final *ADC* value equal to zero is assigned to the affected pixels.

In the next step, the dependency of the *ADC* on the temperature is taken into consideration. Therefore, the previously calculated *ADC* value is calibrated to the reference temperature of the 20°C using the following transformation:

$$ADC = c_1 \cdot e^{c_2 \cdot (T - T_0)}, \tag{4.5}$$

where c_1 is the *ADC* at T_0 = 20°C, c_2 is a factor describing the temperature dependency, and *T* is an actual temperature of the phantom in degree Celsius. The value of c_2 was taken from the study published by Wagner et al. (2017) who experimentally determined this as c_2 = 0.02995 for 30% K30-PVP-solution at 3T. A simple calculation reveals that temperature increase by one Celsius degree causes *ADC* increase of 30% K30-PVP-solution by ~3% in comparison to the *ADC* value at 20°C.

By rearranging terms in Equation (4.5), the calibrated *ADC* is given as:

$$ADC_{20°\text{C}} = \frac{ADC_{\text{initial}}}{\exp^{(c_2 \cdot (T - T_{20°\text{C}}))}}. \tag{4.6}$$

The scale on the thermometer was with the graduation of 0.5°C, however the accuracy of the read-out based on the visual judgement was possible up to 0.125°.

4.1.4 ROI Segmentation

The shape of the scanned phantom was determined on the non-diffusion-weighted images, individually for each slice, using the Canny edge detection function provided by MATLAB. This approach extracts the edges of the objects in the picture in the multi-step process including smoothing of the image with the use of a Gaussian filter, computing the gradient magnitude and orientation to locate the edges and estimate their strengths, applying the non-maxima suppression to thin the edges, and finally performing the hysteresis thresholding to better extract the real edges (Canny 1986; Xin et al. 2012). To find the outline of an object, two thresholds are applied. The upper threshold results in less fake edges, but the outline might be discontinuous, therefore the lower threshold is intended to connect these strong edges, but gives as a result less accurate contours (Xin et al. 2012). In this work, the two thresholds, manually adjusted, are consistent among all the measurements. After the outline of the phantom is established, five regions of interest (ROIs) are automatically segmented inside each part of the phantom, which gives 10 ROIs in total per slice. An exemplary placement of the ROIs is shown in the Figure 4. The size of a ROI varies from slice to slice depending on the cross section width of the respective part of the phantom in an individual image. First of all, the lower border of the phantom is found on the middle slice image and is defined as a default value for all other slices. Then, each separate slice is divided into four regions within which the vertical edges of the phantom are defined. If not all four vertical edges can be found, then the slice is excluded from the analysis. In the next step, the upper border of the phantom is defined and the upper ROI in a shape of a segment of the circle is determined. Then, rectangular ROIs near the bottom, in the middle and near left and right vertical edge are placed. All ROIs are placed in a certain distance from the edges to reduce the influence of the artifacts. In case of overlapping ROIs or small cross-sectional area of the phantom, the slice is excluded from the analysis.

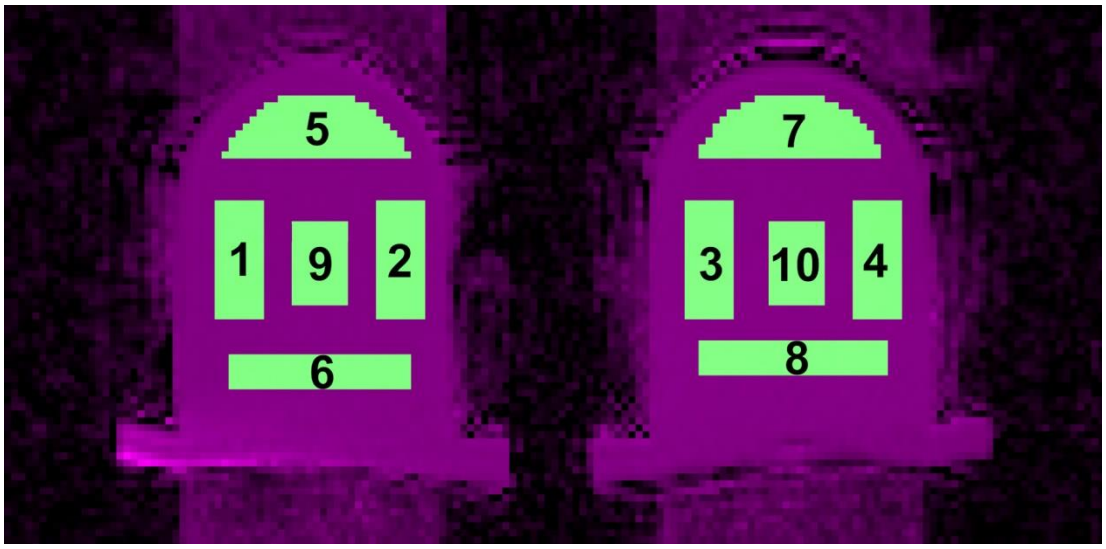

Figure 4. An example of the automatic ROIs placement in the non-diffusion weighted image. The ROIs on the left side of the picture are labeled as follows: 1 – left ROI, 2 – right ROI, 5 – upper ROI, 6 – lower ROI, 9 – middle ROI; on the right side: 3 – left ROI, 4 – right ROI, 7 – upper ROI, 8 – lower ROI, 10 – middle ROI.

4.1.5 Statistical Analysis

The variability of *ADC* was measured by the coefficient of variation (*CV*) which describes the relative dispersion of the data around the mean. *CV* is defined as (Dawson and Trapp 2004):

$$CV = \frac{\sigma}{\mu} \cdot 100\%, \tag{4.7}$$

where σ is the standard deviation and μ is the mean.

The spatial and temporal variability of *ADC* is determined in multiple steps. At first, the overall *ADC* variability in the whole phantom is assessed by calculating the mean value in all the pixels from all the 10 ROIs and all the slices. Secondly, the general consistency of *ADC* in the left and in the right part of the phantom is assessed. Analogically, the pixels from all 5 ROIs and all the slices are taken for calculations. Further, the spatial variability of the *ADC* in the 10 regions represented by 10 ROIs is assessed. To achieve this, the mean values are calculated taking a particular ROI's pixels from all the slices. In each step, the stability of the values in the multiple measurements is assessed.

4.2 Breast Phantom II

The homogeneity of *ADC* measurements in the longer period of time was assessed in the second round of measurements. The second experiment was conducted using an improved version of the phantom. The screw-on lid was replaced by a cover attached with six screws (see Figure 5) to make the filling with a liquid up to the cover easier and reduce the formation of air-bubbles. The other technical details remained unchanged (see Section 4.1.1).

Figure 5. Isometric view of a one part of the phantom with the improved cover.

The six measurements were carried out weekly for 6 weeks by a medical technologist. The DWI protocol contained four variants of an EPI work-in-progress (WIP) sequence. The technical details of the used DWI sequences are listed in Table 2. The common settings for all the sequences are as follows: 4 *b*-values = 0, 100, 750, 1500s/mm^2 with number of signal averages = 1, 3, 5, 10 respectively, field of view = 225mm × 360mm, acquisition matrix 94 × 150, slice thickness 3 mm, number of slices = 50. The WIP_3 and WIP_4 are motion-corrected versions of WIP_1 and WPI_2. However, for a static phantom like the proposed DWI breast phantom, it is expected that the sequences with motion correction will deliver similar results as the corresponding ones without motion correction. No saturation band is applied. The analysis of the data was conducted according to the procedure described in Sections 4.1.3– 4.1.5. The automatic ROI segmentation process was adjusted to the size of the acquisition matrix.

Table 2. Details of the EPI WIP sequences used in the second round of the measurements.

Sequence	**Gradient design**	**GRAPPA, factor**	**TR [ms]**	**TE [ms]**	**TA [min:s]**	**BW [HZ/px]**
WIP_1	monopolar	2	7320	55	02:41	2565
WIP_2	bipolar	2	7840	69	02:53	2564
WIP_3	monopolar	2	7320	55	02:41	2565
WIP_4	bipolar	2	7840	69	02:53	2564

4.3 Breast

This section explains the methodological approach for investigating the influence of the residual fat signal on the ability of DKI-derived parameters to differentiate between benign and malignant breast lesions. The presented work is a retrospective analysis of the data prospectively acquired in a two-institution MRI study. The prospective study received ethical approval (S-151/2014) from the Ethics Commission of the Medical Faculty of the University of Heidelberg. The inclusion criteria for the prospective study was a presence of a suspicious finding on X-ray screening mammography, classified as BI-RADS 4 or BI-RADS 5, followed by indication for breast biopsy. All the patients with ambiguous lesion, after the primary mammography, underwent the clarification process incorporating ultrasound, clinical examination or magnification mammography. The MRI examination took place before the biopsy. The results of a core needle biopsy performed in the guidance of the ultrasound or X-ray images served as a reference standard.

In this retrospective research, the patients were excluded if their lesions were unrecognizable on the DWI images (23 patients) or due to the technical problems in the DWI acquisition (1 patient). In total, 198 patients with a single breast lesion were enrolled.

4.3.1 Imaging Protocol

The patients were scanned in one of the two study centers, equipped with 1.5T scanners. In the first study center Group A was scanned with the Ingenia MR scanner (Philips, Best, the Nederlands) using 2-channel breast loop coil and the elements of the spine coil in the table. In the second study center Group B was examined with the Aera MR scanner (Siemens, Erlangen, Germany) using 18-channel breast coil. For all patients, the diffusion-weighted sequence was acquired in addition to the full diagnostic protocol consisting of T_2-weighted and T_1-weighted precontrast sequences and T_1-weighted contrast enhanced sequence. The diffusion-weighted images were acquired using 4 *b*-values 0, 100, 750 and 1500 s/mm^2. The details of the MRI protocols are listed in the Table 3.

Table 3. Details of the used DWI sequences for breast lesion imaging.

Feature	**Group A**	**Group B**
scanner	1.5T Ingenia, Philips	1.5T Aera, Siemens
b-value	0, 100, 750, 1500 s/mm^2	0, 100, 750, 1500 s/mm^2
phase encoding direction	RL	AP
fat suppression technique	SPAIR	SPAIR
parallel imaging	SENSE × 2.5	GRAPPA × 2
acquisition bandwidth	2393 Hz/px	870 Hz/px
readout	single shot EPI	readout segmented EPI with 3 segments
Field Of View (FOV)	340 mm × 400 mm	480 mm × 240 mm
voxel size	2.5 mm × 2.5 mm	2.5 mm × 2.5 mm
slice thickness	3 mm	3 mm
TR	10.6 s	11.7 s
TE	100 ms	80 ms

4.3.2 Volume of Interest

For each patient three ROIs were delineated manually by a postgraduate medical researcher in consensus with a board-certified radiologist using The Medical Imaging Interaction Toolkit (MITK, DKFZ, Heidelberg, Germany). At first, the three-dimensional segmentation of a lesion was performed on the highest *b*-value image. In some cases the lesion could not be identified on the b = 1500 s/mm^2 image and therefore was delineated on the b = 750 s/mm^2 image. The ROI delineation on diffusion-weighted images was performed using the information about location described in the X-ray screening report and complementary T_2-weighted images. In addition, for each patient a second two-dimensional ROI in the fatty tissue area was manually delineated. The adipose tissue was identified on T_2-weighted images, in the region free of the artifacts. The one-slice fat ROI was usually segmented on the contralateral breast like a mirror image of the lesion, keeping a similar distance from the coils, to mimic the sensitivity of the coils near the lesion. The third ROI was segmented for the estimation of background signal level. The quadratic ROI of size 10×10 pixels, was automatically placed in the corner of the DWI-image, 10 pixels from the edges, outside the patient's body, on all slices.

4.3.3 DWI-Fitting Models to Evaluate the Influence of Residual Fat Signal

To investigate the influence of the residual fat signal, the five fitting methods were evaluated and compared. For the sake of clarity, $D_1 - D_5$ denote the apparent diffusion coefficient and $K_2 - K_5$ denote the apparent kurtosis coefficient.

Method1: Firstly, the mono-exponential equation was used:

$$S(b) = S_0\, e^{-bD_1}, \tag{4.8}$$

where $S(b)$ is the diffusion-weighted signal, S_0 is the signal without diffusion-weighting, b is diffusion sensitizing factor.

Method2: Secondly, the diffusion kurtosis equation was fitted:

$$S(b) = S_0\, e^{-bD_2+\frac{1}{6}b^2D_2^2K_2.} \tag{4.9}$$

Method3: This method assumes that the signal from the adipose tissue is transferred to the lesion area in a result of the chemical shift in the phase encoding direction. Due to the low value of *ADC* of fat, fat signal can be considered constant for each *b*-value. Therefore, the measured signal, in the lesion area, can be approximated by equation:

$$S(b) = S_0\, e^{-bD_3+\frac{1}{6}b^2D_3^2K_3} + a \cdot \theta(b_{max}), \tag{4.10}$$

where $\theta(b_{max})$ is the signal measured in the fatty tissue ROI at the maximal *b*-value = 1500s/mm^2 and $a = 0.1, 0.2, 0.3 \ldots 1$ is a factor moderating step-wise the contribution of the $\theta(b_{max})$ to the overall measured signal. The assumptions of this method are illustrated in the Figure 6.

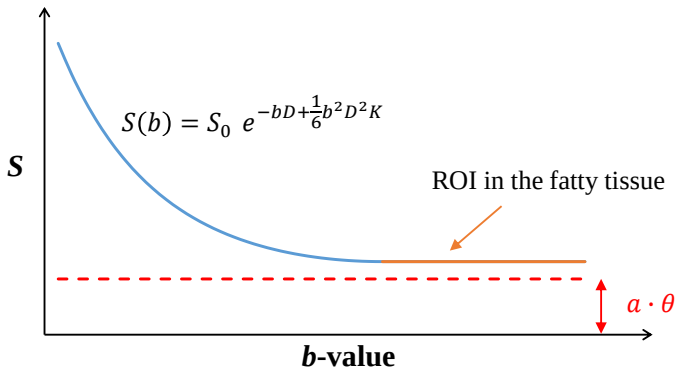

Figure 6. A conceptual plot of the signal decay in the lesion contaminated with the signal from adipose tissue due to the chemical shift artifact. It can be postulated that the almost constant signal measured at the higher *b*-values might come from the fat due to its low *ADC* value, and therefore build a peculiar background level θ. Factor a describes the fraction of θ contributing to the measured signal in the lesion area.

Method4: In this approach, the phenomenological modification of the equation proposed by Jensen et al. (2005) was used. The η factor denoting the noise background level in Equation (2.14) was replaced by $\theta(b_{max})$ denoting the background signal from the chemical shift artefact:

$$S(b) = \sqrt{\left(S_0\, e^{-bD_3+\frac{1}{6}b^2D_3^2K_3}\right)^2 + \theta(b_{max})^2}, \tag{4.11}$$

where $\theta(b_{max})$ is the signal in the fatty tissue area at b-value = 1500s/mm^2. The similar phenomenological extension with the term accounting for fat-related signal was primarily applied to radiomics model by Bickelhaupt et al. (2018). However, the direct influence of the correction term on the values of diffusion-kurtosis-derived coefficients has not been studied yet.

Method5: This method considers a possible contamination of the pixels located nearby the ROI boarder with a signal from the abutted adipose tissue as a result of the partial volume effect (see Figure 7). In this case the contaminating signal comes from fat and water protons, its dependency on b-value is expected. The overall signal in the lesion can be represented as a sum of the fractions of the standard kurtosis equation and the signal from the fatty tissue of discarded absolute magnitude:

$$S(b) = S_0\left[f e^{-bD_5+\frac{1}{6}b^2D_5^2K_5} + (1-f)\tilde{\theta}(b)\right], \tag{4.12}$$

where $\tilde{\theta}(b) = \frac{\theta(b)}{\theta(b=0)}$ and $f = 0.1, 0.2, 0.3 \ldots 1$ is a factor moderating the fractions of the signals.

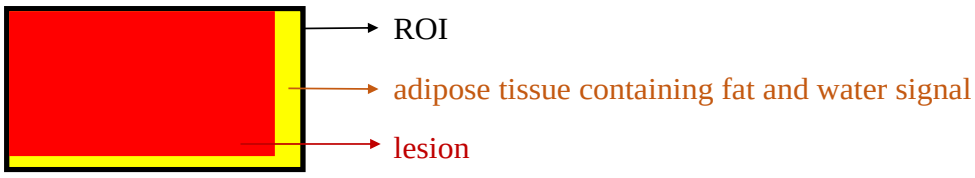

Figure 7. Illustration of the contamination of the ROI with the adipose tissue lying nearby the border. The abutted pixels contain the signal from fat and water protons.

The analysis of the DWI data was conducted using an in-house script written in MATLAB. The optimization algorithm "Trust Region" with constrained non-linear least square fitting was employed for the purpose of fitting. The curves were fitted to the mean of the measured signal for three b-values: 100, 750 and 1500 s/mm^2. As a fitting option, the lower and upper boundary conditions were set to fulfill the requirements: $0 \leq D_i \leq 3.5\ \mu m^2/ms$ and $0 \leq$

$K_i \leq 3$, according to the recommendation published in (Bickelhaupt et al. 2018). S_0 was set as a free parameter and the measured signal for b = 0 was set as a starting point for the optimization process. For adjusted methods 3-5, the mean value of the signal in the fatty tissue area was taken during the fitting process, with constant or changing value with the strength of diffusion weighting, according to the used approach.

Moreover, the results delivered by the Method4 with the $\theta(b_{max})$ factor accounting for residual fat related signal were compared with the original approach proposed by Jensen, Equation (2.14), accounting for background signal level, which is denoted in this thesis as Method4b. To do this, the mean value of the signal in the three-dimensional ROI at *b*-value = 1500s/mm^2 was taken.

4.3.4 Lesion-to-Background Ratio

It may be expected that the proposed methods accounting for residual fat related signal should perform better than the standard methods in case of the lesions highly corrupted with signal from fat. It can be assumed that such lesions are characterized by the low contrast between the lesion and the adipose tissue on the high *b*-value image. To investigate this assumption, a lesion-to-background ratio (*LBR*) was introduced. *LBR* was defined as a ratio of the mean signal intensity on the highest measured *b*-value image in the lesion ROI and the fat ROI, given by the following equation:

$$LBR = \frac{\mu_t}{\mu_b} \tag{4.13}$$

where μ_t is the mean value of the signal measured on the *b*-value = 1500 s/mm^2 image in the lesion and μ_b the mean value of the signal measured on the *b*-value = 1500 s/mm^2 image in the segmented fatty tissue area. Two thresholds were applied, to divide each of the two groups of patients (Group A and Group B) into the three subgroups representing low ($LBR < 1.5$), middle ($1.5 \leq LBR < 2$) and high lesion-to-background ratio ($LBR \geq 2$).

4.3.5 Statistical Analysis

Multiple logistic regression was used as a classifier of malignancy and benignancy of the lesions. The diagnostic performance of the proposed logistic regression models was assessed by plotting Receiver Operating Characteristic (ROC) curve for each model. The accuracy of the predictions was assessed by value of Area Under the ROC Curve (AUC), as well as specificity and sensitivity level.

A logistic regression model describes the probability of the malignancy of the lesion according to the equation (David G. Kleinbaum 2002):

$$P\left(D = 1 \middle| X_1, X_2, \dots X_k\right) = \frac{1}{1 + e^{-(\alpha + \sum_{i=1}^{k} \beta_i X_i)}}, \tag{4.14}$$

where D indicates malignancy, X_1, X_2, up to X_k are independent variables, α and β_i are logistic regression parameters. In this analysis, apparent diffusion coefficient and apparent diffusional kurtosis coefficient were taken as a predictor in logistic regression models.

To assess the diagnostic performance of the diffusion and diffusion kurtosis parameters, the Receiver Operating Characteristic (ROC) curves were analyzed. ROC curve describes the relationship between false-positive rate and true-positive rate what relates to 1-specificity and sensitivity of the diagnostic test.

Sensitivity is defined as the true positive fraction. It means it describes the accuracy of diagnosing malignancy among the patients with malignant lesions:

$$Sensitivity = \frac{number\ of\ true\ positive\ desicions}{number\ of\ actually\ positive\ cases}. \tag{4.15}$$

Specificity describes the accuracy of diagnosing benignity among patients with benign lesions:

$$Specificity = \frac{number\ of\ true\ negative\ desicions}{number\ of\ actually\ nagtive\ cases}. \tag{4.16}$$

In analogy, 1-specificity is defined as false positive fraction and describes the rate of benign lesions wrongly diagnosed as malignant:

$$1 - Specificity = \frac{number\ of\ false\ positive\ desicions}{number\ of\ actually\ nagtive\ cases}. \tag{4.17}$$

The perfect test has high specificity and high sensitivity that is low false-negative rate and low false-positive rate. *p*-values smaller than 0.05 were chosen as an indicator for statistically significant difference.

4.4 Ovaries

The focus of this chapter is on research methodology of effectiveness of DKI as a standalone modality for differentiation of sonographically indeterminate ovarian lesions.

The research described in this dissertation was conducted using data gathered in a prospective single-institutional study. The study received ethical approval (S-337/2016) from the Ethics Commission of the Medical Faculty of the University of Heidelberg. The recruitment criteria for patient enrollment was the presence of sonographically indeterminate adnexal masses. From the collective of 84 patients, who were examined between November 2016 and December 2018 using MRI, 19 were excluded due to the non-visible adnexal lesion on MRI, 2 patients received conservative treatment, 3 patients were lost to follow-up, 1 patient was

scanned with different DWI sequence parameters. Finally, data from 21 patients with the bilateral ovarian lesion and data from 37 patients with a single lesion in the left or right ovary were used in the main analysis. In total, 79 lesions were included. The reference standard used in this study was established by the histopathological findings obtained from surgical procedure performed on each patient. MRI examination was performed before surgery.

Moreover, taking into account that certain types of benign lesions can lead to false-positive findings during DWI examination due to their relatively low *ADC* value, the additional subanalysis of a reduced cohort of patients was also performed. The aim was to investigate the influence of these lesions on the overall performance of DKI in distinguishing between benign and malignant masses. According to the guidelines of the radiologist involved in this study, 30 lesions with following histopathological result were excluded: endometrioma, dermoid (mature cystic teratoma), corpus luteal cyst (hemorrhagic), mucinous cystadenofibroma with associated mature teratoma. The reduced cohort of patients included 49 lesions.

4.4.1 Imaging Protocol

The MRI data were acquired using 3T scanner (Prisma, Siemens, Erlangen) equipped with 16-channel body coil. In almost all cases, full diagnostic protocol comprising T_1-weighted and T_2-weighted sequence, diffusion-weighted sequence and enhanced T_1-weighted sequence was applied. Two patients declined the application of contrast agent. The DWI sequence used six *b*-values: 0, 50, 100, 800, 1500 and 2000 s/mm^2. The parameters are listed in Table 4. In general, 60 slices were acquired. However, for some patients, the FOV had to be extended due to the large size of the lesion.

Table 4. Technical details of DWI sequence used for imaging of ovarian lesions.

Feature	**Values**
scanner	3.0T Prisma, Siemens
b-value	0, 50, 100, 800, 1500, 2000 s/mm^2
fat suppression technique	SPAIR
parallel imaging	GRAPPA × 2
readout	single shot EPI
FOV	296 mm × 449 mm
voxel size	1.2 mm × 1.2 mm
slice thickness	3 mm
TR	6.2 s
TE	59 ms

4.4.2 Volume of Interest

The manual delineation of the ROIs was conducted in MITK by two board-certified radiologists, blinded to the histopathology results. Due to the general large size of the lesions, only a single slice, with the highest signal intensity in the lesion area on the image with b = 1500 s/mm^2, was selected, which represents the highest diffusion restriction in the tissue. The lesion localization on DWI images was done in conjunction with T_2-weighted images. In all cases the ROI was delineated directly on the image with b = 1500 s/mm^2. However, if the signal on b = 1500 s/mm^2 image was not strong enough to clearly identify the lesion, the contours were visually mapped to the edges on the lower b-value 800 s/mm^2 image.

4.4.3 Diffusion and Diffusion Kurtosis Fitting

At first, in the analysis, the standard diffusion mono-exponential equation was applied:

$$S(b) = S_0\, e^{-bADC}, \tag{4.18}$$

where *ADC* is the apparent diffusion coefficient, b diffusion sensitizing factor and S_0 is the non-diffusion-weighted signal. The curve was fitted to the three b-values: 100, 800 and 1500 s/mm^2 for each voxel separately. During the fitting process S_0 was set as a free parameter with a starting value of the measured signal at b = 0. Very low b-values were excluded from the fitting process to minimize the effect of IVIM. The highest b-value was omitted to reduce the effect of non-Gaussian diffusion.

In the second step, the parameters of diffusion kurtosis fitting model were derived from equation:

$$S(b) = S_0\, e^{-bD_{\mathrm{app}}+\frac{1}{6}b^2D_{\mathrm{app}}^2K_{\mathrm{app}}}, \tag{4.19}$$

where D_{app} is the apparent diffusion coefficient and K_{app} is the apparent kurtosis coefficient. For kurtosis-fitting four b-values were incorporated: 100, 800, 1500 and 2000 s/mm^2. The low b-values were also not included in the fitting. Likewise, S_0 was set as a free parameter.

The obtained parameter maps were further processed by excluding the pixels which did not satisfy the conditions: $0 < ADC < 3.5$ mm^2/s, $0 < D_{\mathrm{app}} < 3.5$ mm^2/s and $0 < K_{\mathrm{app}} < 3.0$, in accordance with the suggestions published in (Bickelhaupt et al. 2018).

4.4.4 Voxel Selection

An ovarian mass can consist of both solid and fluid-filled components, however the first one is more concerning and therefore significant for calculation of DWI and DKI parameters. Although manual segmentation of solid parts allows precise extraction of relevant regions, it

can be time-consuming and therefore not feasible in the clinical routine. Owing to this fact, a simplified automatic voxel selection procedure was developed. Under assumption that strong signal on high diffusion-weighted images represents the diffusion restrictions in the solid part of the lesion, the threshold for the signal intensity was applied to select the brightest pixels. The primary threshold was set up to select 1% the pixels inside the ROI with the highest signal intensity on the image b = 1500 s/mm^2. The selection of only 1% of the voxels was dictated by the fact that some lesions consisted mainly of large fluid-filled components and relatively small solid areas. On the other hand, in case of the small lesions, the additional restriction for the minimal total number of selected pixels was applied. That is, finally more than 10 pixels from the parameters map were taken into the further statistical analysis.

For the sake of comparison, a supplemental analysis was conducted using 10% of the voxels with the highest signal intensity in the ROI in the b = 1500 s/mm^2 image.

4.4.5 Statistical Analysis

To account for the possible correlation in outcomes between bilateral ovarian lesions of the some patient, the generalized linear mixed models (GLMMs) were applied. The difference in diffusion and diffusion kurtosis-derived parameters for benign and malignant lesions were tested using linear mixed model. Subsequently, the mixed logistic models with *ADC*, D_{app} and K_{app} as single predictor were built. Additionally, the multiple logistic mixed models were constructed to analyze the benefit of combining two predictors. In the built GLMMs the fixed effect is associated with diffusion and diffusion-kurtosis-derived parameters, whereas the random effect is associated with the variation in these parameters between left and right lesion in the patient. However, that the aim of the study was to analyze the relation of diffusion and diffusion-kurtosis-derived parameters between malignant and benign lesions for the whole population of patients. Hence, the differences in the bilateral lesions of the individuals are treated rather as disruptive effect and are out of the area of interest of this work. The linear and logistic mixed models were constructed using the built-in GLIMMIX procedure in SAS. The ability to discriminate malignancy from benignity was assessed by analyzing ROC curves using SigmaPlot 14.0 (Systat Software Inc., San Jose, California). For all tests, *p*-values $\leq$0.05 were considered as statistically significant.

5 Results

The results chapter is divided into four parts. The first two Sections 5.1 and 5.2 present the results of the use of the developed phantoms for quality assurance in breast DWI (according to the methods described in Sections 4.1 and 4.2). Section 5.3 shows the results of the use of various fitting models for characterization of breast lesions (see Section 4.3). In the last section of this chapter, the results of DKI in ovarian lesions are presented (see Section 4.4).

5.1 Breast Phantom I

In this section the results of the assessment of the homogeneity of *ADC* measurements with the use of the DWI breast phantom are presented. At first, the overall *ADC* value in the whole phantom is assessed. Then, the variability between the left and right part of the coil is evaluated. Finally, the spatial variability, represented by the values in the individual ROIs placed in the different regions of the phantom, is scrutinized.

5.1.1 Variability of the Mean *ADC* Measured in the Whole Phantom

At first, the mean *ADC* measured in the whole phantom, calculated from voxels in 10 ROIs from all slices was assessed. The sequence with parallel imaging and bipolar gradients showed higher relative variation (3.93%–4.59%) than the sequence with monopolar gradients (1.37%–1.53%). Similarly, for analogous sequences without parallel imaging – the *CV* was in the rage of 3.34%–4.15% and 1.47%–1.65%, respectively.

Similarly, for EPI sequences, higher relative variation was observed for bipolar gradients than for monopolar gradients. At the same time, the relative variation in *ADC* was increasing with the higher acceleration factor of parallel imaging.

Nevertheless, the relative variation of the *ADC* in the subsequent measurements was comparable with the measurements for the same type of the sequence.

Table 5. The *CV* for the whole phantom over 5-day measurement and the mean *ADC* calculated in the single measurement for 5-day period.

Sequence	***CV* [%] in the whole phantom over 5 days**	**mean *ADC* [µm²/ms] (min – max) in the single measurement for 5-day measurements period**	
		Left part of the phantom	**Right part of the phantom**
$RESOLVE_1$	1.48	0.848–0.856	0.861–0.869
$RESOLVE_2$	4.21	0.882–0.894	0.833–0.836
$RESOLVE_1$ 2^{nd}	1.59	0.847–0.850	0.866–0.868
$RESOLVE_2$ 2^{nd}	4.20	0.874–0.884	0.831–0.833
$RESOLVE_3$	1.61	0.853–0.853	0.864–0.865
$RESOLVE_4$	3.80	0.888–0.891	0.842–0.834
$SS\text{-}EPI_1$	2.44	0.840–0.848	0.872–0.880
$SS\text{-}EPI_2$	5.09	0.847–0.856	0.923–0.932
$SS\text{-}EPI_3$	1.90	0.842–0.852	0.860–0.873
$SS\text{-}EPI_4$	4.50	0.856–0.867	0.915–0.921
$SS\text{-}EPI_5$	6.26	0.837–0.846	0.849–0.859
$SS\text{-}EPI_6$	8.69	0.838–0.845	0.906–0.913
$SS\text{-}EPI_7$	2.18	0.841–0.849	0.873–0.878
$SS\text{-}EPI_8$	2.33	0.850–0.851	0.884–0.887

5.1.2 Variability between the Left and the Right Part of the Phantom

In this section, the mean value was calculated from the pixels in 5 ROIs in all slices. For the RESOLVE sequence with monopolar gradients higher relative variation was observed in the right part of the phantom. In contrast, for the sequences with bipolar gradients, in majority of cases, an opposite trend was observed, that means higher relative variation in *ADC* was detected in the left part of the phantom. Moreover, in all the cases with monopolar gradient, the mean *ADC* of the right part was slightly higher than in the left part of the phantom. Conversely, for sequences with bipolar gradient, the *ADC* value measured in the right part of the phantom was smaller than *ADC* in the left part.

In all the analyzed types of the SS-EPI sequences, the relative variation in the right part of the phantom was always higher than in the left part. Additionally, in all the cases the mean *ADC* measured in the right part of the phantom was higher than in the left part, usually with

higher differences between the two parts of the phantom for sequences with bipolar gradients. When comparing sequences with the same value of the parallel imaging factor pairwisely, a higher *CV* was always observed for those with bipolar gradient compared to those with monopolar gradient.

5.1.3 Spatial Variability within the Left and the Right Part of the Phantom

In this part, the variability among 10 segmented ROIs, representing different internal regions in the phantom, is presented. For each measurement-day, the mean *ADC* was calculated for 10 ROIs separately, taking the pixels from the three slices in the middle into account, which resulted in 50 values of mean *ADC* and 50 values of *CV*.

For the RESOLVE sequence with parallel imaging and monopolar gradients, the relative variation in the individual ROIs was in the range of 0.38%–1.18% and was lower than for the bipolar gradients that was 0.68%–2.21%. The difference between the highest and the lowest calculated *ADC* was 0.031 $\mu m^2/ms$ for monopolar gradients and was four times smaller than for the bipolar gradients, which was equal to 0.125 $\mu m^2/ms$. By averaging the *ADC* values for each ROI over 5-day measurements, for monopolar gradients, the minimal mean *ADC* of 0.844 $\mu m^2/ms$ was observed for the left ROI in the left part of the phantom. A maximal *ADC* value of 0.863 $\mu m^2/ms$ was observed for left ROI in the right part of the phantom (Figure 8). For bipolar gradient, minimal mean *ADC* = 0.809 $\mu m^2/ms$ was calculated for the upper ROI in the right part of the phantom, whereas maximal *ADC* = 0.924 $\mu m^2/ms$ in the lower ROI in the left part. The dispersion of the differences in the single measurement between the 10 ROIs was much smaller for the monopolar gradients (0.019–0.025 $\mu m^2/ms$) than for the bipolar gradients (0.109–0.121 $\mu m^2/ms$). The *ADC* values measured over the 5 days are presented in Figure 9.

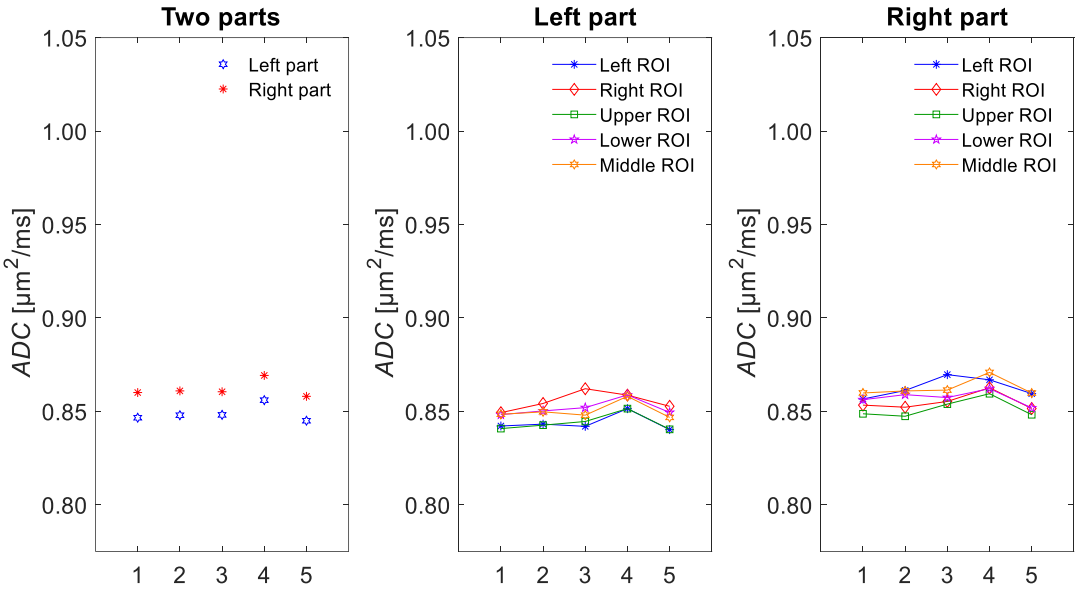

Figure 8. **RESOLVE$_1$** sequence with **monopolar** diffusion gradients and **parallel imaging** with a reduction factor of **2**. Plots shown from the left as follows: overall *ADC* in the left and right part of the phantom, *ADC* in the individual 5 ROIs segmented in the left part of the phantom, and *ADC* in the 5 ROIs in the right part of the phantom. The x-axis indicates measurement days.

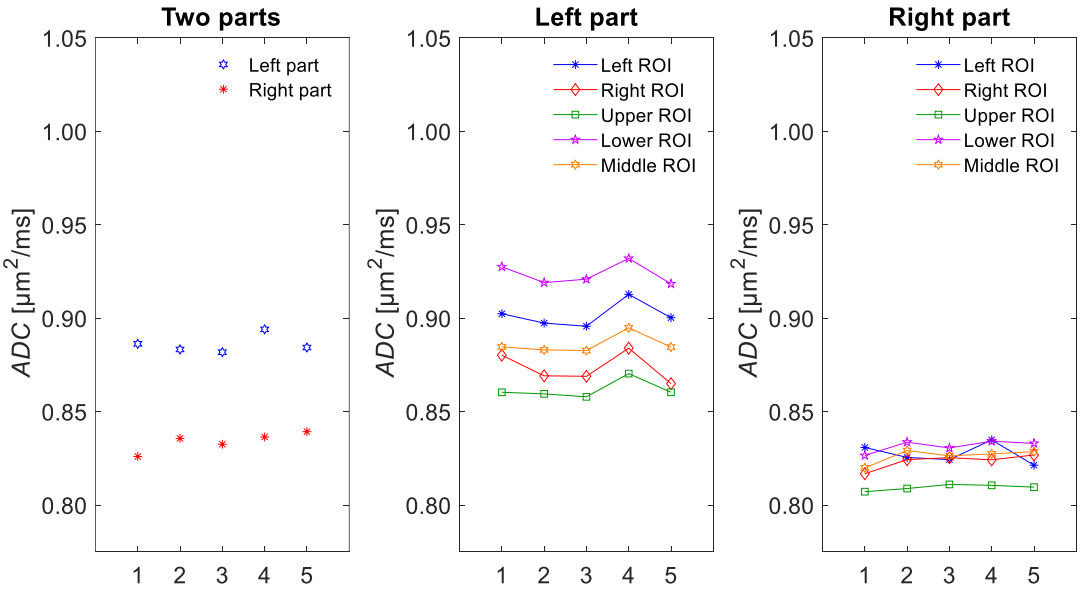

Figure 9. **RESOLVE$_2$** sequence with **bipolar** diffusion gradients and **parallel imaging** with a reduction factor of **2**. Plots shown from the left as follows: overall *ADC* in the left and right part of the phantom, *ADC* in the individual 5 ROIs segmented in the left part of the phantom, and *ADC* in the 5 ROIs in the right part of the phantom. The x-axis indicates measurement days.

The second measurement of the sequences RESOLVE$_1$ and RESOLVE$_2$, repeated on the same day, showed similar values of *CV* (0.38%–1.18% vs. 0.68%–2.21% respectively). In both cases, a similar spread of the *ADC* values was observed, with maximal difference of 0.032 μm^2/ms for the monopolar gradient and a difference of 0.123 μm^2/ms for the bipolar gradient. The mean *ADC* in the ROIs averaged over 5 measurements was in the range of 0.848–0.869 μm^2/ms for the monopolar (Figure 10) and 0.815–0.928 μm^2/ms for bipolar diffusion gradient (Figure 11).

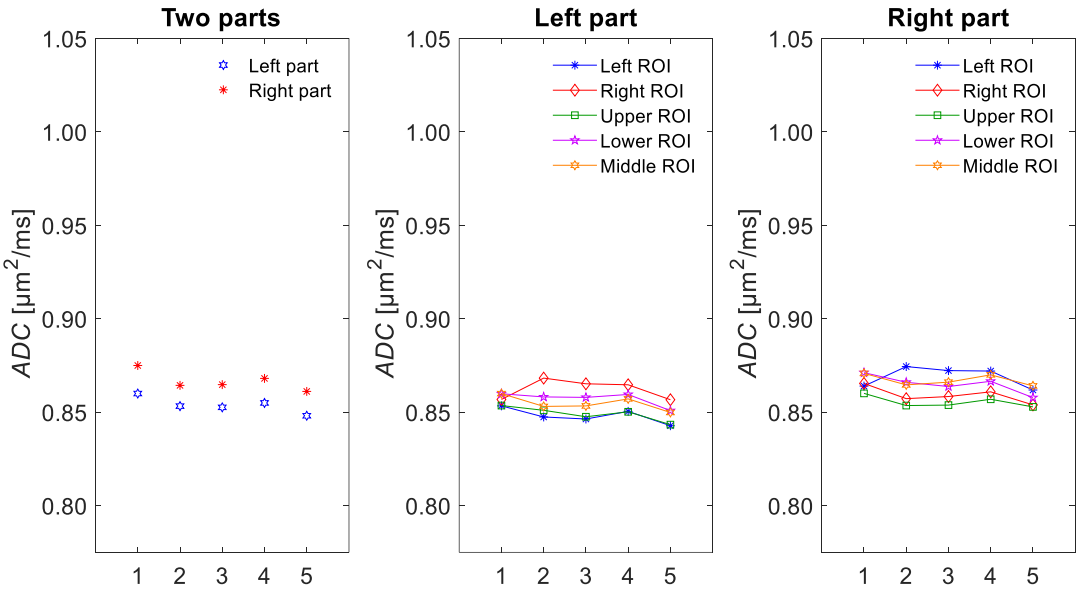

Figure 10. **Repeated** measurement at the same day of **RESOLVE$_1$** sequence with **monopolar** diffusion gradients and **parallel imaging** with a reduction factor of **2**. Plots shown from the left as follows: overall *ADC* in the left and right part of the phantom, *ADC* in the individual 5 ROIs segmented in the left part of the phantom, and *ADC* in the 5 ROIs in the right part of the phantom. The x-axis indicates measurement days.

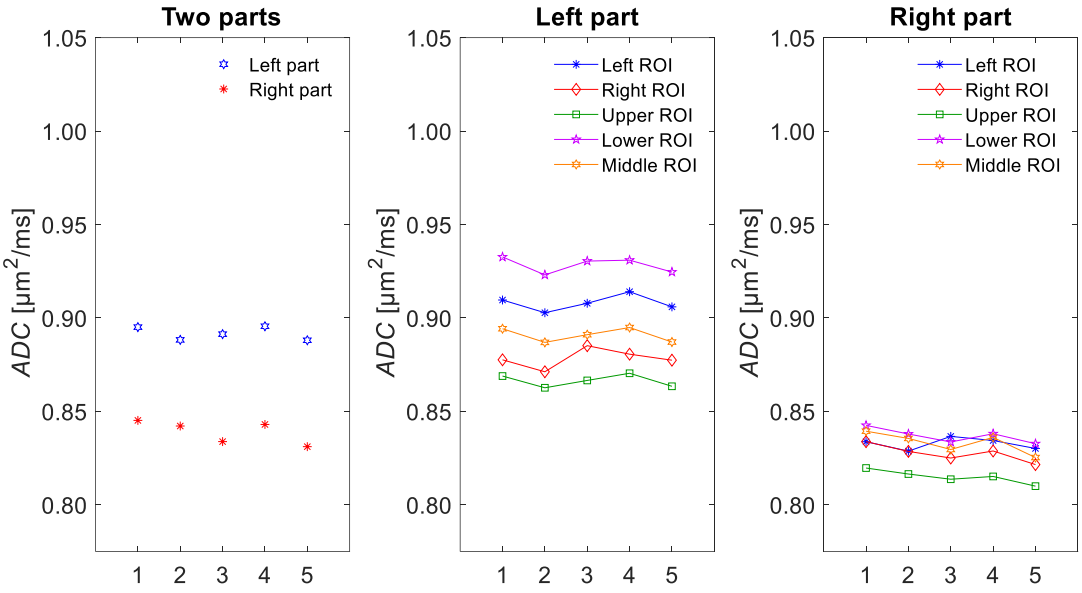

Figure 11. **Repeated** measurement at the same day of **RESOLVE$_2$** sequence with **bipolar** diffusion gradients and **parallel imaging** with a reduction factor of **2**. Plots shown from the left as follows: overall *ADC* in the left and right part of the phantom, *ADC* in the individual 5 ROIs segmented in the left part of the phantom, and *ADC* in the 5 ROIs in the right part of the phantom. The x-axis indicates measurement days.

For the RESOLVE sequence without parallel imaging, for monopolar gradients the relative variation in individual ROIs calculated for the 5 time-points separately, varies between 0.27% and 1.37% and was lower than for bipolar gradients which ranges from 0.40% to 2.23%. The maximal mean *ADC* averaged over 5-day measurements for the monopolar gradients was equal to 0.866 μm^2/ms for the lower ROI in the right part of the phantom, whereas the minimal was 0.840 μm^2/ms for the left ROI in the left part (Figure 12). For bipolar gradients, the highest mean value of 0.903 μm^2/ms was calculated for lower ROI in the left part of the phantom. The lowest value of 0.813 μm^2/ms was found for the upper ROI in the right part (Figure 13). The difference between highest and lowest calculated *ADC* was 0.042 μm^2/ms for RESOLVE$_3$ and was three times smaller than for RESOLVE$_4$, which was equal to 0.118 μm^2/ms. The differences between 10 ROIs in the single measurements were in the range of 0.022–0.032 μm^2/ms and 0.072–0.115 μm^2/ms, respectively.

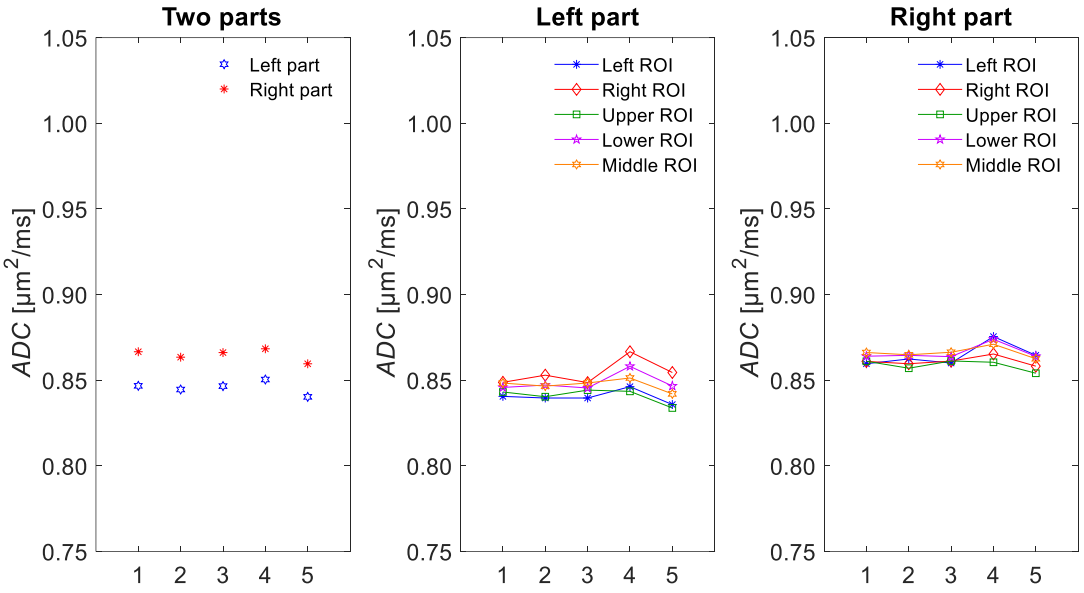

Figure 12. **RESOLVE$_3$** sequence with **monopolar** diffusion gradients, **without parallel imaging**. Plots shown from the left as follows: overall *ADC* in the left and right part of the phantom, *ADC* in the individual 5 ROIs segmented in the left part of the phantom, and *ADC* in the 5 ROIs in the right part of the phantom. The x-axis indicates measurement days.

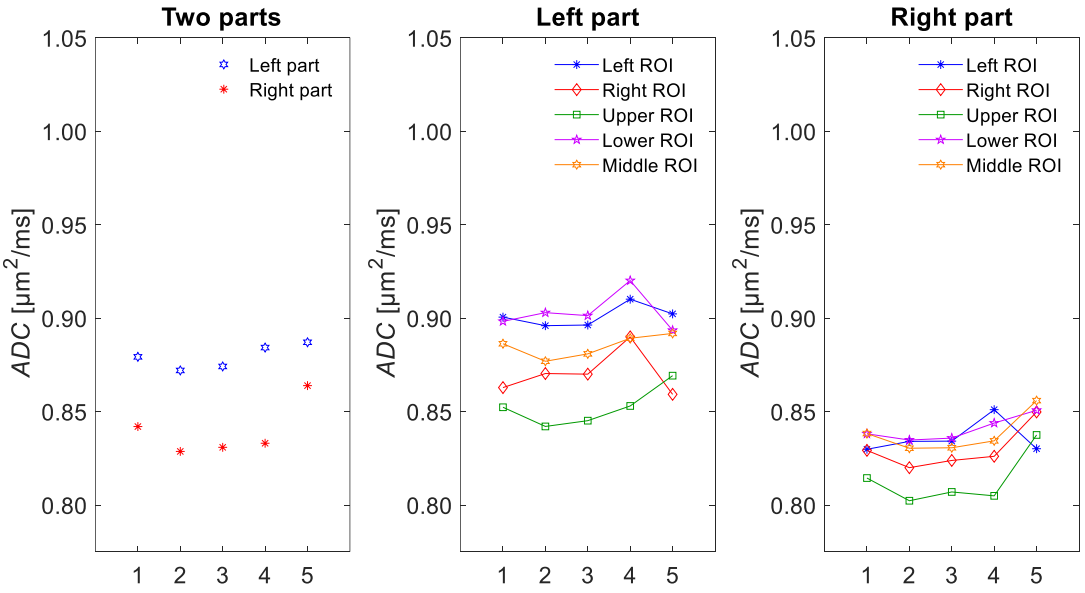

Figure 13. **RESOLVE$_4$** sequence with **bipolar** diffusion gradients, **without parallel imaging**. Plots shown from the left as follows: overall *ADC* in the left and right part of the phantom, *ADC* in the individual 5 ROIs segmented in the left part of the phantom, and *ADC* in the 5 ROIs in the right part of the phantom. The x-axis indicates measurement days.

Among single-shot EPI sequences, the highest *CV* was observed for the highest parallel imaging acceleration (GRAPPA = 7). The *CV* obtained for the sequence with monopolar gradients was in the range of 2.93%–9.47% and for bipolar gradients it was in the range of 4.11%–10.97%. The differences between the highest and the lowest *ADC* values calculated in one of the 10 ROIs among 5 measurements were 0.091 and 0.150 μm^2/ms, respectively. The differences among the ROIs in the single measurements were in the range of 0.075–0.088 μm^2/ms for monopolar and 0.132–0.145 μm^2/ms for bipolar gradients. The mean *ADC* calculated individually for each ROIs over 5 days took the value between 0.801–0.885 μm^2/ms for monopolar (Figure 14) and 0.824–0.957 μm^2/ms for bipolar gradients (Figure 15).

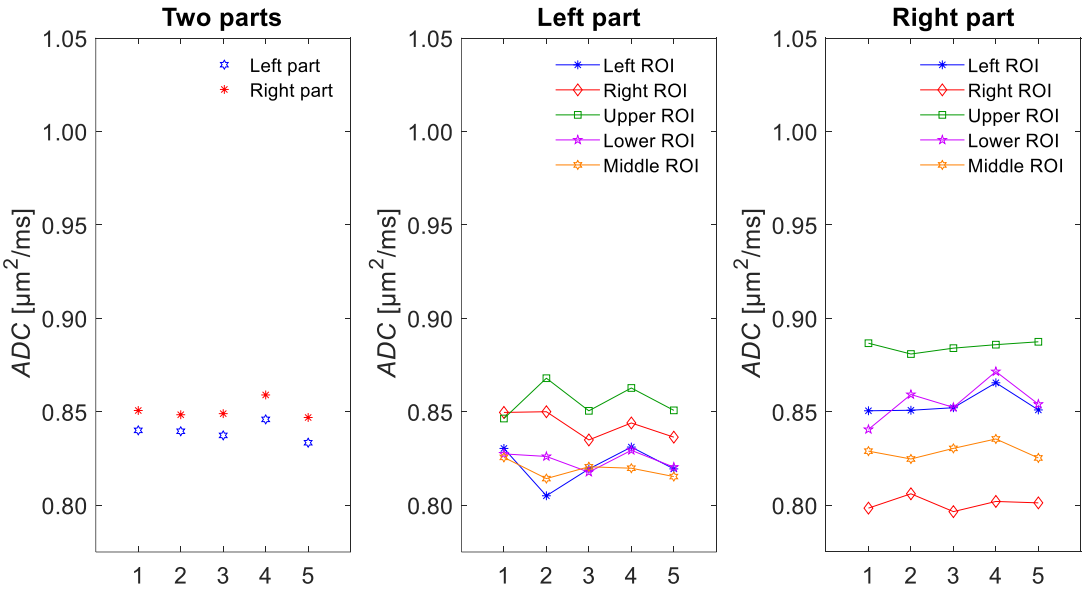

Figure 14. **SS-EPI$_5$** sequence with **monopolar** diffusion gradients and **parallel imaging** with a reduction factor of **7**. Plots shown from the left as follows: overall *ADC* in the left and right part of the phantom, *ADC* in the individual 5 ROIs segmented in the left part of the phantom, and *ADC* in the 5 ROIs in the right part of the phantom. The x-axis indicates measurement days.

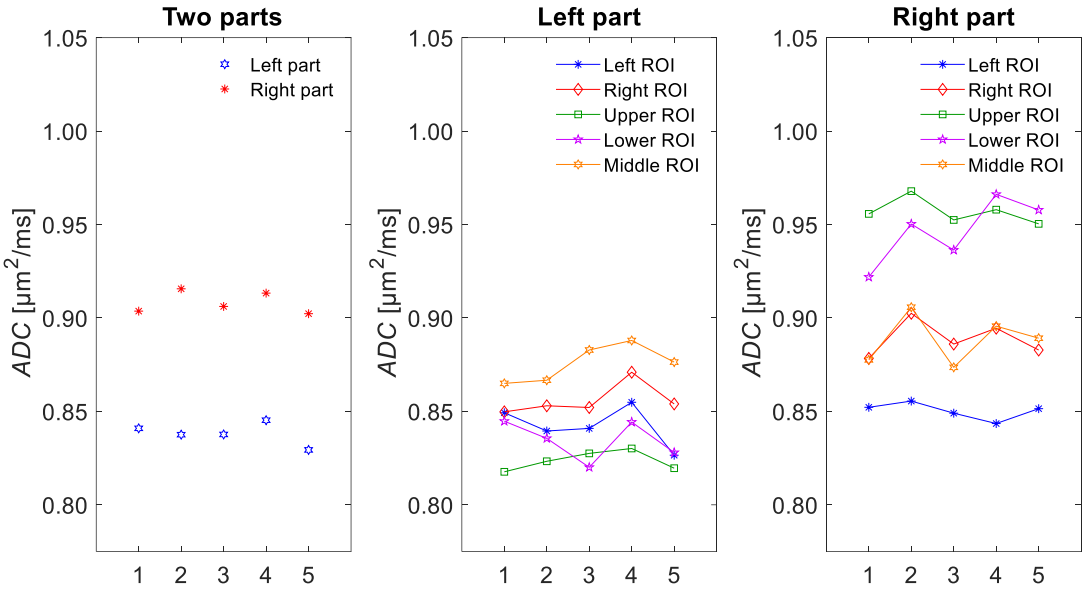

Figure 15. **SS-EPI$_6$** sequence with **bipolar** diffusion gradients and **parallel imaging** with a reduction factor of **7**. Plots shown from the left as follows: overall *ADC* in the left and right part of the phantom, *ADC* in the individual 5 ROIs segmented in the left part of the phantom, and *ADC* in the 5 ROIs in the right part of the phantom. The x-axis indicates measurement days.

For the SS-EPI sequence with GRAPPA = 2 and GRAPPA = 3, *CV* calculated for each ROI and measurement separately, for monopolar gradients was in the range of 0.52%–1.66% and 0.69%–1.52%, respectively. For bipolar gradients *CV* was higher in the range 0.55%–2.80% and 0.85%–2.55% respectively. The difference between the maximal and the minimal calculated *ADC* was, for monopolar gradients, equal to 0.065 μm^2/ms for GRAPPA = 2 and 0.041 μm^2/ms for GRAPPA = 3. For bipolar gradients the differences were twice as high, i.e. 0.122 μm^2/ms and 0.105 μm^2/ms, respectively. The mean *ADC* in individual ROIs, averaged over 5-day measurements was for monopolar gradients in the range of 0.834–0.886 μm^2/ms for GRAPPA = 2 (Figure 16) and 0.838–0.865 μm^2/ms for GRAPPA = 3 (Figure 17). For bipolar gradients the discrepancy was higher that means successively 0.840–0.953 μm^2/ms (Figure 18) and 0.859–0.954 μm^2/ms (Figure 19). Also the differences between the individual ROIs in the single measurements, which were in the range of 0.042–0.056 μm^2/ms for GRAPP = 2 and 0.026–0.031 μm^2/ms for GRAPPA = 3, were lower than 0.108–0.115 μm^2/ms and 0.096–0.098 μm^2/ms respectively for bipolar gradients.

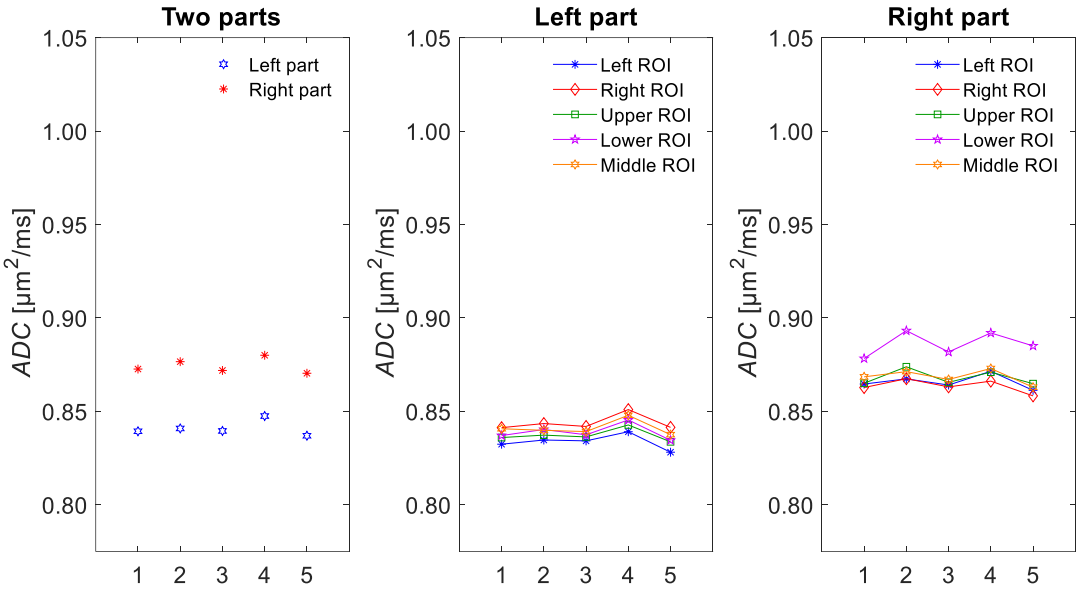

Figure 16. **SS-EPI$_1$** sequence with **monopolar** diffusion gradients and **parallel imaging** with a reduction factor of **2**. Plots shown from the left as follows: overall *ADC* in the left and right part of the phantom, *ADC* in the individual 5 ROIs segmented in the left part of the phantom, and *ADC* in the 5 ROIs in the right part of the phantom. The x-axis indicates measurement days.

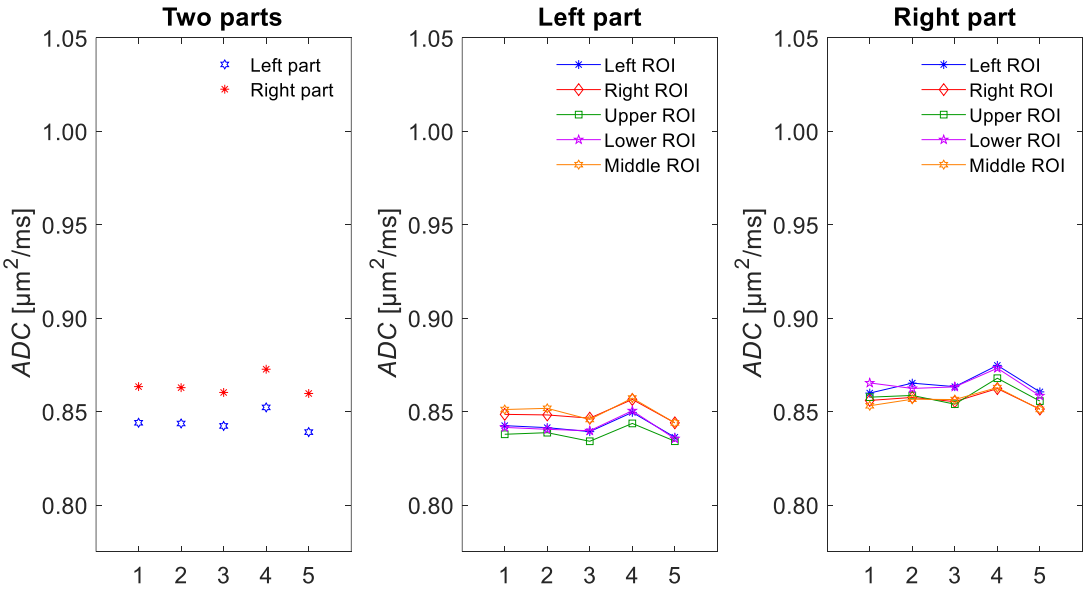

Figure 17. **SS-EPI$_3$** sequence with **monopolar** diffusion gradients and **parallel imaging** with a reduction factor of **3**. Plots shown from the left as follows: overall *ADC* in the left and right part of the phantom, *ADC* in the individual 5 ROIs segmented in the left part of the phantom, and *ADC* in the 5 ROIs in the right part of the phantom. The x-axis indicates measurement days.

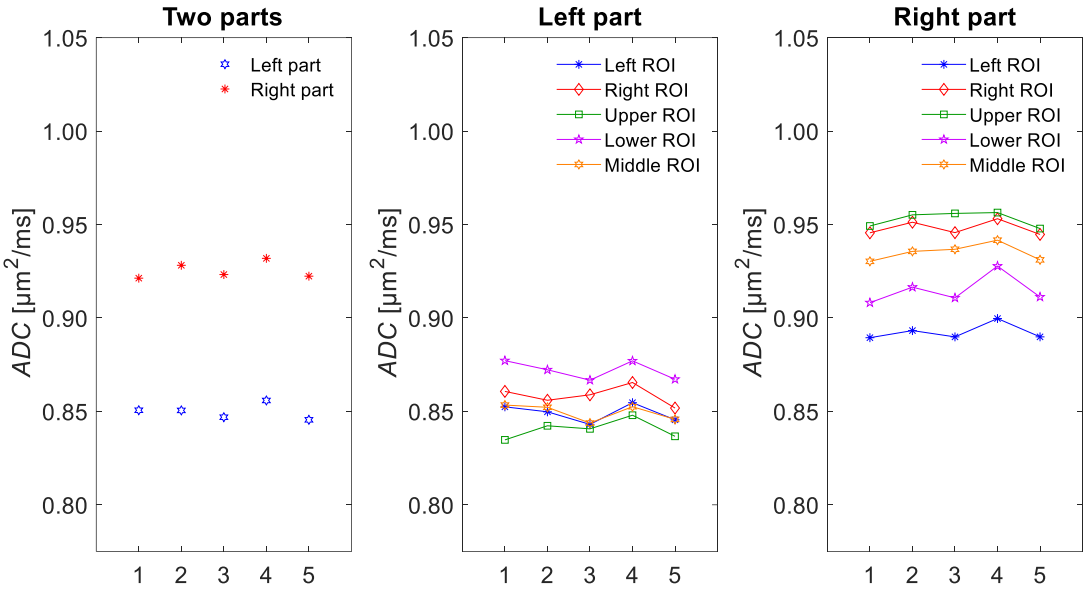

Figure 18. **SS-EPI$_2$** sequence with **bipolar** diffusion gradients and **parallel imaging** with a reduction factor of **2**. Plots shown from the left as follows: overall *ADC* in the left and right part of the phantom, *ADC* in the individual 5 ROIs segmented in the left part of the phantom, and *ADC* in the 5 ROIs in the right part of the phantom. The x-axis indicates measurement days.

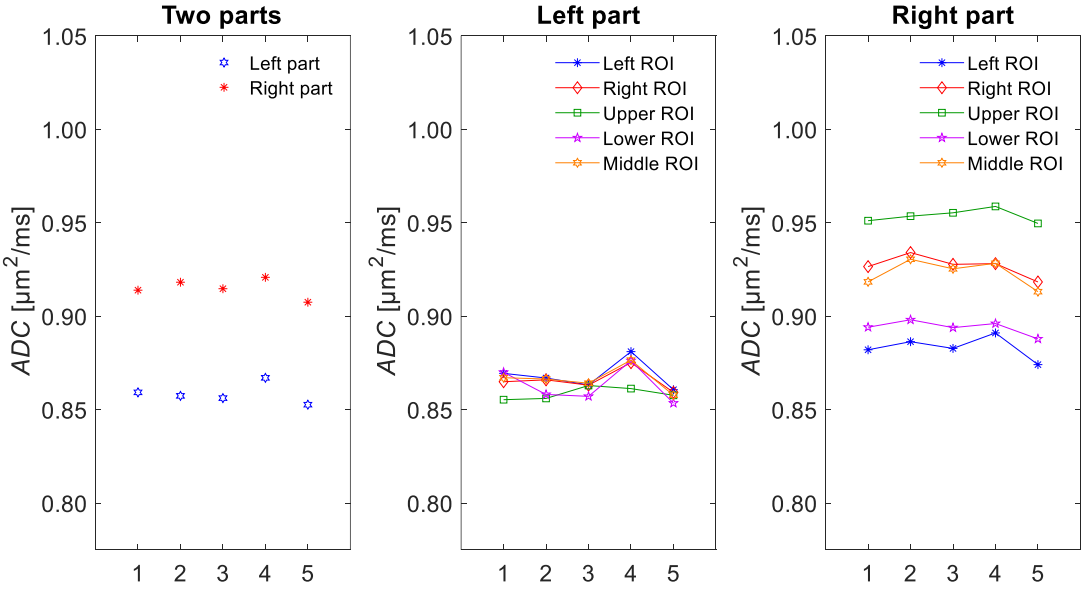

Figure 19. **SS-EPI$_4$** sequence with **bipolar** diffusion gradients and **parallel imaging** with a reduction factor of **3**. Plots shown from the left as follows: overall *ADC* in the left and right part of the phantom, *ADC* in the individual 5 ROIs segmented in the left part of the phantom, and *ADC* in the 5 ROIs in the right part of the phantom. The x-axis indicates measurement days.

For the SS-EPI sequence without parallel imaging, the relative variation in the individual ROI, considering separately each measurement, was comparable between monopolar (0.29% –0.96%) and bipolar (0.33%–0.91%) gradients. The difference between the maximal and the minimal observed *ADC* was 0.048 μm^2/ms for monopolar and was slightly below 0.060 μm^2/ms for bipolar gradients, however the differences are much lower than for the sequences with parallel imaging. The difference between the ROIs in the single measurements were in the range of 0.036–0.042 μm^2/ms for monopolar and 0.044–0.048 μm^2/ms for bipolar gradients. The mean *ADC* value for particular ROIs are presented in Figure 20 for monopolar and in Figure 21 for bipolar diffusion gradient.

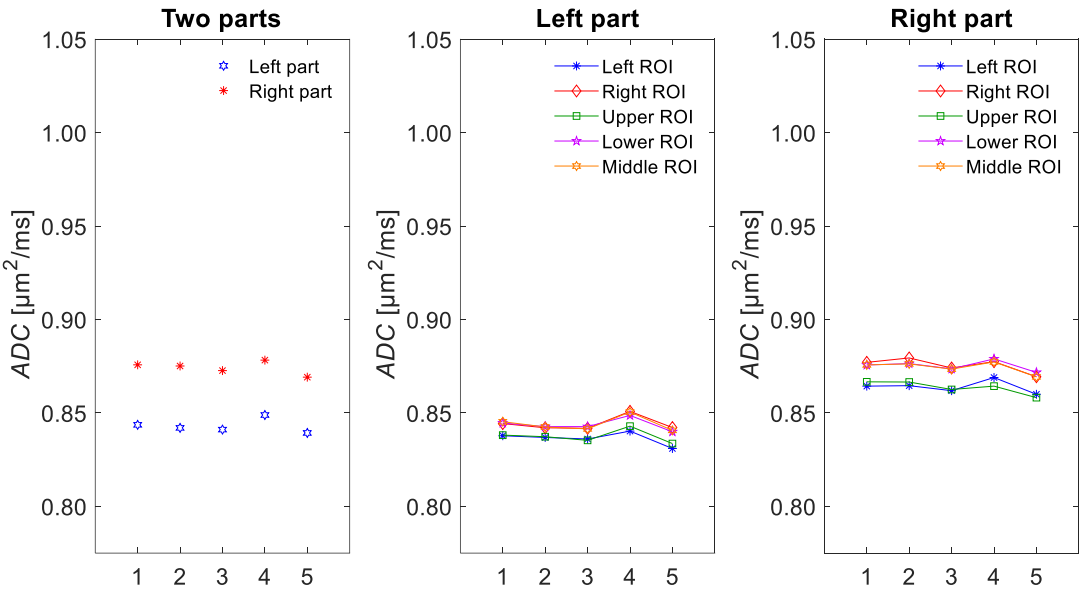

Figure 20. **SS-EPI$_7$** sequence with **monopolar** diffusion gradients and **without parallel imaging**. Plots shown from the left as follows: overall *ADC* in the left and right part of the phantom, *ADC* in the individual 5 ROIs segmented in the left part of the phantom, and *ADC* in the 5 ROIs in the right part of the phantom. The x-axis indicates measurement days.

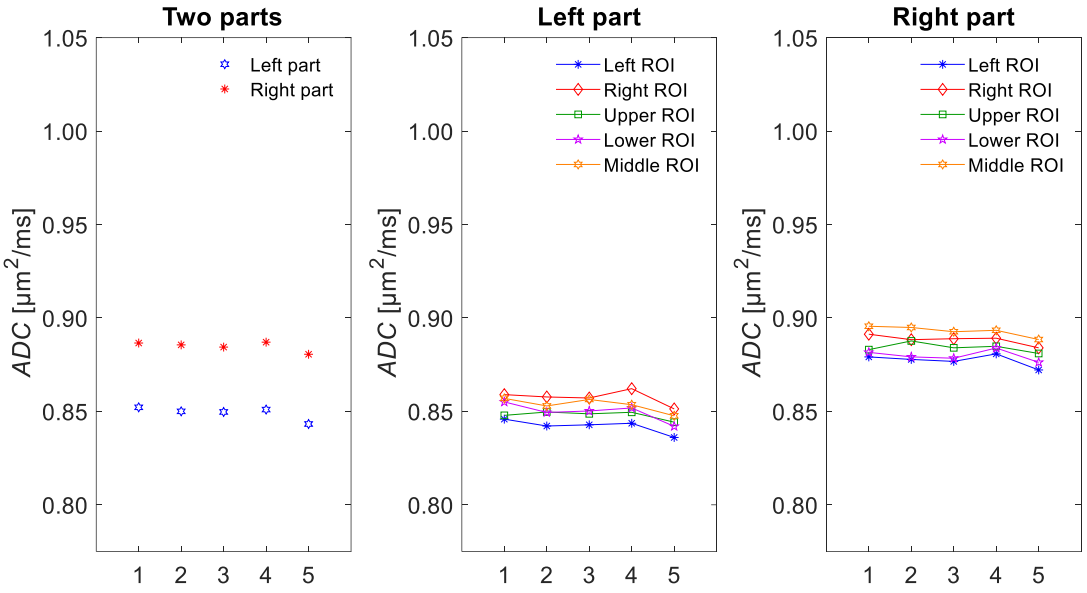

Figure 21. **SS-EPI$_8$** sequence with **bipolar** diffusion gradients and **without parallel imaging**. Plots shown from the left as follows: overall *ADC* in the left and right part of the phantom, *ADC* in the individual 5 ROIs segmented in the left part of the phantom, and *ADC* in the 5 ROIs in the right part of the phantom. The x-axis indicates measurement days.

In summary, the highest dispersion of *ADC* values, when considering the entire phantom, was observed for SS-EPI$_6$ sequence with bipolar diffusion gradients and parallel imaging with a reduction factor of 7, and a maximum *CV* of 8.69%. The highest deviations in *ADC* value between the ROIs on the same side of the coil was observed also for the same sequence, resulting in *CV* of 8.42% for the right side of the coil and 6.70% for the left side. On the other hand, the lowest dispersion of *ADC* value in the entire phantom was observed for RESOLVE$_1$ sequence with *CV* of 1.48%. The deviation between the ROIs on the same side of the coil was 1.48% for the right side of the coil and 0.78% for the left side of the coil.

5.2 Breast Phantom II

In this section the results of the second round of the measurements, using an improved version of the phantom and new DWI protocol are presented. The general *CV* for the whole phantom, taking the pixels from 10 ROIs together, over all 5-day measurements was lower for monopolar than for bipolar gradients (3.74% vs. 4.31%). Furthermore, comparing the single measurements, the relative variation was in the range of 3.40%–4.14% and 4.04%–4.61% respectively.

For both sequences, higher variation was observed in the right part of the phantom. Thus, relative variation within 5 measurements was 3.36%–3.70% for monopolar and 3.85%–

4.48% for bipolar gradients, whereas for the left part of the phantom it was as follows: 1.26%–1.52% and 1.69%–2.14%.

To analyze the differences between the internal regions of the phantom, the mean value was calculated for each of the 10 ROIs. *CV* among the *ADC* calculated for 10 ROIs and each of the 5 measurements was in the range of 0.57%–2.25% for monopolar and 0.67%–3.73% bipolar gradients. The difference between maximal and minimal *ADC* was 0.101 μm^2/ms and was identical for both sequences. However, the difference in the single measurements between the 10 ROIs for monopolar gradients were lower than for bipolar gradients (0.051–0.076 μm^2/ms vs. 0.071–0.093 μm^2/ms). The mean *ADC* averaged over 5 measurements for each ROI was in the range of 0.836–0.899 μm^2/ms for monopolar and 0.846–0.919 μm^2/ms for bipolar gradients. The mean *ADC* in 10 ROIs is presented in Figure 22 for monopolar and Figure 23 for bipolar diffusion gradient and for analogous sequences with motion correction option in Figure 24 and Figure 25, respectively.

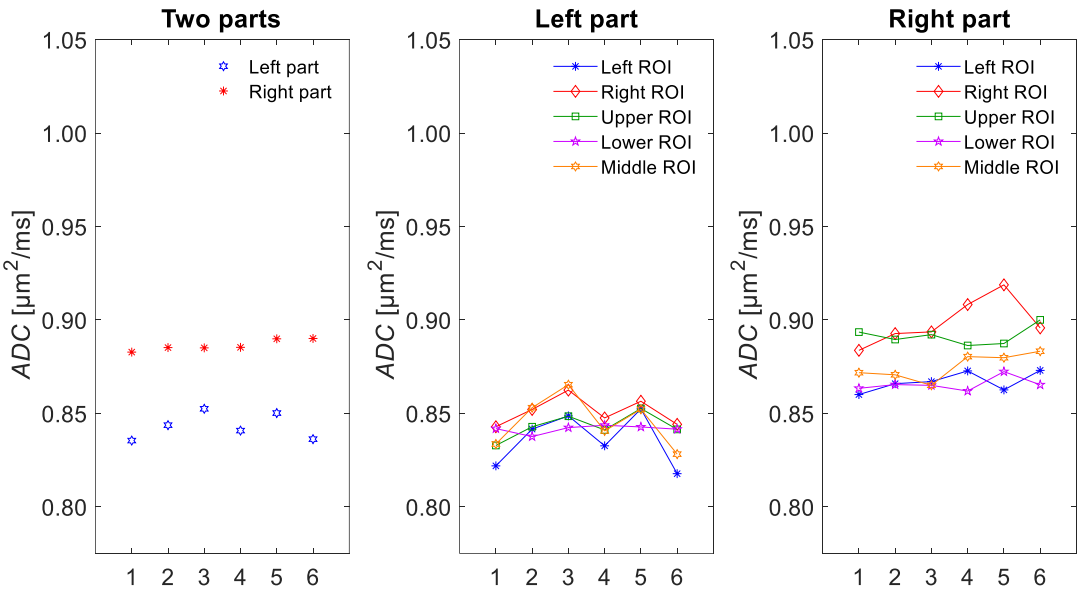

Figure 22. **WIP$_1$** sequence with **monopolar** diffusion gradients and **without parallel imaging**. From the left are shown as follows: overall *ADC* in the left and right part of the phantom, *ADC* in the individual 5 ROIs segmented in the left part of the phantom, and *ADC* in the 5 ROIs in the right part of the phantom. The x-axis indicates measurement days.

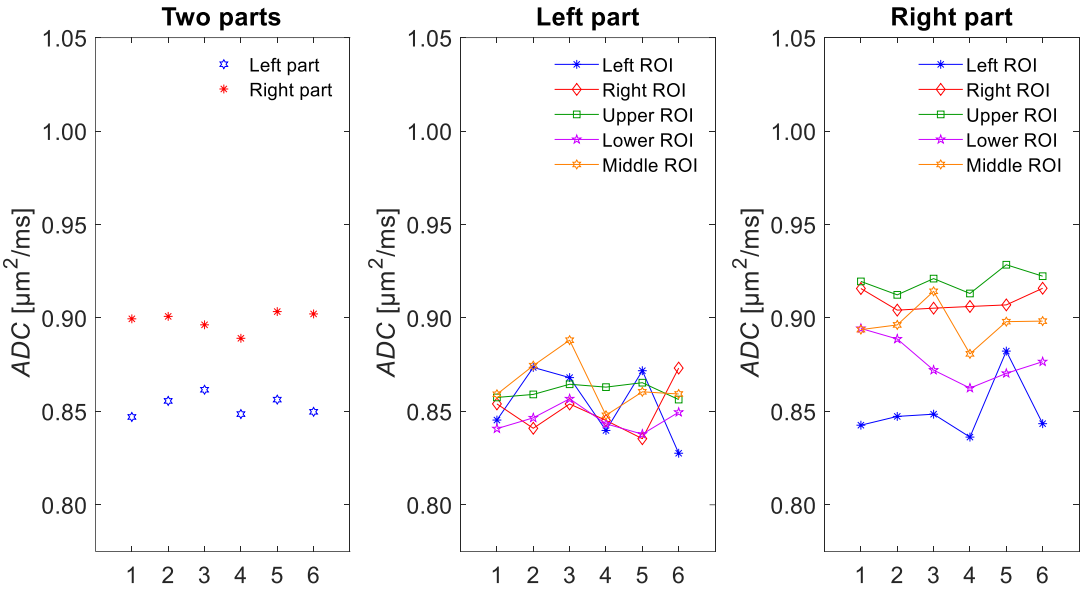

Figure 23. **WIP₂** sequence with **bipolar** diffusion gradients and **without parallel imaging**. From the left are shown as follows: overall *ADC* in the left and right part of the phantom, *ADC* in the individual 5 ROIs segmented in the left part of the phantom, and *ADC* in the 5 ROIs in the right part of the phantom. The x-axis indicates measurement days. The x-axis indicates measurement days.

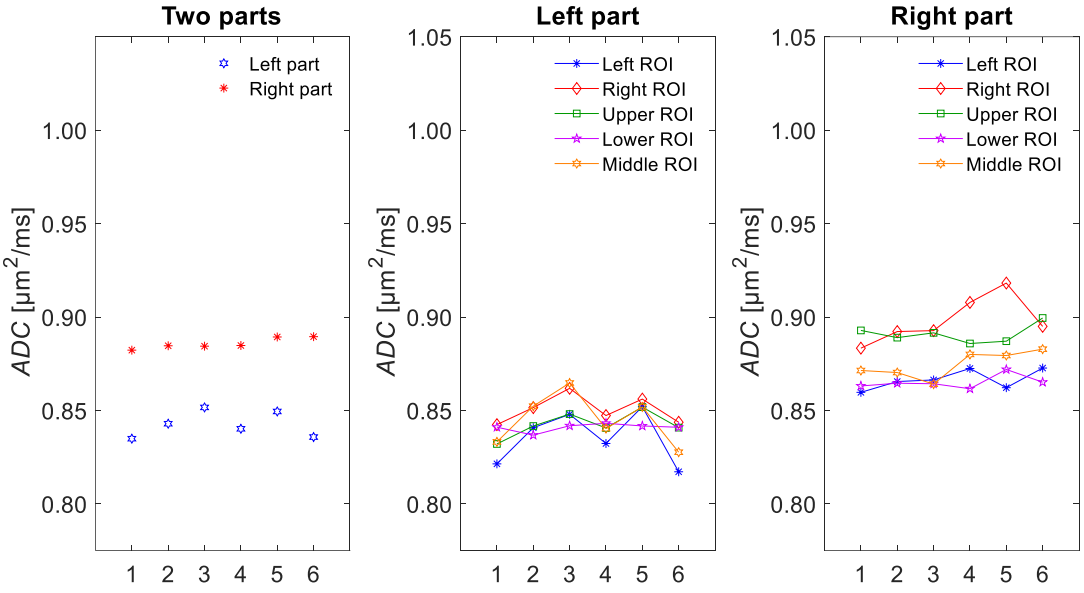

Figure 24. **WIP₃** sequence with **monopolar** diffusion gradients, **without parallel imaging**, but with the motion correction option. From the left are shown as follows: overall *ADC* in the left and right part of the phantom, *ADC* in the individual 5 ROIs segmented in the left part of the phantom, and *ADC* in the 5 ROIs in the right part of the phantom. The x-axis indicates measurement days.

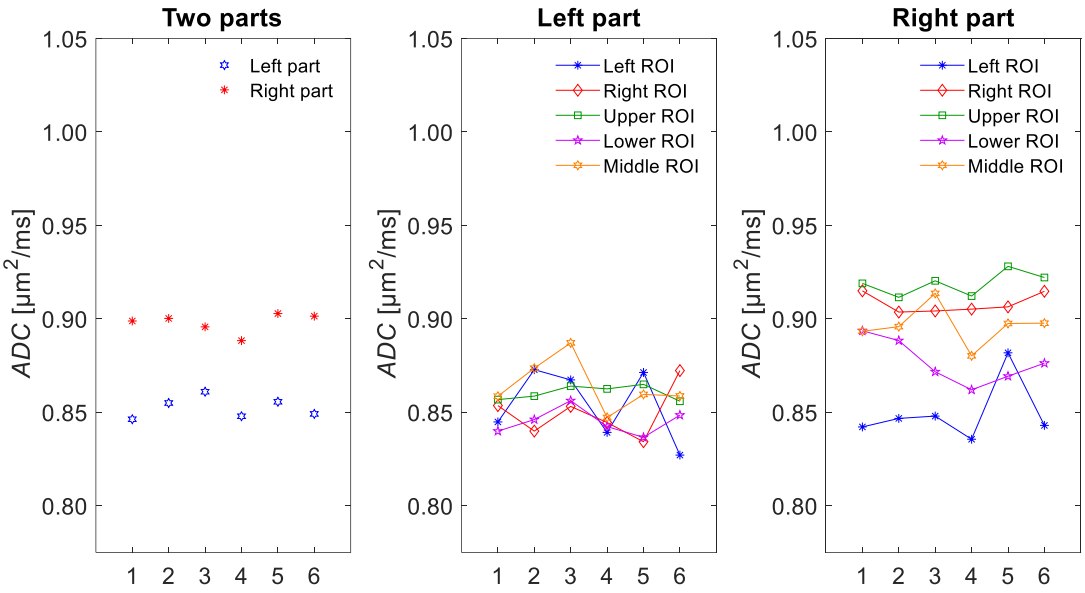

Figure 25. **WIP$_4$** sequence with **bipolar** diffusion gradients, **without parallel imaging**, but with the motion correction option. From the left are shown as follows: overall *ADC* in the left and right part of the phantom, *ADC* in the individual 5 ROIs segmented in the left part of the phantom, and *ADC* in the 5 ROIs in the right part of the phantom. The x-axis indicates measurement days.

5.3 Breast Lesions

This section presents the results of the use of the various fitting approaches in characterization of suspicious mammography findings. Most of the results presented in this section were published by Mlynarska-Bujny et al. (2020). The first subsections are devoted to methods accounting for constant level of fat-related contamination, which do not change with *b*-value (see Equations (4.8)–(4.11)). In the above mentioned sections, only the case of the maximal fat signal contribution (a = 1) in Method3 is considered, what is denoted with two asterisks (Method3**). The full evaluation of the extent of contamination with fat-related signal using Method3 is showed in Section 5.3.6. Section 5.3.6 presents also results of the Method5, which accounts for contamination with fat-related signal depending on *b*-value. Almost all subsections present the results of the ROC analysis for logistic regression models with two predictors. Only in Section 5.3.2 the results show the ROC analysis for a single coefficient.

According to the histopathological findings, the Group A consisted of 45 benign and 60 malignant lesions, whereas Group B of 32 benign and 61 malignant lesions. The median number of voxels of the benign lesions was 11 in Group A and 14 in Group B, whereas for malignant lesions 21 and 25, respectively.

5.3.1 Diffusion and Kurtosis Coefficients

Table 6 summarizes the values of the obtained diffusion and diffusion kurtosis coefficients. For methods 1–4, the diffusion coefficient D_i was significantly lower in malignant lesions than in benign lesions ($p < 0.001$). On the contrary, the diffusion kurtosis coefficient K_i in malignant lesions was significantly higher ($p < 0.001$) than in benign lesions. The graphical representation of the distribution of values in the box-plot graphs is presented in Figure 26. It can be observed that the values of diffusion and diffusion kurtosis coefficients are more dispersed in Group A than in Group B. Looking at the median value, one can conclude that the methods applying fat-related correction factor result in a higher diffusion coefficient and lower diffusion kurtosis coefficient than in case of standard methods.

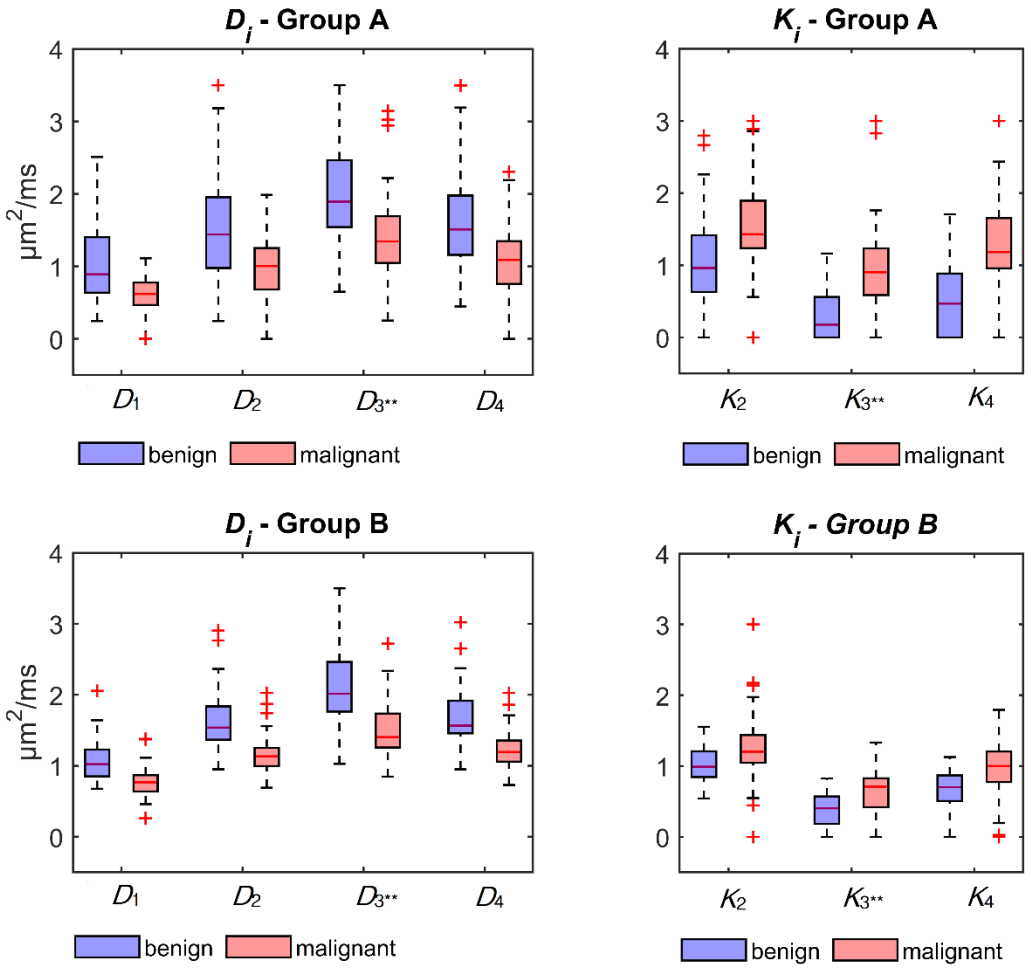

Figure 26. Graphical representation of diffusion D_i and diffusion kurtosis K_i coefficients derived by fitting methods 1–4 for Group A (upper row) and Group B (lower row). Reproduced from (Mlynarska-Bujny et al. 2020).

Table 6. Diffusion and diffusion kurtosis coefficients derived by fitting methods 1–4; (*b* – benign lesions, *m* – malignant lesions).

	Group A					Group B				
	mean	**std**	**median**	**min**	**max**	**mean**	**std**	**median**	**min**	**max**
D_{1b}	1.04	0.56	0.89	0.25	2.51	1.08	0.32	1.02	0.68	2.05
D_{1m}	0.58	0.26	0.62	0.00	1.11	0.76	0.20	0.77	0.26	1.38
D_{2b}	1.52	0.73	1.44	0.25	3.50	1.67	0.46	1.54	0.95	2.91
D_{2m}	0.95	0.46	1.00	0.00	1.99	1.14	0.25	1.13	0.69	2.03
D_{3b}^{**}	1.98	0.70	1.89	0.65	3.50	2.15	0.56	2.09	0.96	3.50
D_{3m}^{**}	1.37	0.59	1.35	0.25	3.14	1.47	0.34	1.41	0.82	2.32
D_{4b}	1.61	0.70	1.51	0.45	3.50	1.76	0.45	1.66	0.95	3.09
D_{4m}	1.04	0.48	1.09	0.00	2.31	1.21	0.26	1.20	0.73	2.04
K_{2b}	1.05	0.65	0.96	0.00	2.80	1.03	0.27	0.99	0.54	1.55
K_{2m}	1.56	0.72	1.43	0.00	3.00	1.25	0.49	1.20	0.00	3.00
K_{3b}^{**}	0.33	0.39	0.18	0.00	1.16	0.38	0.25.	0.40	0.00	0.82
K_{3m}^{**}	0.98	0.74	0.90	0.00	3.00	0.61	0.35	0.71	0.00	1.33
K_{4b}	0.54	0.53	0.47	0.00	1.71	0.67	0.28	0.70	0.00	1.13
K_{4m}	1.25	0.74	1.18	0.00	3.00	0.94	0.44	1.00	0.00	1.79

5.3.2 ROC Analysis of D_i and K_i

At first, the diagnostic performance of the diffusion and diffusional kurtosis coefficients as single predictors was analyzed.

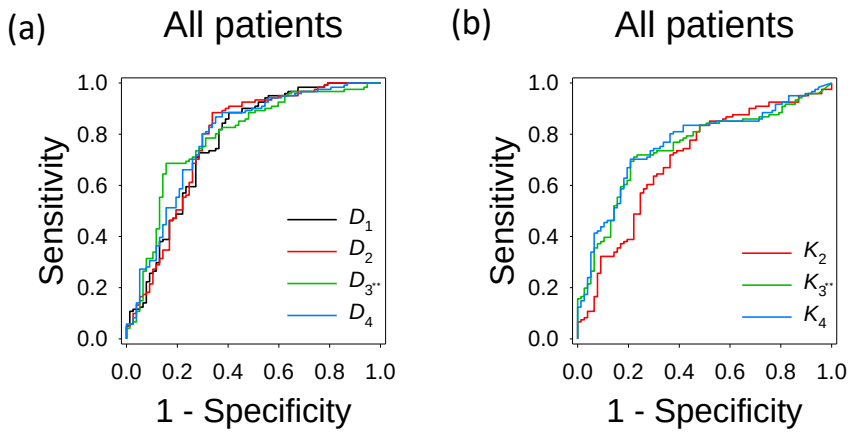

Figure 27. ROC curves for diffusion (a) and kurtosis coefficients (b) for all patients derived by fitting methods 1–4.

Figure 27 shows the ROC curves for diffusion and diffusional kurtosis coefficients, taking the entire study collective into account. The ROC analysis performed for single parameter revealed no statistically significant differences in AUC between the D_i, while for K_i the differences could be observed between Method2 and Method4 (0.76 vs. 0.70, $p = 0.049$). At the cut-off point for sensitivity 95% the specificity for diffusion coefficients oscillated around 40%, whereas for diffusion kurtosis coefficients the specificity was rather low. The ROC statistic is summarized in Table 7.

Table 7. ROC statistics for D_i and K_i . In the brackets, 95% confidence intervals are shown.

	D_i		K_i	
Method	**AUC**	**Specificity***	**AUC**	**Specificity***
1	0.77 [0.70–0.84]	44% [33%–56%]	-	-
2	0.78 [0.70–0.85]	40% [29%–52%]	0.70 [0.63–0.78]	13% [6%–23%]
3**	0.79 [0.72–0.85]	38% [27%–49%]	0.75 [0.68–0.82]	12% [5%–21%]
4	0.79 [0.72–0.85]	39% [28%–51%]	0.76 [0.69–0.83]	17% [9%–27%]

*Specificity at the cut-off point for 95% sensitivity

**results for the maximal fat signal contribution ($a = 1$)

5.3.3 ROC Analysis of Multiple Logistic Regression Models

The diagnostic accuracy improved dramatically after combining diffusion and diffusion kurtosis coefficients in logistic regression model with two predictors. As shown in Table 8, the highest AUC was observed for both methods with fat correction factor. The differences in AUC between Method3** and standard Method1 or Method2 were statistically significant ($p < 0.015$). For Method4, the difference was statistically significant when compared with Method1 ($p = 0.020$), but for Method2 it was at the margin of statistical significance ($p = 0.068$). No statistically significant difference was observed between Method3 and Method4. At the cut-off point for 95% sensitivity, the highest specificity of 52% (95%CI 40–63) was observed for Method4.

Next, the analysis by the study site was performed. In Group A it reveals the highest AUC for Method3** (0.86 (95%CI 0.79–0.93)) and Method 4 (0.85 (95%CI 0.78–0.93)). However, in a pairwise comparison statistically significant differences in AUC can be observed between Method4 and both standard approaches ($p < 0.035$). At the cut-off point at 95% sensitivity, Method4 presents the highest specificity of 58% (95%CI 42–72) in comparison to 49% (95%CI 34–64) for Method3**, 33% (95%CI 20–49) for diffusion kurtosis and 38%

(95%CI 24–53) for standard diffusion equation. Although Method4 also presented the highest specificity at the 95% sensitivity among all fitting methods in the Group B, no statistically significant differences in AUC between the models with fat correction factor and standard fitting approaches were observed for this cohort of patients.

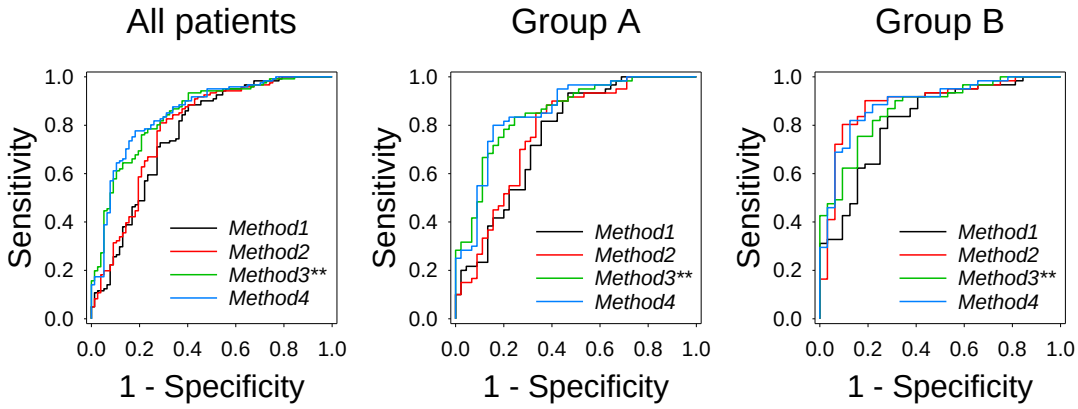

Figure 28. ROC curves for fitting methods 1–4. Reproduced from (Mlynarska-Bujny et al. 2020).

Table 8. ROC statistics for logistic regression with two predictors – diffusion and diffusion kurtosis coefficient (fitting Methods 2–4) and diffusion coefficient as a single predictor (Method1). 95% confidence interval in the brackets.

AUC [95%CI]			
Method	**All**	**Group A**	**Group B**
1*	0.77 [0.70–0.84]	0.76 [0.66–0.86]	0.82 [0.73–0.91]
2	0.79 [0.72–0.86]	0.77 [0.68–0.87]	0.89 [0.82–0.97]
3**	0.85 [0.79–0.90]	0.85 [0.78–0.93]	0.87 [0.80–0.94]
4	0.85 [0.80–0.91]	0.86 [0.78–0.93]	0.89 [0.82–0.96]
Specificity at the 95% sensitivity [95%CI]			
Method	**All patients**	**Group A**	**Group B**
1*	44% [33%–56%]	38% [24%–53%]	44% [26%–62%]
2	38% [27%–49%]	33% [20%–49%]	47% [29%–65%]
3**	45% [34%–57%]	49% [34%–64%]	41% [24%–59%]
4	52% [40%–63%]	58% [42%–72%]	50% [32%–68%]

*results for logistic regression with diffusion coefficient as a single predictor
**results for the maximal fat signal contribution (a = 1)

5.3.4 Lesion-to-Background Ratio

As a next step, the patients were divided into the three subgroups according to the lesion-to-background ratio (Equation (4.13)) using two thresholds of 1.5 and 2.0 ($LBR < 1.5$, $1.5 \leq LBR < 2$ and $LBR \geq 2$). The thresholds were set up in such a way to get an equal number of the patients in the subgroups. The descriptive statistics of *LBR* parameter were summarized in Table 9.

The ROC curves for multiple logistic regression models with diffusion and diffusion kurtosis coefficient as predictors are presented in Figure 29. At first, let us take into consideration the subgroups with the low *LBR*. The ROC curves analysis showed the highest AUC for Method4 for the full cohort of patients. In the individual analysis by the study site, in the Group A the differences in AUC between standard and fat-corrected methods are even more prominent, albeit not statistically significant like also in the case of the full cohort. Notwithstanding, at the cutoff points yielding around 90% sensitivity, in the Group A the highest specificity was observed for Method4 (see Figure 29). However, in the Group B the highest sensitivity was found for standard Method2, followed by Method4. It is worth mentioning that 85% of the lesions in the subgroup with the low *LBR* in the Group A were poorly visible on $b = 1500$ s/mm^2 image and therefore segmented on $b = 750$ s/mm^2 image. In the Group B it was only 44%. The proportion of benign lesions in the subgroups is decreasing with *LBR* value, which is consistent with the expectations as malignant lesions present higher signal on high *b*-value DWI. The differences in AUC between the methods accounting for residual fat signal and standard diffusion and diffusion kurtosis approaches decrease for the patients with middle *LBR*, whereas for high *LBR* patients no additive effect of correction factor was observed. The AUC values are summarized in Table 9.

Table 9. Descriptive statistics of the *LBR* values for the subgroups obtained by *LBR* thresholds.

Group A	**mean ± std**	**min**	**max**	**benign**	**malignant**
$LBR < 1.5$	1.21 ± 0.16	0.86	1.47	22	13
$1.5 \leq LBR < 2$	1.74 ± 0.15	1.54	1.98	13	13
$LBR \geq 2$	2.78 ± 0.91	2.03	6.41	10	34
Group B	**mean ± std**	**min**	**max**	**benign**	**malignant**
$LBR < 1.5$	1.28 ± 0.14	0.93	1.49	16	11
$1.5 \leq LBR < 2$	1.77 ± 0.14	1.51	1.99	10	18
$LBR \geq 2$	2.50 ± 0.44	2.00	3.74	6	32

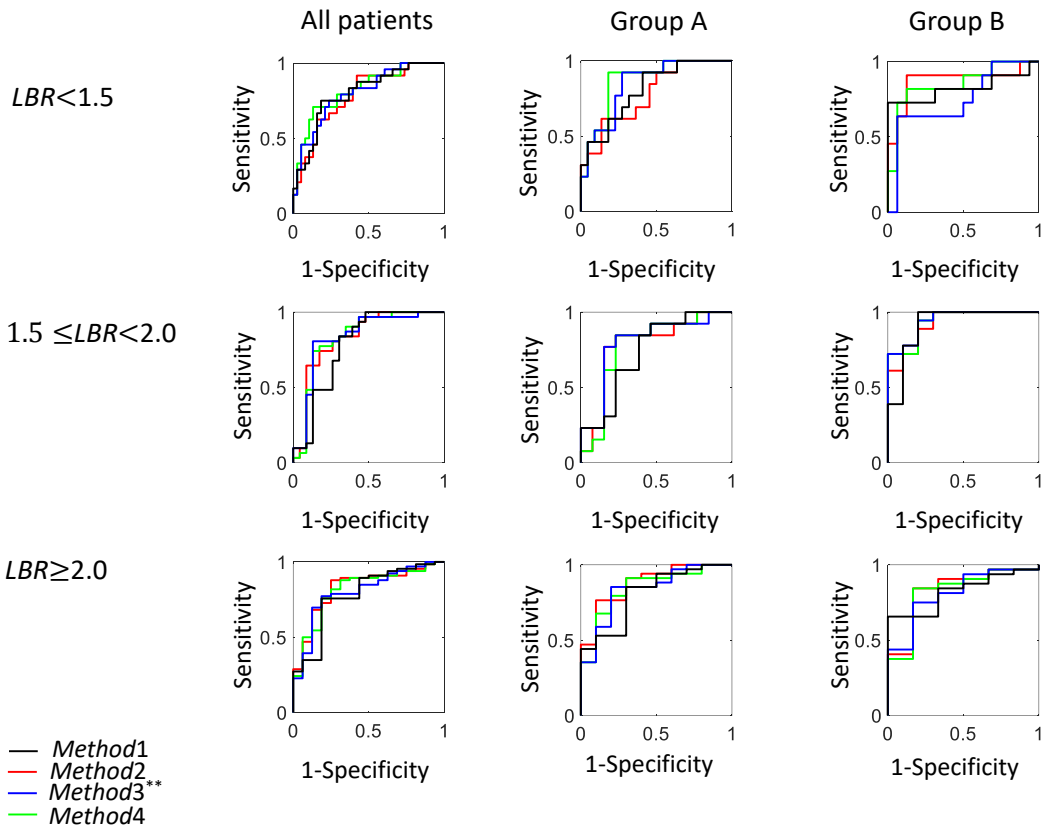

Figure 29. ROC curves for multiple logistic regression models with diffusion and diffusion kurtosis coefficients as predictors for patients divided into three groups according to *LBR*. In the first column are ROC curves for all patients, in the second for Group A only and in the third for Group B.

Table 10. AUC for logistic regression over D_i and K_i for the different *LBR* subgroups. 95% confidence intervals in the brackets.

	All	**Group A**	**Group B**
Method		***LBR* < 1.5**	
1*	0.80 [0.69–0.91]	0.81 [0.66–0.95]	0.82 [0.62–1.03]
2	0.78 [0.67–0.90]	0.78 [0.62–0.94]	0.88 [0.71–1.04]
3**	0.80 [0.69–0.91]	0.85 [0.72–0.98]	0.74 [0.54–0.95]
4	0.82 [0.71–0.93]	0.87 [0.75–0.99]	0.85 [0.69–1.01]
Method		**1.5 ≤ *LBR* < 2.0**	
1*	0.78 [0.64–0.92]	0.74 [0.54–0.94]	0.92 [0.79–1.05]
2	0.83 [0.71–0.95]	0.78 [0.58–0.98]	0.92 [0.82–1.02]
3**	0.83 [0.71–0.96]	0.80 [0.61–0.99]	0.94 [0.87–1.02]
4	0.83 [0.71–0.96]	0.78 [0.58–0.97]	0.94 [0.85–1.03]
Method		***LBR* ≥ 2.0**	
1*	0.78 [0.65–0.91]	0.81 [0.65–0.96]	0.82 [0.68–0.97]
2	0.83 [0.72–0.94]	0.88 [0.76–1.00]	0.83 [0.64–1.02]
3**	0.80 [0.68–0.92]	0.84 [0.69–0.98]	0.81 [0.63–1.00]
4	0.82 [0.70–0.93]	0.84 [0.70–0.99]	0.82 [0.63–1.02]

*results for logistic regression with diffusion coefficient as a single predictor

**results for the maximal fat signal contribution (a = 1)

5.3.5 Accounting for Noise Contamination

In this subsection the results of the adapted approach accounting for residual fat-related signal, given by Equation (4.11), are compared with the original method applying correction factor for background noise, given by Equation (2.14). As already mentioned in Chapter 4, this comparison is possible only for the patients from Group B. The method accounting for noise contamination is denoted as Method4'. As an estimation of the background noise level, the mean value in the third ROI was taken.

Table 11 summarizes the values of diffusion and diffusion kurtosis coefficients obtained with Method4'. When comparing these values with Table 6 it can be observed that the diffu-

sion coefficients derived by Method4' seem to have slightly lower values than these derived by Method4, but are still slightly higher than the diffusion coefficient obtained with Method2. On the other hand, the diffusion kurtosis coefficients derived by Method4' seem to have slightly higher values than these derived by Method4, but lower than these obtained by Method2. However, the ROC analysis for multiple logistic regression with diffusion and diffusion kurtosis coefficient derived by Method4' revealed the AUC of 0.89 (95%CI 0.82–0.97) and the specificity of 53% (95%CI 35–71) at the cut-off point at the 95% sensitivity. This results in the same AUC value and slightly higher specificity than these achieved with Method4 and Method2 (see Table 8).

Table 11. Statistics of diffusion and diffusion kurtosis parameters derived by Method4' with primary noise correction factor; (b – benign lesions, m – malignant lesions).

	Group B				
	mean	**std**	**median**	**min**	**max**
$D_{4'b}$	1.72	0.45	1.57	0.95	2.99
$D_{4'm}$	1.17	0.25	1.15	0.72	2.03
$K_{4'b}$	0.90	0.21	0.86	0.49	1.32
$K_{4'm}$	1.10	0.45	1.10	0.00	2.27

5.3.6 Fractionated Fat-Related Signal Contribution

This subsection shows the results obtained with Method3 and Method5. At first, the results obtained with Method3, with the *a* factor varying from 0.1 to 1.0 with 0.1 step size, are shown. The increasing value of weighting factor *a* corresponds to the higher contribution of the fat signal into the overall signal measured in the lesion area. Table 12 summarizes the ROC analysis for logistic regression models with diffusion and diffusion kurtosis coefficients as predictors. For the full cohort of patients, the highest AUC was observed for the highest *a* factor. Moreover, the AUC values increase with the increasing *a* factor. In the individual analysis by the study side, in Group A, also incorporating higher fraction of the fat signal into the signal decay fitting equation results in the higher AUC. On the other hand, in Group B the highest *a* factor revealed the smallest AUC, whereas the maximal AUC was found for the middle range *a* factor.

Table 12. AUC values for Method3 with varying fat contribution.

a	**0.1**	**0.2**	**0.3**	**0.4**	**0.5**	**0.6**	**0.7**	**0.8**	**0.9**	**1.0**
All	0.79	0.80	0.81	0.81	0.82	0.83	0.84	0.85	0.85	0.85
Group A	0.78	0.79	0.80	0.80	0.81	0.83	0.85	0.85	0.85	0.85
Group B	0.89	0.89	0.89	0.90	0.90	0.90	0.89	0.89	0.88	0.87

In Method5, increasing value of the weighting factor *f* expresses the decreasing contribution of the relative residual fat signal to the overall signal measured in the lesion area. Table 13 shows the obtained AUC value for multiple logistic regression model with D_5 and K_5 as predictors. In the full cohort study, as well as in the individual analysis by the study site, the maximal AUC value was reached for the $f = 1$ which corresponds to the Method2 without fat correction factor.

Table 13. AUC values for models with fractionated fat contribution. Higher *f*-value corresponds to the higher contribution from the signal in lesion and lower from fatty tissue area. $f = 1$ relates to the entire contribution from signal in the lesion.

f	**0.1**	**0.2**	**0.3**	**0.4**	**0.5**	**0.6**	**0.7**	**0.8**	**0.9**	**1.0**
All	0.59	0.61	0.63	0.69	0.74	0.75	0.77	0.78	0.79	0.79
Group A	0.67	0.68	0.69	0.70	0.70	0.71	0.74	0.75	0.77	0.77
Group B	0.77	0.78	0.80	0.81	0.83	0.82	0.84	0.86	0.88	0.89

5.4 Ovarian Lesions

This section is devoted to the results of the study analyzing the performance of DKI in differentiation of benign from malignant ovarian lesions. Most of the results presented here were published by Mokry et al. (2020). Histopathological examination performed on resected ovarian tissue resulted in 62 benign and 17 malignant lesions. The following subsections 5.4.1–5.4.2 present the results of the analysis based on the selected 1% of the voxels with the highest intensity on the $b = 1500$ mm^2/s images. Sections 5.4.3–5.4.4 show the results of an analogical analysis for 10% of the voxels with the highest intensity on the $b = 1500$ mm^2/s images. Subsection 5.4.5 is devoted to the results obtained for a reduced cohort of patients.

5.4.1 Diffusion and Diffusional Kurtosis Parameters – 1% of the Voxels

Table 14 presents the summary statistics of voxels used in the calculations of the *DWI* and *DKI* coefficients.

Table 14. Summary statistics of the 1% voxel fraction used in calculations of parameters derived by diffusion and diffusion kurtosis fitting model, expressed as percentage and numbers.

	benign % of voxels	**malignant % of voxels**	**benign number of voxels**	**malignant number of voxels**
	median [min, max]	**median [min, max]**	**median [min, max]**	**median [min, max]**
ADC	0.98 [0.55, 4.15]	0.96 [0.86, 6.36]	14 [11, 121]	23 [11, 84]
D_{app}, K_{app}	0.96 [0.46, 3.56]	0.94 [0.69, 6.36]	13 [11, 119]	23 [11, 84]

The distribution of diffusion and kurtosis coefficients is shown in Figure 30. The average difference in *DWI*-derived and *DKI*-derived parameters between benign and malignant lesions was calculated using a linear mixed model, and is summarized in Table 15. The *ADC* in malignant lesions was on average lower by 0.45 μm²/ms (95%CI 0.11–0.78) than in benign lesions. Similarly, the D_{app} was on average lower by 0.55 μm²/ms (95%CI 0.12–0.98) in malignant lesions in comparison to the benign ones. On the contrary, the kurtosis coefficient in malignant lesions was on average higher by 0.27 (95%CI 0.14–0.41) than in benign lesions. All differences were statistically significant ($p < 0.02$).

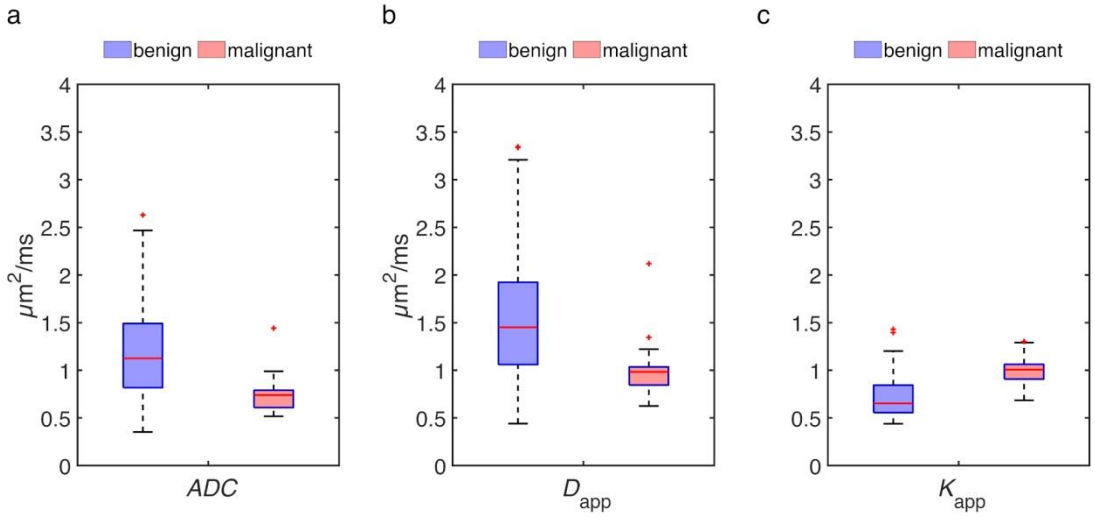

Figure 30. Distribution of *ADC* parameter (a) and *DKI*-derived parameters (b and c) in benign and malignant lesions for 1% the voxels. Reproduced, with permission, from (Mokry et al. 2020).

Table 15. Statistics of the parameters derived by diffusion and diffusion kurtosis fitting model for 1% the voxels

	benign	**malignant**	**difference derived by linear mixed model**	***p****
	median [min, max]	**median [min-max]**	**average difference between malignant and benign [95%CI]**	
ADC [μm²/ms]	1.13 [0.35, 2.63]	0.74 [0.52, 1.44]	-0.45 [-0.78, -0.11]	0.011
D_{app} [μm²/ms]	1.45 [0.44, 3.34]	0.98 [0.63, 2.12]	-0.55 [-0.98, -0.12]	0.016
K_{app}	0.65 [0.44, 1.43]	1.01 [0.69, 1.30]	0.27 [0.14, 0.41]	0.0003

5.4.2 Mixed Logistic Model – 1% of the Voxels

The statistics of the ROC curves (Figure 31) based on the parameters derived by mixed logistic model with *DWI*-derived and *DKI*-derived parameters is summarized in Table 16.

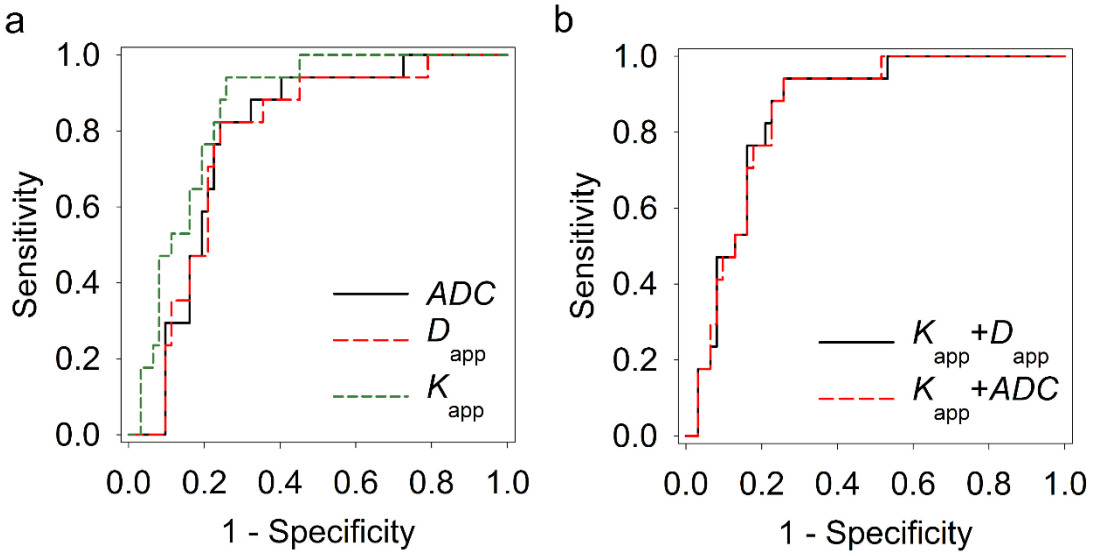

Figure 31. ROC curves for 1% of the voxels (a – single predictor model, b – two predictors model). Reproduced, with permission, from (Mokry et al. 2020).

Table 16. Summary of diagnostic performance of mixed logistic models with diffusion and kurtosis coefficient as predictors in differentiating malignant from benign ovarian lesions for 1% the voxels.

MLM parameters	**AUC**	***p****	**Sensitivity 100% (CI95% 80-100)**	**Sensitivity 94% (CI95% 71-100)**	**Sensitivity 88% (CI95% 64-99)**
ADC	0.78 (CI95% 0.67–0.89)	0.047	27% (CI95% 17–40)	60% (CI95% 46–72)	68% (CI95% 55–79)
D_{app}	0.77 (CI95% 0.66–0.89)	0.053	21% (CI95% 12–33)	55% (CI95% 42–68)	65% (CI95% 51–76)
K_{app}	0.85 (CI95% 0.77–0.94)	–	55% (CI95% 42–68)	74% (CI95% 62–84)	76% (CI95% 63–86)
K_{app}+D_{app}	0.85 (CI95% 0.77–0.94)	1.00	47% (CI95% 34–60)	74% (CI95% 62–84)	77% (CI95% 65–87)
K_{app}+*ADC*	0.85 (CI95% 0.77–0.94)	0.89	48% (CI95% 36–61)	74% (CI95% 62–84)	77% (CI95% 65–87)

*p-value for AUCs comparison to AUC for K_{app}

Among the mixed logistic models with single predictor, kurtosis coefficient achieved the highest AUC value of 0.85 (CI95% 0.77–0.94) in comparison to apparent diffusion coefficient 0.78 (CI95% 0.67–0.89) and diffusion kurtosis coefficient with AUC of 0.77 (CI95% 0.66–0.89). The difference in AUC between K_{app} and *ADC* is statistically significant (p = 0.047), but between K_{app} and D_{app} slightly outside the accepted statistical significance level (p = 0.053). Aiming for a sensitivity of 100% (CI95% 80-100), the corresponding specificity was 27% (CI95% 17–40) for *ADC* and 21% (CI95% 12–33) for D_{app}, whereas for K_{app} the sensitivity was 55% (CI95% 42–68). Combining K_{app} with *ADC* or D_{app} by building GLMM models with two predictors, did not improve the *AUC* and resulted in a lower specificity at the 100% sensitivity in comparison to K_{app} alone.

5.4.3 Diffusion and Kurtosis Parameters – 10% of the Voxels

Summary statistics of the number of pixels used for calculations when 10% of the voxels were selected is presented in Table 17.

Table 17. Summary statistics of the 10% voxel fraction used in calculations of parameters derived by diffusion and diffusion kurtosis fitting model, expressed as percentage and numbers.

	benign % of voxels	**malignant % of voxels**	**benign number of voxels**	**malignant number of voxels**
	median [min, max]	**median [min, max]**	**median [min, max]**	**median [min, max]**
ADC	9.09 [3.84, 9.98]	9.70 [8.14, 9.94]	117.5 [31, 1160]	235 [17, 889]
D_{app}, K_{app}	8.36 [1.77, 9.89]	9.58 [6.98, 9.94]	97 [12, 1035]	233 [17, 885]

The *ADC* in malignant lesions was on average lower by 0.56 (95%CI 0.18–0.93) than in benign lesion, whereas D_{app} was on average lower by 0.62 (95%CI 0.21–1.02). On the contrary, the K_{app} was on average higher by 0.21 (95%CI 0.073–0.34) in malignant lesions than in the benign ones. All differences in parameters between benign and malignant lesions were statistically significant (p<0.001). The summary statistics of the parameters is presented in Table 17. The distribution of parameters is shown in Figure 32.

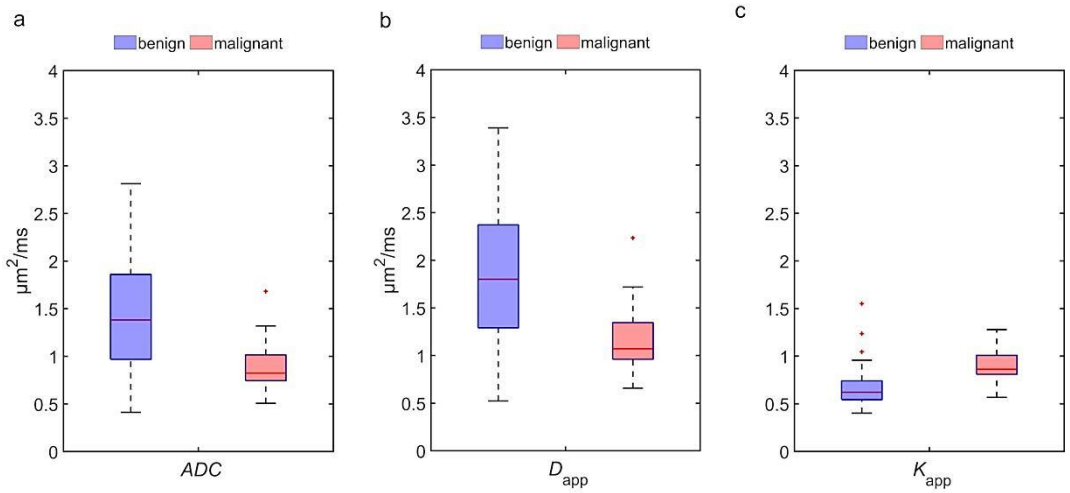

Figure 32. Distribution of *ADC* parameter (a) and *DKI*-derived parameters (b and c) in benign and malignant lesions for 10% the voxels. Reproduced, with permission, from (Mokry et al. 2020).

Table 18. Statistics of the parameters derived by diffusion and diffusion kurtosis fitting model for 10% the voxels

	benign	**malignant**	**difference derived by linear mixed model**	***p****
	median [min, max]	**median [min, max]**	**average difference between malignant and benign [95%CI]**	
ADC [μm²/ms]	1.38 [0.41, 2.81]	0.82 [0.51, 1.68]	-0.56 [-0.93, -0.18]	0.0053
D_{app} [μm²/ms]	1.80 [0.52, 3.39]	1.07 [0.66, 2.24]	-0.62 [-1.02, -0.21]	0.0048
K_{app}	0.62 [0.40, 1.55]	0.86 [0.57, 1.28]	0.21 [0.073, 0.34]	0.0043

5.4.4 Mixed Logistic Model – 10% of the Voxels

For the mixed logistic model with single predictor, the highest ROC AUC of 0.85 (CI95% 0.75–0.95) was observed for K_{app}, whereas the AUC for *ADC* was 0.80 (CI95% 0.70–0.91) and for D_{app} 0.80 (CI95% 0.69–0.91) but the differences where not statistically significant ($0.06<p<0.08$). For the cut-off points at the sensitivity 100%, the specificity of *ADC* and D_{app} was 29% (CI95% 18–42) and for K_{app} was 32% (CI95% 21–45). The addition of *ADC* or D_{app} as a second predictor to K_{app} did not result in better performance. The ROC curves are presented in Figure 33 .

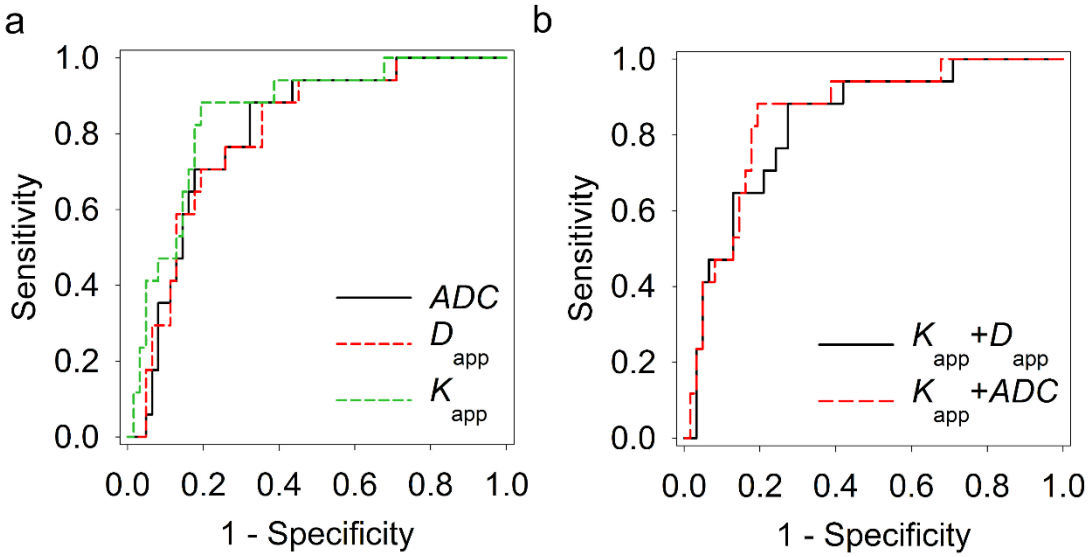

Figure 33. ROC curves for 10% of the voxels (a – single predictor model, b – two predictors model). Reproduced, with permission, from (Mokry et al. 2020).

Table 19. Summary of diagnostic performance of mixed logistic models with diffusion and kurtosis coefficient as predictors in differentiating malignant from benign ovarian lesions for 10% the voxels.

MLM parameters	**AUC**	***p****	**Sensitivity 100% (CI95% 80-100)**	**Sensitivity 94% (CI95% 71-100)**	**Sensitivity 88% (CI95% 64-99)**
ADC	0.80 (CI95% 0.70–0.91)	0.06	29% (CI95% 18–42)	56% (CI95% 43–69)	68% (CI95% 55–79)
D_{app}	0.80 (CI95% 0.69–0.91)	0.08	29% (CI95% 18–42)	55% (CI95% 42–68)	65% (CI95% 51–76)
K_{app}	0.85 (CI95% 0.75–0.95)	–	32% (CI95% 21–45)	61% (CI95% 48–73)	81% (CI95% 69–90)
K_{app}+D_{app}	0.83 (CI95% 0.73–0.94)	0.15	29% (CI95% 18–42)	58% (CI95% 45–70)	73% (CI95% 60–83)
K_{app}+*ADC*	0.85 (CI95% 0.75–0.95)	0	32% (CI95% 21–45)	61% (CI95% 48–73)	81% (CI95% 69–90)

*p-value for AUCs comparison to AUC for K_{app}

5.4.5 Reduced Cohort of Patients

This subsection is devoted to the results obtained for the reduced cohort of patients comprising 49 lesions. For the selected DWI- and DKI-derived parameters under investigation, the average differences between the malignant and benign lesions were more pronounced in the reduced cohort when comparing with the full cohort of patients, which is in line with expectations. This observation is valid for both analyses based on the selected 1% and 10% the voxels in the ROI (Table 20 and Table 22).

Table 20. Statistics of the parameters derived by diffusion and diffusion kurtosis fitting model for the reduced cohort of patients for 1% the voxels.

	benign	**malignant**	**difference derived by linear mixed model**	***p****
	median [min, max]	**median [min, max]**	**average difference between malignant and benign [95%CI]**	
ADC [$\mu m^2/ms$]	1.35 [0.35, 2.63]	0.74 [0.52, 1.44]	-0.62 [-1.00, -0.24]	0.0040
D_{app} [$\mu m^2/ms$]	1.74 [0.44, 3.34]	0.98 [0.63, 2.12]	-0.78 [-1.28, -0.29]	0.0050
K_{app}	0.61 [0.44, 1.19]	1.01 [0.69, 1.30]	0.32 [0.18, 0.46]	0.0004

The results of the ROC analysis for the reduced number of patients for the main analysis based on the selected 1% the voxels in the ROI is summarized in Table 21.

Table 21. Summary of diagnostic performance of mixed logistic models with diffusion and kurtosis coefficient as predictors in differentiating malignant from benign ovarian lesions for 1% the voxels in the reduced cohort of patients.

GLMMIX paramters	**AUC**	***p****	**Sensitivity 100% (CI95% 80-100)**	**Sensitivity 94% (CI95% 71-100)**	**Sensitivity 88% (CI95% 64-99)**
ADC	0.82 (CI95% 0.69–0.94)	0.13	41% (CI95% 24-59)	69% (CI95% 50-84)	78% (CI95% 60-91)
D_{app}	0.82 (CI95% 0.69–0.94)	0.15	31% (CI95% 16-50)	69% (CI95% 50-84)	72% (CI95% 53-86)
K_{app}	0.89 (CI95% 0.80–0.98)	–	59% (CI95% 41-76)	78% (CI95% 60-91)	78% (CI95% 60-91)
K_{app}+D_{app}	0.89 (CI95% 0.80–0.98)	0.48	59% (CI95% 41-76)	78% (CI95% 60-91)	81% (CI95% 64-93)
K_{app}+*ADC*	0.89 (CI95% 0.80–0.98)	0	59% (CI95% 41-76)	78% (CI95% 60-91)	78% (CI95% 60-91)

*p-value for AUCs comparison to AUC for K_{app}

Although for all mixed logistic models with single predictor, the increase in AUC can be observed in comparison to the full cohort, resulting in the AUC of 0.82 (CI95% 0.69–0.94) for *ADC* and D_{app} and AUC of 0.89 (CI95% 0.80–0.98) for K_{app}. However, the differences in AUC between K_{app} and *ADC* or K_{app} and D_{app} are not statistically significant. Aiming again for 100% sensitivity, the specificity of 41% (CI95% 24-59) was observed for *ADC*, 31% (CI95% 16-50) for D_{app} and 59% (CI95% 41-76) for K_{app}. The increase in specificity for 100% sensitivity in the reduced cohort in comparison to full cohort was more relevant for *ADC* and D_{app} than for K_{app}. No improvement in specificity at the cut-off point for sensitivity 100% was observed after combining K_{app} with *ADC* or D_{app} in GLMM models with two predictors.

Table 22. Statistics of the parameters derived by diffusion and diffusion kurtosis fitting model for the reduced cohort of patients for 10% the voxels.

	benign	**malignant**	**difference derived by linear mixed model**	***p****
	median [min, max]	**median [min, max]**	**average difference between malignant and benign [95%CI]**	
ADC [$\mu m^2/ms$]	1.66 [0.41, 2.81]	0.82 [0.51, 1.68]	-0.77 [-1.21, -0.33]	0.0024
D_{app} [$\mu m^2/ms$]	2.18 [0.52, 3.39]	1.07 [0.66, 2.24]	-0.83 [-1.31, -0.35]	0.0028
K_{app}	0.58 [0.40, 1.24]	0.86 [0.57, 1.28]	0.26 [0.12, 0.40]	0.0019

Table 23 shows the results of ROC analysis for 10% the voxels in the ROI. It can be observed that in the reduced patients group the AUC of 0.88 (CI95% 0.78–0.98) for K_{app} was still significantly higher than AUC of 0.81 (CI95% 0.68–0.93, $p = 0.053$) for *ADC*, but the difference between the AUC for D_{app} which was 0.82 (CI95% 0.70–0.94) was not statistically significant ($p = 0.14$). However, for the reduced cohort, all three parameters, K_{app}, *ADC* and D_{app}, presented the same specificity of 47% (CI95% 29–65) at the cut–off point for sensitivity 100%. No improvement in AUC was observed after adding the *ADC* or D_{app} as a second predictor to K_{app} in GLMM model ($p = 0.24$ and $p = 0.10$).

Table 23. Summary of diagnostic performance of mixed logistic models with diffusion and kurtosis coefficient as predictors in differentiating malignant from benign ovarian lesions for 10% the voxels in the reduced cohort, after excluding patients with endometriomas, teratomas and follicular cysts.

MLM parameters	**AUC**	***p****	**Sensitivity 100% (CI95% 80–100)**	**Sensitivity 94% (CI95% 71–100)**	**Sensitivity 88% (CI95% 64–99)**
ADC	0.81 (CI95% 0.68–0.93)	0.05	47% (CI95% 29–65)	72% (CI95% 53–86)	75% (CI95% 57–89)
D_{app}	0.82 (CI95% 0.70–0.94)	0.14	47% (CI95% 29–65)	69% (CI95% 50–84)	75% (CI95% 57–89)
K_{app}	0.88 (CI95% 0.78–0.98)	–	47% (CI95% 29–65)	72% (CI95% 53–86)	84% (CI95% 67–95)
K_{app}+D_{app}	0.86 (CI95% 0.75–0.97)	0.10	38% (CI95% 21–56)	72% (CI95% 53–86)	81% (CI95% 64–93)
K_{app}+*ADC*	0.86 (CI95% 0.76–0.97)	0.24	50% (CI95% 32–68)	75% (CI95% 57–89)	81% (CI95% 64–93)

*p-value for AUCs comparison to AUC for K_{app}

6 Discussion

6.1 Breast Phantom

This study shows the potential application of the DWI phantom, dedicated for a breast coil, for assessing the homogeneity of the *ADC* measurements. The proposed phantom offers large-volume imaging and enables simultaneous measurements on both sides of the breast coil. Thanks to the automatization of the segmentation process, various regions depicted on the cross-sectional images can be easily compared. Furthermore, the built-in thermometer enables simple assessment of the temperature of the liquid solution filling the phantom. Therefore, the measured *ADC* value can be corrected to the reference value at 20°C, which is essential for comparison purposes between different measurement days. Moreover, the implemented design solution enables an adjustment of the spacing between the two parts of the phantom to the size of a breast coil. Therefore the phantom can be used in the various systems.

The choice of the PVP water solution as a base for the DWI breast phantom was dictated by its favorable chemical and physical characteristics (Wagner et al. 2017). Firstly, the desired degree of diffusivity can be achieved by changing the concentration of PVP in the water. Secondly, the PVP water solution shows a mono-exponential signal decay with increasing *b*-value, with *ADC* independent of the diffusion time (Pierpaoli et al. 2009). There are various advanced phantoms, composed of multiple compartments filled with the PVP water solutions of different degree of diffusivity. Whereas some of them require an ice-water bath to achieve the reference temperature of 0°C (Boss et al. 2014), others do not use the temperature correction (Keenan et al. 2016b). The main disadvantage of cooling down the PVP solution to 0°C is a decreased range of *ADC* values in comparison to the body temperature, for which the aqueous solutions of PVP span full physiologic range (Keenan et al. 2018). The chosen 30% PVP-K30 concentration results in *ADC* of approximately 0.84 mm^2/s at 20°C (Wagner et al. 2017), which is in the range of the reported mean *ADC* values for the malignant breast lesions (Baltzer et al. 2019).

The proposed phantom allows for addressing many aspects of quality assurance in breast DWI which were discussed in detail in this dissertation. Regular measurements with the phantom may reveal the potential abnormalities during the normal exploitation of the MRI scanner. Generally, in almost all the analyzed sequences, the relative variation was higher in the right part of the phantom, like also the overall *ADC* was higher. In contrast, the opposite rule was observed for both multi-shot segmented sequences with bipolar gradients, with and

without parallel imaging ($RESOLVE_2$ and $RESOLVE_4$), where the left side of the phantom showed higher *CV* and *ADC* than the right part. The spatial variability of *ADC*, analyzed with the use of the segmented ROIs in the phantom revealed the range of disparities reflecting the value of the overall *CV*. Moreover, the occurrence of the regions with the highest and the lowest *ADC* value may be more or less associated with the chosen parameters and the type of the sequence. Therefore, one of the possible applications of the phantom in the future might be the correction of the values obtained for a patient, according to the location of the lesion and the choice of the parameters in the applied sequence. The assessment of the reproducibility of *ADC* over a longer period of time would be especially important for the high-risk patients who have undergone multiple MRI examinations, sometimes on the various scanners.

In the repeated measurements over 5-days period, *CV* for the whole phantom showed comparable values between the measurements of the same variant of the sequence. Among multi-shot segmented EPI (RESOLVE) sequences, those with monopolar diffusion gradients were more stable than the sequences with bipolar gradients. At the same time, the parallel imaging acquisition does not strongly affect the general stability of ADC measurements. Among single-shot EPI sequences with parallel imaging acquisition, the variants with bipolar diffusion gradients also showed higher relative variation than analogical monopolar sequences. However, the difference for sequences without parallel imaging was very small. The higher variation of *ADC* for the bipolar gradient sequence, in comparison to monopolar sequence, may result from the use of the additional refocusing pulse, which makes bipolar gradients more susceptible to flip angle imperfections and B1 magnetic field inhomogeneities (Finsterbusch 2009). An inconsistency in the 90° excitation pulse and a 180° refocusing pulses, which results in misshaped slice profile already in the standard spin-echo EPI (Schmiedeskamp et al. 2012), may be the possible cause of the observed intensified inhomogeneity of *ADC*. Additionally, there may be deviations of the applied gradient shapes from the intended ones due to imperfections of the gradient system. Further investigation of the gradient impulse response function would provide clarification in this regard (Wilm et al. 2015).

To summarize, in this work, the reproducibility of *ADC* in the measurements repeated during the same day was analyzed. A good agreement between the first and the second acquisition could be observed for two repeated multi-shot segmented EPI sequences. However, the second acquisition was conducted nearly at the end of the DWI protocol. Therefore, the rising temperature might be the cause of fluctuations between two measurements from the different time points. For WIP sequences from the second round of the measurements, the values obtained in the repeated measurement gave almost identical results. In this case the second acquisition was conducted directly after the first one.

This study has certain limitations. First of all, the study is based on a relatively low number of measurements, which influences the accuracy of estimation of the parameters. Another

drawback is the used temperature correction method, taking the temperature at the beginning of the measurements. In case of the long-lasting protocols, consisting of many sequences, the temperature of PVP-solution may rise, therefore for sequences acquired at the later point of time the temperature adjustment might be too low and the obtained *ADC* values may be inflated. In such a case the correction assuming linear temperature rise, taking into account the acquisition time of each sequence, could mitigate this problem. Moreover, in some cases the additional sequences were applied or the acquisition was repeated due to the technical problems. Therefore, the time-point of the final acquisition, counted from the beginning of the measurement, was not always the same for the analogous sequences.

6.2 Breast Lesions

The aim of this study was to evaluate the diagnostic ability of various methods with different diffusion-kurtosis-based fitting approaches accounting for residual fat-related signal in characterization of breast lesions. The motivation behind this work was the observation that an overestimation of kurtosis values, due to the elevated background signal level, can be diminished by applying an adjusted correction factor (Bickelhaupt et al. 2018; Jensen and Helpern 2010; Jensen et al. 2005). In this work, three methods aiming to mitigate the overestimation of the kurtosis values caused by the fat-related elevated background level were proposed and examined. The two proposed methods (Method3 and Method4) account mainly for the possible contamination due to the chemical shift, whereas the third one (Method5) takes into account the partial volume effect. Method4 used similar phenomenological extension as proposed by Bickelhaupt et al. (2018), where the approach proposed by Jensen et al. (2005) was extended in the context of a radiomics model. Another approach incorporating a noise correction factor, which is also very similar to the one proposed by (Jensen et al. 2005) was published by Iima et al. (2015). However, this approach was used to reduce the contamination with background noise in the signal, but it did not address the corruption with the remaining fat signal.

The relationship between the values of the coefficients obtained by different fitting approaches used in this study was in line with expectations. The diffusion coefficient derived by standard diffusion kurtosis fitting was higher than the coefficient derived by mono-exponential function, which is due to the compensation of the slower signal decay with higher *b*-values with inclusion of kurtosis coefficient. At the same time, the modified diffusion kurtosis fitting approaches delivered lower values of kurtosis than the standard diffusion kurtosis fitting, because the artificial elevation of the signal at high *b*-values was counteracted by additional correction parameter. Nevertheless, authors of several studies (Nogueira et al. 2014; Palm et al. 2019; Sun et al. 2015) examining DWI and DKI fitting in breast have reported higher minimal *ADC* values in benign and malignant lesions than those observed in this work. This fact might be attributed to the cases of an image that has a poor signal-to-

noise ratio, and exhibits high contamination with residual fat signal. Baron et al. (2010) reported *ADC* values measured in adipose tissue smaller by factor of 10 than *ADC* measured in fibroglandular tissue using SPAIR for fat signal suppression. On the contrary, looking at the mean values of *ADC*, the results are in agreement with the findings of the meta-analysis by Baxter et al. (2019). Regarding the values of diffusion coefficients derived by standard diffusion kurtosis fitting (Method2), the results are consistent with those reported in other studies (Christou et al. 2017; Nogueira et al. 2014; Palm et al. 2019; Sun et al. 2015; Wu et al. 2014; Zhou et al. 2019), whereas values of kurtosis coefficients, in both malignant and benign lesions, are higher. It has to be highlighted that the application of the fat correction factor in Method3** results in lower kurtosis coefficients than in Method2 which are in line with the literature after all. In majority of these studies more *b*-values were involved, and higher maximum *b*-value was used. This work involved an abbreviated DWI protocol, therefore the range of the used *b*-values may not be optimal for DKI evaluation (Chuhutin et al. 2017). Nevertheless, the primary objective was to create a protocol that enables its utilization in the clinical routine. Palm et al. (2019) used a similar number and range of *b*-values and despite of this observed lower kurtosis coefficients. In this case the differences may be attributed to the higher field strength of 3T scanner leading to higher SNR, and selection of only one slice representing the lesion.

In terms of the ROC analysis' outcomes for the entire study population, Method3 and Method4 demonstrated the highest AUC values. For the sensitivity at 95%, the highest specificity was observed with Method4, which reduces the number of indications for biopsy in patients with benign lesions by half. In the individual analyses by the study site, for the sensitivity at 95%, 6 out of 10 patients with benign lesions can be correctly diagnosed with the Method4 in Group A, whereas in Group B it was 5 out of 10 patients with benign lesion. Regarding Method3, the two cohorts exhibit varying outcomes. The inclusion of an extra parameter *a* in Method3, which regulates the level of contamination by fat signal, yielded better results in AUC with increasing *a* value in Group A in comparison to the standard approaches. In contrast, in Group B there was a high degree of similarity in the AUC outcomes. Therefore the usefulness of Method3 is compromised due to the necessity of choosing an appropriate additional parameter. The stratified analysis, in which the patients were categorized by the ratio of the signal intensity in the lesion and adipose tissue area at high *b*-value image, indicated that varying results were achieved between the two groups. In Group A the outcomes suggest that the impaired diagnosis of poorly visible lesions may be indeed caused by the contamination of the signal with residual fat signal, because the effect of the proposed correction factor becomes more significant as the relative background level increases. Group B did not experience the expected benefits from implementation of modified fitting approaches. However, what is true for the entire patient population in this study is the observation that the approach (Method5) with fractionated fat contribution, in which an additional parameter *f* was introduced, showed not only no improvement in AUC, but also resulted in the adverse effect.

This outcome suggests that for the studied population of patients a more significant source of the contamination with the residual fat signal may be chemical shift rather than partial volume effect. Nevertheless, considering the increased intricacy involved with fractionated fat contribution methods, Method4 appears to be more favorable option.

The results of the data analysis suggest that there are noticeable differences between outcomes obtained in Group A and Group B, where DWI data were acquired using MR scanners from different vendors. Despite setting up both DWI sequences as similar as possible, the ultimate parameters were not identical due to differences in technical solutions utilized by the two vendors. Thus, the use of segmented EPI (RESOLVE) or parallel imaging operating on the *k*-space data (GRAPPA) in Group B, as opposed to single-shot EPI and parallel imaging with the reconstruction in the image domain (SENSE) or additional post-processing techniques in Group A, may impact the efficiency of fat suppression. This confirms the necessity for standardization and stresses the crucial role of quality assurance in DWI. A more extensive investigation of the differences in MR sequence specifics and their potential influence on the background signal level and DKI performance may be high of interest.

The application of the original correction factor proposed by Jensen et al. (2005) was possible only in patients from Group B. The AUC values obtained using the original approach with correction factor accounting for noise level were comparable with those obtained with Method4. In Group A, as a result of the post-processing procedure being a part of parallel imaging, the signal outside the patient was set to zero. Especially in this group the comparison between the original method and its phenomenological extension would be the most interesting. Iima et al. (2015) proposed another noise correction factor and observed also lower kurtosis values than these presented here for Method4' with correction factor accounting for noise. However, in the mentioned study, a 3T scanner and broader range of *b*-values were used.

It has to be highlighted that this study is limited by a restricted number of patients, especially in the stratified analysis by lesion visibility at high *b*-value images, where statistical significance testing is highly affected by the small sample size. Another drawback is the lack of validation of the constructed logistic regression models on the independent data sets. It must be pointed out that the obtained AUCs may be too optimistic due to the fitting the models and then testing them on the same data-set. To make a well-established statement, further evaluation is needed. Finally, the interpretation of the signal in the segmented fatty tissue area as the general background signal level may me not completely justified. By assuming that contamination comes from artifacts and partial volume effect, the assigned level of the contamination may be in some cases too high. The shortcoming of the proposed methods accounting for residual fat signal is a possible overcorrection in patients with relatively high signal in the fatty area ROI in comparison to the signal in the lesion. The undesirable effect of very low kurtosis values may lead to false-negative results. All in all, for the preferred

method with the fat correction term, that is Method4, no adverse effects in the overall performance were observed in comparison to the performance of the standard diffusion kurtosis equation in the analyzed cohort.

6.3 Ovarian Lesions

An accurate classification of adnexal masses may be challenging, because the benign tumor incidence rate is much higher than the malignant ones. In patients with equivocal radiological finding surgical removal of adnexal masses with histologic evaluation is required as clarification. As a result, many women with clinically inconsequential benign ovarian lesions, which could be conservatively treated, underwent unnecessary oophorectomy (Stein et al. 2021).

The primary sequence in the standard MRI protocol for characterization of sonographically indeterminate adnexal lesions is the T_1-weighted, and T_2-weighted sequence (Spencer et al. 2010). If the suspicion of presence of neoplasm in solid part of the lesion cannot be dispelled with morphological MRI images, the further sequence of choice is gadolinium contrast-enhanced sequence standalone or in conjunction with diffusion-weighted MRI, whereas DWI as a standalone problem-solving sequence is recommended only in case of lesions with low T_2 (Forstner et al. 2017). The quantitative analysis based on the *ADC* values, derived by standard mono-exponential fitting method, may be challenging due to the fact that some benign ovarian lesions present low *ADC* values which is misleading when accepting the principle that diffusion restrictions are an indicator for malignancy (Agostinho et al. 2019). Furthermore, the results of the meta-analysis by Kim et al. (2016) suggest that the overlap in *ADC* values among benign and malignant lesions makes this parameter an inefficient as a standalone way for characterization of ovarian masses. However, the potential role of DKI in this application has been studied only in a very limited way. Therefore the aim of this study was to evaluate the ability of DKI in characterization of sonographically ambiguous ovarian lesions.

The number of studies evaluating the role of DKI in differentiation of adnexal masses is very limited to date. Li et al. (2017) investigated inter alia malignant epithelial ovarian tumors and reported values of DKI and DWI derived parameters which are in agreement with values of malignant lesions observed in this study. Further, a study by Yue et al. (2019) in a control group with normal endometrium showed the values similar to the ones reported in benign lesions here. However, to date no large study has compared explicitly the diagnostic performance in characterization of various representative types of ovarian lesions.

In this study, the main analysis was based on the selected 1% of the voxels in the ROI, assuming that these represent the regions with the highest diffusion restrictions. As expected, K_{app} was higher in malignant lesions, whereas D_{app} was lower in benign lesions. D_{app} exhibit-

ed higher values than *ADC* in general, which is in line with theory of the correction due to curvature of the signal decay by non-Gaussian diffusion in biological tissue (Jensen and Helpern 2010). The ROC analysis showed, at the threshold at 100% sensitivity, that every second patient with benign lesion could be correctly diagnosed by K_{app} value, whereas by *ADC* it was every fourth patient and by D_{app} every fifth patient with benign lesion. Using K_{app} as a differentiating parameter, the number of the extensive surgical procedures in the analyzed population with benign lesions could be potentially reduced by the half when comparing with diagnosis based on *ADC* value. The analogous additional analysis, when 10% of the voxels were used, shows much smaller specificity for K_{app}, higher for D_{app} and similar for *ADC* than analysis for 1% of the voxels. All in all, the specificity for all these three parameters, that is K_{app}, D_{app} and *ADC*, was comparable with each other in the analysis based on 10% of the voxels. Moreover, although the AUC for the K_{app} reached a higher value than AUC for *ADC* or D_{app}, the differences were not statistically significant (with the *p*-value just over the predetermined threshold). In the case of the mixed logistic models with two predictors, the results of the analysis based on 1% of the voxels selected within the ROI outperformed these obtained for 10% voxels.

It is worth mentioning that many of the analyzed lesions were solid-cystic ovarian neoplasm with the very large cystic component. Therefore, the approach of selecting only 1% of the voxels was applied instead of an analysis of the mean in the whole segmented ROI. It was dictated by the desire to extract the essential information from the most suspicious regions. In the case of lesions primarily composed of cystic component and only small solid part, taking 10% of the voxels in the ROI would result in an elevated *ADC* value approaching *ADC* of free water, masking the contribution from the area of low *ADC* due to diffusion restriction and potential malignancy. Therefore, analysis of only 1% of the voxels with the highest signal intensity allows better selection of the regions with diffusion restrictions and true low *ADC*. On the other hand, the high signal intensity on the high *b*-value image is not always limited to diffusion restrictions. The co-occurrence of hemorrhage and fat components (Duarte et al. 2018) may also be manifested by strong signal intensity on high *b*-values and low *ADC* value which increases the number of false positive findings. Therefore the applied method of voxel selection inside the ROIs may raise some concerns. One hand, the proposed method is characterized by its simplicity and as an automated process guarantees the repeatability of the values of calculated quantitative parameters. On the other hand, selecting a fixed percentage of voxels within the ROI might not be optimal for each lesion. Utilizing only 1% of the voxels within the ROI resulted in notably better outcome of K_{app} parameter when compared to utilizing 10% of the voxels, what can suggest that more informative voxels were chosen for the analysis. Therefore, additional studies for establishing the most appropriate method for selecting voxels in heterogenous ovarian masses are needed. Moreover, the segmentation was limited to only one slice displaying the highest diffusion restrictions in the lesion. The choice of only one slice was dictated by too time-consuming

procedure of manual 3D segmentation, especially in the lesions of big sizes, which might be difficult to incorporate in the clinical routine.

As already mentioned in the previous chapters, the issue of frequent misdiagnosis of certain histopathological types of benign lesions using DWI, which can exhibit unexpectedly low *ADC* values, was addressed in several review studies (Agostinho et al. 2019; Duarte et al. 2018; Kim et al. 2016). It was suggested that in these particular types of masses the diagnosis of benignity can be established by relying on standard morphological MRI sequences. Therefore the additional subanalysis was conducted, using the reduced cohort, after excluding the cases that are frequently misdiagnosed using DWI, like it was described in Section 4.4. The ROC analysis, when considering selected 1% of the voxels, showed improvement in specificity at the sensitivity at 100% for *ADC* and D_{app}, what is consistent with expectations. The performance of K_{app} was also satisfactory. K_{app} showed still the highest specificity at 100% sensitivity, rendering the correct diagnosis of 6 out of 10 patients possible, whereas for D_{app} it was 3 out of 10 and for *ADC* 4 out of 10. All three mentioned coefficients presented the same specificity for 10% voxels analysis.

It has to be highlighted that among the limitations of this study is the small number of patients, especially those with malignant lesions. In consequence, due to the limited amount of data, the models were built and tested on the same data-set which is likely to pose a risk of overfitting. A larger study cohort is crucial for improving the precision of the analysis and ultimately leading to more informed conclusions.

7 Summary

This thesis sets out to investigate the usefulness of diffusion imaging and diffusion kurtosis imaging for characterization of suspicious breast and ovarian lesions. The work was divided into three parts. To answer the research questions, the experiments with the phantom were conducted, and the analysis of the clinical data from retrospective and prospective study was done.

The first part of this thesis was devoted to the experiments with the phantom designed for the breast coil. The aim was to assess the repeatability and reproducibility of quantitative measurements of apparent diffusion coefficient, which is the most commonly used quantitative parameter in clinical diffusion imaging of breast. The ability to control the spatial and temporal uniformity of apparent diffusion coefficient was demonstrated with the semi-automated quality control procedure using the self-written MATLAB script. The interesting feature of the breast phantom is the built-in thermometer which enables the temperature correction of apparent diffusion coefficient values. The readout-segmented and single-shot echo-planar imaging sequences with various setups of diffusion sensitizing gradient and parallel imaging acceleration factor were used. It was shown that this simple isotropic phantom can be used to monitor the variability between left and right side of the breast coil and to detect the differences in measurements with various protocol setup parameters. Among the readout-segmented echo-planar sequences, the highest spatial nonuniformity was found for bipolar gradient sequences, with the variability more prominent in the left side of the coil. Similarly, the bipolar single-shot echo-planar sequences showed higher spatial nonuniformity than the monopolar one, however the bigger variability was observed in the right part of the coil. Moreover, the spatial nonuniformity of apparent diffusion coefficient values varied with the parallel imaging acceleration factor. In summary, depending on the sequence parameters, significant inhomogeneities and right-left differences were observed, which ultimately could not be explained within the scope of this thesis. Therefore, due to the relatively high deviation of *ADC* values, reaching a maximum value of coefficient of variation of 8.69%, further investigation of the origin of these differences seems urgently warranted, particularly regarding discrepancies between the phantoms and patient measurements concerning relaxation times, presence of adipose tissue, and varying diffusion coefficients. As a conclusion, by incorporating the regular quality control procedure into the clinical routine, the variations in measurements can be explored, which could help to ensure the robustness of the measurements of qualitative diffusion parameters. Using this simple breast phantom, the reliability of measured apparent diffusion coefficient values between the coil sides, measurements days, and acquisition among one measurement slot can be estimated. This is especially relevant if

the range of the values of apparent diffusion coefficient for benign and malignant lesion overlap, like it is in the case of breast lesions. The phantoms could potentially serve as suitable tools for selecting appropriate measurement parameters to enable more homogeneous diffusion parameters.

In the second part, the influence of residual fat-related signal on quantitative parameters in diffusion kurtosis imaging of breast was investigated. The not fully suppressed signal from adipose tissue may corrupt the signal in the lesion area and distort the quantitative parameters. Therefore the research aim was to develop various alternative fitting models accounting for possible corruption with signal from fatty tissue. A data-set comprises the diffusion images of suspicious mammography findings taken in two study centers. The proposed modified fitting models performed better than the standard approaches. In the analysis by study site, the incorporation of fat correction terms improved the results in the first cohort of patients. In the second cohort, no improvement with the lack of adverse effect was found. This suggests that the proposed modified evaluation methods may potentially be applied to reduce the negative impact of the contamination of the signal in breast lesion with unsuccessfully suppressed signal from adipose tissue in quantitative diffusion kurtosis imaging.

Finally, the last part of this thesis studies the application of diffusion kurtosis imaging in differentiation between benign and malignant ovarian lesions. Moreover, as the exclusion of malignancy is the main target of this diagnostic imaging procedure, the inconclusive findings need further verification through surgery and histopathological examination for definitive diagnosis. However, in the final diagnosis, the benign tumors outnumber malignant ones. Therefore the improvement of imaging techniques may avoid the unnecessary invasive management of benign adnexal masses. Although many studies showed that diffusion kurtosis imaging has potential for characterization of lesion in various parts of the body, it remained almost unexplored, to date of writing this thesis, for differentiation between benign and malignant ovarian lesions. Therefore the aim of this study was to investigate the reliability of quantitative kurtosis parameters for characterization of sonographically indeterminate ovarian lesions. Receiver operating characteristic analysis showed, that the chosen threshold yielded maximum sensitivity, that is all malignancies could be correctly diagnosed, and specificity giving an accurate classification of every second benign lesion. At the same time, the half of the patients could be accurately classified. This suggests that diffusion kurtosis imaging may have potential for reducing the number of unnecessary oophorectomies.

8 Zusammenfassung

Ziel dieser Arbeit ist es, die Diffusionsbildgebung und die Diffusions-Kurtosis-Bildgebung zur Charakterisierung von verdächtigen Brustläsionen und Ovarialläsionen zu untersuchen. Die Arbeit wurde in drei Teile geteilt. In diesen werden Experimente mit einem Phantom durchgeführt, eine retrospektive Analyse von klinischen Daten erstellt, und eine prospektive Studienanalyse durchgeführt.

Der erste Teil dieser Arbeit ist den Experimenten mit dem für die Brustspule konzipierten Phantom gewidmet. Ziel ist es, die Wiederholbarkeit und Reproduzierbarkeit quantitativer Messungen des scheinbaren Diffusionskoeffizienten zu bewerten, der am häufigsten verwendete quantitative Parameter in der klinischen Diffusionsbildgebung der Brust ist. Die Möglichkeit, die räumliche und zeitliche Homogenität des scheinbaren Diffusionskoeffizienten zu kontrollieren, wird mit einem halbautomatischen Qualitätskontrollverfahren unter Verwendung des selbstgeschriebenen MATLAB-Skripts demonstriert. Die Besonderheit des Brustphantoms ist ein eingebautes Thermometer, mit dem eine Temperaturkorrektur der scheinbaren Diffusionskoeffizienten möglich wird. Hierbei werden Sequenzen mit verschiedenen Einstellungen verwendet. Es wird gezeigt, dass dieses einfache isotrope Phantom verwendet werden kann, um eine Variabilität zwischen linker und rechter Seite der Brustspule und die Unterschiede in den Messungen mit verschiedenen Protokollen zu überwachen. Unter den gemessenen Auslese-segmentierten echoplanaren Diffusionssequenzen zeigen bipolare Gradientensequenzen die höchste räumliche Ungleichmäßigkeit, wobei die Variabilität auf der linken Seite der Spule stärker ausgeprägt ist. In ähnlicher Weise zeigten die bipolaren Single-Shot-Echo-Planar-Sequenzen eine höhere räumliche Ungleichförmigkeit als die monopolare, jedoch wird die größere Variabilität im rechten Teil der Spule beobachtet. Darüber hinaus änderte sich die räumliche Ungleichmäßigkeit der scheinbaren Diffusionskoeffizientenwerte mit dem parallelen Abbildungsbeschleunigungsfaktor. Abschließend, zeigen sich je nach Sequenzparametern deutliche Inhomogenitäten und recht-links-Unterschiede, die letztlich im Rahmen dieser Arbeit nicht erklärt werden konnten. Aufgrund der erheblichen Diskrepanzen im *ADC*-Werte und dem höchsten Variationskoeffizient von 8.67% scheint jedoch eine weitere Untersuchung der Herkunft der Unterschiede dringend geboten, auch hinsichtlich der Unterschiede der Phantome im Vergleich zu Patientenmessungen hinsichtlich der Relaxationszeiten, Präsenz von Fettgewebe und unterschiedlicher Diffusionskoeffizienten. Zusammenfassend lässt sich sagen, dass durch die Einbeziehung des regulären Qualitätskontrollverfahrens in die klinische Routine die Variationen in der Messung untersucht werden können, was dazu beitragen könnte, die Robustheit der Messungen qualitativer Diffusionsparameter sicherzustellen. Unter Verwendung dieses einfachen Brustphantoms kann die Zuverlässigkeit der gemessenen Werte des scheinbaren Diffusionskoeffizienten zwischen den Spu-

lenseiten, den Messtagen und der Datenerfassung innerhalb des Messzeitfensters geschätzt werden. Dies ist besonders relevant, wenn sich die Wertebereiche des scheinbaren Diffusionskoeffizienten für gutartige und bösartige Läsionen überschneidet, wie es im Fall von Brustläsionen der Fall ist.

Im zweiten Teil wurde der Einfluss des Restfettsignals auf quantitative Parameter in der Diffusions-Kurtosis-Bildgebung der Brust untersucht. Das nicht vollständig unterdrückte Signal des Fettgewebes kann das Signal im Bereich von Läsionen verfälschen und die quantitativen Parameter verfälschen. Daher ist das Forschungsziel, verschiedene alternative Anpassungsmodelle zu entwickeln, die eine mögliche Verfälschung mit Signalen aus Fettgewebe berücksichtigen. Ein Datensatz umfasst die in zwei Studienzentren aufgenommenen Diffusionsbilder verdächtiger Mammographiebefunde. Die vorgeschlagenen modifizierten Anpassungsmodelle schneiden besser ab als die Standardansätze. In der Analyse nach Studienort verbesserte die Aufnahme von Fettkorrekturbegriffen die Ergebnisse in der ersten Patientenkohorte. In der zweiten Kohorte wird keine Verbesserung bei fehlender Nebenwirkung festgestellt. Dies deutet darauf hin, dass die vorgeschlagenen modifizierten Bewertungsmethoden möglicherweise angewendet werden können, um die negativen Auswirkungen der Kontamination des Signals in Brustläsionen mit erfolglos unterdrückten Signalen aus Fettgewebe in der quantitativen Diffusions-Kurtosis-Bildgebung zu verringern.

Schließlich untersucht der letzte Teil dieser Arbeit die Anwendung der Diffusions-Kurtosis-Bildgebung zur Differenzierung zwischen gutartigen und bösartigen Ovarialläsionen. Da der Ausschluss einer Malignität das Hauptziel der diagnostischen Bildgebung ist, müssen die nicht eindeutigen Befunde durch eine Operation und eine histopathologische Untersuchung für eine endgültige Diagnose verifiziert werden. Bei der endgültigen Diagnose überwiegen jedoch gutartige Tumoren den bösartigen. Daher kann die Verbesserung der bildgebenden Verfahren die unnötige invasive Behandlung gutartiger Ovarialläsionen vermeiden. Obwohl viele Studien gezeigt haben, dass die Diffusions-Kurtosis-Bildgebung ein vielversprechendes Potenzial zur Charakterisierung von Läsionen in verschiedenen Körperteilen hat, blieb sie bis zum Zeitpunkt der Erstellung dieser Arbeit nahezu unerforscht, um zwischen gutartigen und bösartigen Ovarialläsionen zu unterscheiden. Ziel dieser Studie ist es daher, die Zuverlässigkeit quantitativer Parameter bei der Charakterisierung sonographisch unklarer Ovarialläsionen zu untersuchen. Die Receiver-Operating-Characteristic-Analyse zeigte, dass der gewählte Schwellenwert ermöglichte, dass alle malignen Erkrankungen korrekt diagnostiziert werden können, und gleichzeitig jede zweite gutartige Läsion genau klassifiziert werden kann. Dies zeigt das Potential der Diffusions-Kurtosis-Bildgebung unnötigen invasiven chirurgischen Eingriffen zu reduzieren.

9 References

Agostinho, L., Horta, M., Salvador, J. C. and Cunha, T. M. (2019). **Benign ovarian lesions with restricted diffusion**. Radiol Bras *52*, 106-111, doi: 10.1590/0100-3984.2018.0078.

Alexander, A. L., Tsuruda, J. S. and Parker, D. L. (1997). **Elimination of eddy current artifacts in diffusion-weighted echo-planar images: the use of bipolar gradients**. Magn Reson Med *38*, 1016-1021, doi: 10.1002/mrm.1910380623.

Amornsiripanitch, N., Bickelhaupt, S., Shin, H. J., Dang, M., Rahbar, H., Pinker, K. and Partridge, S. C. (2019). **Diffusion-weighted MRI for Unenhanced Breast Cancer Screening**. Radiology *293*, 504-520, doi: 10.1148/radiol.2019182789.

Auekitrungrueng, R., Tinnangwattana, D., Tantipalakorn, C., Charoenratana, C., Lerthiranwong, T., Wanapirak, C. and Tongsong, T. (2019). **Comparison of the diagnostic accuracy of International Ovarian Tumor Analysis simple rules and the risk of malignancy index to discriminate between benign and malignant adnexal masses**. Int J Gynaecol Obstet *146*, 364-369, doi: 10.1002/ijgo.12891.

Bakker, M. F., de Lange, S. V., Pijnappel, R. M., Mann, R. M., Peeters, P. H. M., Monninkhof, E. M., Emaus, M. J., Loo, C. E., Bisschops, R. H. C., Lobbes, M. B. I., de Jong, M. D. F., Duvivier, K. M., Veltman, J., Karssemeijer, N., de Koning, H. J., van Diest, P. J., Mali, W., van den Bosch, M., Veldhuis, W. B. and van Gils, C. H. (2019). **Supplemental MRI Screening for Women with Extremely Dense Breast Tissue**. N Engl J Med *381*, 2091-2102, doi: 10.1056/NEJMoa1903986.

Baltzer, P., Mann, R. M., Iima, M., Sigmund, E. E., Clauser, P., Gilbert, F. J., Martincich, L., Partridge, S. C., Patterson, A., Pinker, K., Thibault, F., Camps-Herrero, J. and Le Bihan, D. (2019). **Diffusion-weighted imaging of the breast-a consensus and mission statement from the EUSOBI International Breast Diffusion-Weighted Imaging working group**. Eur Radiol, doi: 10.1007/s00330-019-06510-3.

Bammer, R. (2003). **Basic principles of diffusion-weighted imaging**. Eur J Radiol *45*, 169-184, doi: 10.1016/s0720-048x(02)00303-0.

Baron, P., Dorrius, M. D., Kappert, P., Oudkerk, M. and Sijens, P. E. (2010). **Diffusion-weighted imaging of normal fibroglandular breast tissue: influence of**

microperfusion and fat suppression technique on the apparent diffusion coefficient. NMR Biomed *23*, 399-405, doi: 10.1002/nbm.1475.

Baxter, G. C., Graves, M. J., Gilbert, F. J. and Patterson, A. J. (2019). **A Meta-analysis of the Diagnostic Performance of Diffusion MRI for Breast Lesion Characterization**. Radiology *291*, 632-641, doi: 10.1148/radiol.2019182510.

Bernstein, M., King, K. and Zhou, X. (2004). **Handbook of MRI Pulse Sequences**, Elsevier.

Bickelhaupt, S., Jaeger, P. F., Laun, F. B., Lederer, W., Daniel, H., Kuder, T. A., Wuesthof, L., Paech, D., Bonekamp, D., Radbruch, A., Delorme, S., Schlemmer, H. P., Steudle, F. H. and Maier-Hein, K. H. (2018). **Radiomics Based on Adapted Diffusion Kurtosis Imaging Helps to Clarify Most Mammographic Findings Suspicious for Cancer**. Radiology *287*, 761-770, doi: 10.1148/radiol.2017170273.

Bickelhaupt, S., Laun, F. B., Tesdorff, J., Lederer, W., Daniel, H., Stieber, A., Delorme, S. and Schlemmer, H. P. (2016). **Fast and Noninvasive Characterization of Suspicious Lesions Detected at Breast Cancer X-Ray Screening: Capability of Diffusion-weighted MR Imaging with MIPs**. Radiology *278*, 689-697, doi: 10.1148/radiol.2015150425.

Bihan, D. L., Breton, E., Lallemand, D., Aubin, M. L., Vignaud, J. and Laval-Jeantet, M. (1988). **Separation of diffusion and perfusion in intravoxel incoherent motion MR imaging**. Radiology *168*, 497-505, doi: 10.1148/radiology.168.2.3393671.

Blaimer, M., Breuer, F., Mueller, M., Heidemann, R. M., Griswold, M. A. and Jakob, P. M. (2004). **SMASH, SENSE, PILS, GRAPPA: how to choose the optimal method**. Top Magn Reson Imaging *15*, 223-236, doi: 10.1097/01.rmr.0000136558.09801.dd.

Boss, M., Chenevert, T., Waterton, J., Morris, D., Ragheb, H., Jackson, A., deSouza, N., Collins, D., van Beers, B., Garteiser, P., Doblas, S., Persigehl, T., Hedderich, D., Martin, A., Mukherjee, P., Keenan, K., Russek, S., Jackson, E. and Zahlmann, G. (2014). **TU-C-12A-08: Thermally-Stabilized Isotropic Diffusion Phantom for Multisite Assessment of Apparent Diffusion Coefficient Reproducibilty**. Medical Physics *41*, 464-464, doi: 10.1118/1.4889298.

Bray, F., Ferlay, J., Soerjomataram, I., Siegel, R. L., Torre, L. A. and Jemal, A. (2018). **Global cancer statistics 2018: GLOBOCAN estimates of incidence and mortality worldwide for 36 cancers in 185 countries**. CA Cancer J Clin *68*, 394-424, doi: 10.3322/caac.21492.

Bulletins—Gynecology, American College of Obstetricians and Gynecologists' Committee on Practice Bulletins—Gynecology (2016). **Practice Bulletin No. 174: Evaluation and Management of Adnexal Masses**. Obstet Gynecol *128*, e210-e226, doi: 10.1097/aog.0000000000001768.

Burton, A., Maskarinec, G., Perez-Gomez, B., Vachon, C., Miao, H., Lajous, M., López-Ridaura, R., Rice, M., Pereira, A., Garmendia, M. L., Tamimi, R. M., Bertrand, K., Kwong, A., Ursin, G., Lee, E., Qureshi, S. A., Ma, H., Vinnicombe, S., Moss, S., Allen, S., Ndumia, R., Vinayak, S., Teo, S. H., Mariapun, S., Fadzli, F., Peplonska, B., Bukowska, A., Nagata, C., Stone, J., Hopper, J., Giles, G., Ozmen, V., Aribal, M. E., Schüz, J., Van Gils, C. H., Wanders, J. O. P., Sirous, R., Sirous, M., Hipwell, J., Kim, J., Lee, J. W., Dickens, C., Hartman, M., Chia, K. S., Scott, C., Chiarelli, A. M., Linton, L., Pollan, M., Flugelman, A. A., Salem, D., Kamal, R., Boyd, N., Dos-Santos-Silva, I. and McCormack, V. (2017). **Mammographic density and ageing: A collaborative pooled analysis of cross-sectional data from 22 countries worldwide**. PLoS Med *14*, e1002335, doi: 10.1371/journal.pmed.1002335.

Bushong, S. C. and Clarke, G. D. (2015). **Magnetic Resonance Imaging : physical and biological principles**, Elsevier Mosby, St. Louis, Missouri.

Canny, J. (1986). **A computational approach to edge detection**. IEEE Trans Pattern Anal Mach Intell *8*, 679-698.

Choi, J. I., Park, S. B., Han, B. H., Kim, Y. H., Lee, Y. H., Park, H. J. and Lee, E. S. (2016). **Imaging features of complex solid and multicystic ovarian lesions: proposed algorithm for differential diagnosis**. Clin Imaging *40*, 46-56, doi: 10.1016/j.clinimag.2015.06.008.

Christou, A., Ghiatas, A., Priovolos, D., Veliou, K. and Bougias, H. (2017). **Accuracy of diffusion kurtosis imaging in characterization of breast lesions**. Br J Radiol *90*, 20160873, doi: 10.1259/bjr.20160873.

Chuhutin, A., Hansen, B. and Jespersen, S. N. (2017). **Precision and accuracy of diffusion kurtosis estimation and the influence of b-value selection**. NMR Biomed *30*, doi: 10.1002/nbm.3777.

Comstock, C. E., Gatsonis, C., Newstead, G. M., Snyder, B. S., Gareen, I. F., Bergin, J. T., Rahbar, H., Sung, J. S., Jacobs, C., Harvey, J. A., Nicholson, M. H., Ward, R. C., Holt, J., Prather, A., Miller, K. D., Schnall, M. D. and Kuhl, C. K. (2020). **Comparison of Abbreviated Breast MRI vs Digital Breast Tomosynthesis for Breast Cancer Detection Among Women With Dense Breasts Undergoing Screening**. Jama *323*, 746-756, doi: 10.1001/jama.2020.0572.

David G. Kleinbaum, M. K. (2002). **Logistic Regression A Self-Learning Text**, 2nd. edn, Springer-Verlag New York

Dawson, B. and Trapp, R. G. (2004). **Basic & Clinical Biostatistics**, fourth. edn, McGraw-Hill Education

Delfaut, E. M., Beltran, J., Johnson, G., Rousseau, J., Marchandise, X. and Cotten, A. (1999). **Fat suppression in MR imaging: techniques and pitfalls**. Radiographics *19*, 373-382, doi: 10.1148/radiographics.19.2.g99mr03373.

Dietrich, O., Heiland, S. and Sartor, K. (2001). **Noise correction for the exact determination of apparent diffusion coefficients at low SNR**. Magnetic Resonance in Medicine *45*, 448-453, doi: https://doi.org/10.1002/1522-2594(200103)45:3<448::AID-MRM1059>3.0.CO;2-W.

Duarte, A. L., Dias, J. L. and Cunha, T. M. (2018). **Pitfalls of diffusion-weighted imaging of the female pelvis**. Radiol Bras *51*, 37-44, doi: 10.1590/0100-3984.2016.0208.

E. Mark Haacke, R. V., Robert W. Brown, Michael R. Thompson, Y.-C. Norman Cheng (1999). **Magnetic Resonance Imaging: Physical Principles and Sequence Design**, 1st. edn, Wiley

Finsterbusch, J. (2009). **Eddy-current compensated diffusion weighting with a single refocusing RF pulse**. Magn Reson Med *61*, 748-754, doi: 10.1002/mrm.21899.

Forstner, R., Thomassin-Naggara, I., Cunha, T. M., Kinkel, K., Masselli, G., Kubik-Huch, R., Spencer, J. A. and Rockall, A. (2017). **ESUR recommendations for MR imaging of the sonographically indeterminate adnexal mass: an update**. Eur Radiol *27*, 2248-2257, doi: 10.1007/s00330-016-4600-3.

Griswold, M. A., Jakob, P. M., Heidemann, R. M., Nittka, M., Jellus, V., Wang, J., Kiefer, B. and Haase, A. (2002). **Generalized autocalibrating partially parallel acquisitions (GRAPPA)**. Magn Reson Med *47*, 1202-1210, doi: 10.1002/mrm.10171.

Gudbjartsson, H. and Patz, S. (1995). **The Rician distribution of noisy MRI data**. Magn Reson Med *34*, 910-914, doi: 10.1002/mrm.1910340618.

Hedayati, V., Tunariu, N., Collins, D. and Koh, D.-M. (2014). **Diffusion-Weighted MR Imaging in Oncology**. Current Radiology Reports *2*, 44, doi: 10.1007/s40134-014-0044-1.

Iima, M. and Le Bihan, D. (2016). **Clinical Intravoxel Incoherent Motion and Diffusion MR Imaging: Past, Present, and Future**. Radiology *278*, 13-32, doi: 10.1148/radiol.2015150244.

Iima, M., Yano, K., Kataoka, M., Umehana, M., Murata, K., Kanao, S., Togashi, K. and Le Bihan, D. (2015). **Quantitative non-Gaussian diffusion and intravoxel incoherent motion magnetic resonance imaging: differentiation of malignant and benign breast lesions**. Invest Radiol *50*, 205-211, doi: 10.1097/rli.0000000000000094.

Jensen, J. H. and Helpern, J. A. (2010). **MRI quantification of non-Gaussian water diffusion by kurtosis analysis**. NMR Biomed *23*, 698-710, doi: 10.1002/nbm.1518.

Jensen, J. H., Helpern, J. A., Ramani, A., Lu, H. and Kaczynski, K. (2005). **Diffusional kurtosis imaging: the quantification of non-gaussian water diffusion by means of magnetic resonance imaging**. Magn Reson Med *53*, 1432-1440, doi: 10.1002/mrm.20508.

Keenan, K. E., Ainslie, M., Barker, A. J., Boss, M. A., Cecil, K. M., Charles, C., Chenevert, T. L., Clarke, L., Evelhoch, J. L., Finn, P., Gembris, D., Gunter, J. L., Hill, D. L. G., Jack, C. R., Jr., Jackson, E. F., Liu, G., Russek, S. E., Sharma, S. D., Steckner, M., Stupic, K. F., Trzasko, J. D., Yuan, C. and Zheng, J. (2018). **Quantitative magnetic resonance imaging phantoms: A review and the need for a system phantom**. Magn Reson Med *79*, 48-61, doi: 10.1002/mrm.26982.

Keenan, K. E., Peskin, A. P., Wilmes, L. J., Aliu, S. O., Jones, E. F., Li, W., Kornak, J., Newitt, D. C. and Hylton, N. M. (2016a). **Variability and bias assessment in breast ADC measurement across multiple systems**. J Magn Reson Imaging *44*, 846-855, doi: 10.1002/jmri.25237.

Keenan, K. E., Wilmes, L. J., Aliu, S. O., Newitt, D. C., Jones, E. F., Boss, M. A., Stupic, K. F., Russek, S. E. and Hylton, N. M. (2016b). **Design of a breast phantom for quantitative MRI**. J Magn Reson Imaging *44*, 610-619, doi: 10.1002/jmri.25214.

Kim, H. J., Lee, S. Y., Shin, Y. R., Park, C. S. and Kim, K. (2016). **The Value of Diffusion-Weighted Imaging in the Differential Diagnosis of Ovarian Lesions: A Meta-Analysis**. PLoS One *11*, e0149465, doi: 10.1371/journal.pone.0149465.

Kuder, T. A. (2014) **Diffusion Pore Imaging by Nuclear Magnetic Resonance**. Heidelberg, Univ., Diss., 2014.

Le Bihan, D., Poupon, C., Amadon, A. and Lethimonnier, F. (2006). **Artifacts and pitfalls in diffusion MRI**. J Magn Reson Imaging *24*, 478-488, doi: 10.1002/jmri.20683.

Li, H. M., Zhao, S. H., Qiang, J. W., Zhang, G. F., Feng, F., Ma, F. H., Li, Y. A. and Gu, W. Y. (2017). **Diffusion kurtosis imaging for differentiating borderline from malignant epithelial ovarian tumors: A correlation with Ki-67 expression**. J Magn Reson Imaging *46*, 1499-1506, doi: 10.1002/jmri.25696.

Lu, H., Jensen, J. H., Ramani, A. and Helpern, J. A. (2006). **Three-dimensional characterization of non-gaussian water diffusion in humans using diffusion kurtosis imaging**. NMR Biomed *19*, 236-247, doi: 10.1002/nbm.1020.

Malayeri, A. A., El Khouli, R. H., Zaheer, A., Jacobs, M. A., Corona-Villalobos, C. P., Kamel, I. R. and Macura, K. J. (2011). **Principles and applications of diffusion-weighted imaging in cancer detection, staging, and treatment follow-up**. Radiographics *31*, 1773-1791, doi: 10.1148/rg.316115515.

Mammographie, K. (2019). **Jahresbericht Evaluation 2017. Deutsches Mammographie-Screening-Programm.** (Kooperationsgemeinschaft Mammographie, Berlin).

Mann, R. M., Kuhl, C. K. and Moy, L. (2019). **Contrast-enhanced MRI for breast cancer screening**. J Magn Reson Imaging *50*, 377-390, doi: 10.1002/jmri.26654.

Martí-Bonmatí, L. (2002). **MR Image Acquisition: From 2D to 3D**. In: 3D Image Processing: Techniques and Clinical Applications, eds. Caramella, D. and Bartolozzi, C., Springer Berlin Heidelberg, Berlin, Heidelberg, pp. 21-29.

Messina, C., Bignone, R., Bruno, A., Bruno, A., Bruno, F., Calandri, M., Caruso, D., Coppolino, P., Robertis, R., Gentili, F., Grazzini, I., Natella, R., Scalise, P., Barile, A., Grassi, R. and Albano, D. (2020). **Diffusion-Weighted Imaging in Oncology: An Update**. Cancers (Basel) *12*, doi: 10.3390/cancers12061493.

Mlynarska-Bujny, A., Bickelhaupt, S., Laun, F. B., König, F., Lederer, W., Daniel, H., Ladd, M. E., Schlemmer, H.-P., Delorme, S. and Kuder, T. A. (2020). **Influence of residual fat signal on diffusion kurtosis MRI of suspicious mammography findings**. Scientific Reports *10*, 13286, doi: 10.1038/s41598-020-70154-3.

Mokry, T., Mlynarska-Bujny, A., Kuder, T. A., Hasse, F. C., Hog, R., Wallwiener, M., Dinkic, C., Brucker, J., Sinn, P., Gnirs, R., Kauczor, H.-U., Schlemmer, H.-P., Rom, J. and Bickelhaupt, S. (2020). **Ultra-High-b-Value Kurtosis Imaging for Noninvasive Tissue Characterization of Ovarian Lesions**. Radiology *296*, 358-369, doi: 10.1148/radiol.2020191700.

Mori, S. (2007). **Introduction to Diffusion Tensor Imaging**, 1st. edn, Elsevier Science

Mori, S. and van Zijl, P. C. M. (2002). **Fiber tracking: principles and strategies – a technical review**. NMR in Biomedicine *15*, 468-480, doi: 10.1002/nbm.781.

Murata, N., Gonzalez-Cuyar, L. F., Murata, K., Fligner, C., Dills, R., Hippe, D. and Maravilla, K. R. (2016). **Macrocyclic and Other Non-Group 1 Gadolinium Contrast Agents Deposit Low Levels of Gadolinium in Brain and Bone Tissue: Preliminary Results From 9 Patients With Normal Renal Function**. Invest Radiol *51*, 447-453, doi: 10.1097/rli.0000000000000252.

Nogueira, L., Brandao, S., Matos, E., Nunes, R. G., Loureiro, J., Ramos, I. and Ferreira, H. A. (2014). **Application of the diffusion kurtosis model for the study of breast lesions**. Eur Radiol *24*, 1197-1203, doi: 10.1007/s00330-014-3146-5.

Palm, T., Wenkel, E., Ohlmeyer, S., Janka, R., Uder, M., Weiland, E., Bickelhaupt, S., Ladd, M. E., Zaitsev, M., Hensel, B. and Laun, F. B. (2019). **Diffusion kurtosis imaging does not improve differentiation performance of breast lesions in a short clinical protocol**. Magn Reson Imaging *63*, 205-216, doi: 10.1016/j.mri.2019.08.007.

Partridge S. C., McDonald. E. (2013). **Diffusion weighted magnetic resonance imaging of the breast: protocol optimization, interpretation, and clinical applications**. Magn Reson Imaging Clin N Am 21, 601-624, doi: 10.1016/j.mric.2013.04.007.

Partridge, S. C., Nissan, N., Rahbar, H., Kitsch, A. E. and Sigmund, E. E. (2017). **Diffusion-weighted breast MRI: Clinical applications and emerging techniques**. J Magn Reson Imaging *45*, 337-355, doi: 10.1002/jmri.25479.

Pierpaoli, C., Sarlls, J. E., Nevo, U., Basser, P. J. and Horkay, F. (2009). **Polyvinylpyrrolidone (PVP) water solutions as isotropic phantoms for diffusion MRI studies**.

Porter, D. A. and Heidemann, R. M. (2009). **High resolution diffusion-weighted imaging using readout-segmented echo-planar imaging, parallel imaging and a two-dimensional navigator-based reacquisition**. Magn Reson Med *62*, 468-475, doi: 10.1002/mrm.22024.

Qayyum, A. (2009). **Diffusion-weighted Imaging in the Abdomen and Pelvis: Concepts and Applications**. RadioGraphics *29*, 1797-1810, doi: 10.1148/rg.296095521.

Radbruch, A., Weberling, L. D., Kieslich, P. J., Eidel, O., Burth, S., Kickingereder, P., Heiland, S., Wick, W., Schlemmer, H. P. and Bendszus, M. (2015). **Gadolinium retention in the dentate nucleus and globus pallidus is dependent on the class of contrast agent**. Radiology *275*, 783-791, doi: 10.1148/radiol.2015150337.

Reese, T., Weisskoff, R. and Wedeen, V. (1998). **Diffusion NMR facilitated by a refocused eddy-current EPI pulse sequence**. Proceedings of the 6th Annual Meeting of ISMRM, 663.

Schmiedeskamp, H., Straka, M. and Bammer, R. (2012). **Compensation of slice profile mismatch in combined spin- and gradient-echo echo-planar imaging pulse sequences**. Magn Reson Med *67*, 378-388, doi: 10.1002/mrm.23012.

Sickles, E., D'Orsi CJ, Bassett LW, et al. (2013). **ACR BI-RADS® Mammography**. In: ACR BI-RADS® Atlas, Breast Imaging Reporting and Data System, Reston, VA, American College of Radiology.

Spak, D. A., Plaxco, J. S., Santiago, L., Dryden, M. J. and Dogan, B. E. (2017). **BI-RADS® fifth edition: A summary of changes**. Diagnostic and Interventional Imaging *98*, 179-190, doi: 10.1016/j.diii.2017.01.001.

Spencer, J. A., Forstner, R., Cunha, T. M. and Kinkel, K. (2010). **ESUR guidelines for MR imaging of the sonographically indeterminate adnexal mass: an algorithmic approach**. Eur Radiol *20*, 25-35, doi: 10.1007/s00330-009-1584-2.

Stehling, M. K., Turner, R. and Mansfield, P. (1991). **Echo-planar imaging: magnetic resonance imaging in a fraction of a second**. Science *254*, 43-50, doi: 10.1126/science.1925560.

Stein, E. B., Roseland, M. E., Shampain, K. L., Wasnik, A. P. and Maturen, K. E. (2021). **Contemporary Guidelines for Adnexal Mass Imaging: A 2020 Update**. Abdom Radiol (NY) *46*, 2127-2139, doi: 10.1007/s00261-020-02812-z.

Stieltjes, B., Brunner, R. M., Fritzsche, K. and Laun, F. (2013). **Introduction to Diffusion Imaging**. In: Diffusion Tensor Imaging Introduction and Atlas, 1. edn, Springer-Verlag Berlin Heidelberg, pp. 5-40.

Stout, N. K., Lee, S. J., Schechter, C. B., Kerlikowske, K., Alagoz, O., Berry, D., Buist, D. S., Cevik, M., Chisholm, G., de Koning, H. J., Huang, H., Hubbard, R. A., Miglioretti, D. L., Munsell, M. F., Trentham-Dietz, A., van Ravesteyn, N. T., Tosteson, A. N. and Mandelblatt, J. S. (2014). **Benefits, harms, and costs for breast cancer screening after US implementation of digital mammography**. J Natl Cancer Inst *106*, dju092, doi: 10.1093/jnci/dju092.

Sun, K., Chen, X., Chai, W., Fei, X., Fu, C., Yan, X., Zhan, Y., Chen, K., Shen, K. and Yan, F. (2015). **Breast Cancer: Diffusion Kurtosis MR Imaging-Diagnostic Accuracy and Correlation with Clinical-Pathologic Factors**. Radiology *277*, 46-55, doi: 10.1148/radiol.15141625.

Timmerman, D., Ameye, L., Fischerova, D., Epstein, E., Melis, G. B., Guerriero, S., Van Holsbeke, C., Savelli, L., Fruscio, R., Lissoni, A. A., Testa, A. C., Veldman, J., Vergote, I., Van Huffel, S., Bourne, T. and Valentin, L. (2010). **Simple ultrasound rules to distinguish between benign and malignant adnexal masses before surgery: prospective validation by IOTA group**. Bmj *341*, c6839, doi: 10.1136/bmj.c6839.

van Everdingen, K. J., van der Grond, J., Kappelle, L. J., Ramos, L. M. and Mali, W. P. (1998). **Diffusion-weighted magnetic resonance imaging in acute stroke**. Stroke *29*, 1783-1790, doi: 10.1161/01.str.29.9.1783.

van Nimwegen, L. W. E., Mavinkurve-Groothuis, A. M. C., de Krijger, R. R., Hulsker, C. C. C., Goverde, A. J., Zsiros, J. and Littooij, A. S. (2020). **MR imaging in discriminating between benign and malignant paediatric ovarian masses: a systematic review**. Eur Radiol *30*, 1166-1181, doi: 10.1007/s00330-019-06420-4.

Vernooij, F., Heintz, P., Witteveen, E. and van der Graaf, Y. (2007). **The outcomes of ovarian cancer treatment are better when provided by gynecologic oncologists and in specialized hospitals: a systematic review**. Gynecol Oncol *105*, 801-812, doi: 10.1016/j.ygyno.2007.02.030.

Wagner, F., Laun, F. B., Kuder, T. A., Mlynarska, A., Maier, F., Faust, J., Demberg, K., Lindemann, L., Rivkin, B., Nagel, A. M., Ladd, M. E., Maier-Hein, K., Bickelhaupt, S. and Bach, M. (2017). **Temperature and concentration calibration of aqueous polyvinylpyrrolidone (PVP) solutions for isotropic diffusion MRI phantoms**. PLoS One *12*, e0179276, doi: 10.1371/journal.pone.0179276.

Wilm, B. J., Nagy, Z., Barmet, C., Vannesjo, S. J., Kasper, L., Haeberlin, M., Gross, S., Dietrich, B. E., Brunner, D. O., Schmid, T. and Pruessmann, K. P. (2015). **Diffusion MRI with concurrent magnetic field monitoring**. Magnetic Resonance in Medicine *74*, 925-933, doi: 10.1002/mrm.25827.

Woodhams, R., Ramadan, S., Stanwell, P., Sakamoto, S., Hata, H., Ozaki, M., Kan, S. and Inoue, Y. (2011). **Diffusion-weighted Imaging of the Breast: Principles and Clinical Applications**. RadioGraphics *31*, 1059-1084, doi: 10.1148/rg.314105160.

Wu, D., Li, G., Zhang, J., Chang, S., Hu, J. and Dai, Y. (2014). **Characterization of breast tumors using diffusion kurtosis imaging (DKI)**. PLoS One *9*, e113240, doi: 10.1371/journal.pone.0113240.

Xin, G., Ke, C. and Xiaoguang, H. (2012). **An improved Canny edge detection algorithm for color image**. In IEEE 10th International Conference on Industrial Informatics (Beijing), doi: 10.1109/INDIN.2012.6301061.

Yue, W., Meng, N., Wang, J., Liu, W., Wang, X., Yan, M., Han, D. and Cheng, J. (2019). **Comparative analysis of the value of diffusion kurtosis imaging and diffusion-weighted imaging in evaluating the histological features of endometrial cancer**. Cancer Imaging *19*, 9, doi: 10.1186/s40644-019-0196-6.

Zhang, L., Tang, M., Min, Z., Lu, J., Lei, X. and Zhang, X. (2016). **Accuracy of combined dynamic contrast-enhanced magnetic resonance imaging and diffusion-weighted imaging for breast cancer detection: a meta-analysis**. Acta Radiol *57*, 651-660, doi: 10.1177/0284185115597265.

Zhou, W. P., Zan, X. Y., Liu, X., Sudarshan, S. K. P., Yang, S. D., Fang, X. M., Guo, Y. J. and Hu, X. Y. (2019). **Characterization of breast lesions using diffusion kurtosis model-based imaging: An initial experience**. J Xray Sci Technol, doi: 10.3233/xst-190590.

10 Publications and Personal Contribution

Parts of this thesis have been published in two peer-reviewed journal articles.

1. **Mlynarska-Bujny**, A., Bickelhaupt, S., Laun, F. B., König, F., Lederer, W., Daniel, H., Ladd, M. E., Schlemmer, H.-P., Delorme, S. and Kuder, T. A. (2020). **Influence of residual fat signal on diffusion kurtosis MRI of suspicious mammography findings**. Scientific Reports *10*, 13286, doi: 10.1038/s41598-020-70154-3.

The first publication provides the content for the following sections of this dissertation: 3.2, 4.3, 5.3, 6.2. As a first author of the article, I was responsible for data processing, statistical analysis, interpretation of the findings and preparation of the manuscript. The conducted research is a retrospective analysis based on the data collected in the prospective study (S-151/2014).

2. Mokry, T., **Mlynarska-Bujny, A.**, Kuder, T. A., Hasse, F. C., Hog, R., Wallwiener, M., Dinkic, C., Brucker, J., Sinn, P., Gnirs, R., Kauczor, H.-U., Schlemmer, H.-P., Rom, J. and Bickelhaupt, S. (2020). **Ultra-High-b-Value Kurtosis Imaging for Noninvasive Tissue Characterization of Ovarian Lesions**. Radiology *296*, 358-369, doi: 10.1148/radiol.2020191700.

The second publication provides the content for the following sections of this dissertation: 3.3, 4.4, 5.4, 6.3. As a co-author, I was responsible for data processing, statistical analysis and participated in the preparation of the manuscript. The publication was based on the data collected in the prospective study (S-337/2016).

Other publications:

Bickelhaupt, S., Paech, D., Laun, F. B., Steudle, F., Kuder, T. A., **Mlynarska, A**., Bach, M., Lederer, W., Teiner, S., Schneider, S., Ladd, M. E., Daniel, H., Stieber, A., Kopp-Schneider, A., Delorme, S. and Schlemmer, H. P. (2017a). **Maximum intensity breast diffusion MRI for BI-RADS 4 lesions detected on X-ray mammography**. Clin Radiol *72*, 900.e901-900.e908, doi: 10.1016/j.crad.2017.05.017.

Bickelhaupt, S., Steudle, F., Paech, D., **Mlynarska, A**., Kuder, T. A., Lederer, W., Daniel, H., Freitag, M., Delorme, S., Schlemmer, H. P. and Laun, F. B. (2017b). **On a fractional order calculus model in diffusion weighted breast imaging to differentiate between malignant and benign breast lesions detected on X-ray screening mammography**. PLoS One *12*, e0176077, doi: 10.1371/journal.pone.0176077.

Dreher, C., Kuder, T. A., König, F., **Mlynarska-Bujny, A**., Tenconi, C., Paech, D., Schlemmer, H. P., Ladd, M. E. and Bickelhaupt, S. (2020). **Radiomics in diffusion data: a test-retest, inter- and intra-reader DWI phantom study**. Clin Radiol *75*, 798.e713-798.e722, doi: 10.1016/j.crad.2020.06.024.

Mokry, T., Pantke, J., Mlynarska-Bujny, A., Hasse, F. C., Kuder, T. A., Schlemmer, H. P., Kauczor, H. U., Rom, J. and Bickelhaupt, S. (2021). **Diffusivity mapping of the ovaries: Variability of apparent diffusion and kurtosis variables over the**

menstrual cycle and influence of oral contraceptives. Magn Reson Imaging *80*, 50-57, doi: 10.1016/j.mri.2021.04.006.

Wagner, F., Laun, F. B., Kuder, T. A., **Mlynarska, A**., Maier, F., Faust, J., Demberg, K., Lindemann, L., Rivkin, B., Nagel, A. M., Ladd, M. E., Maier-Hein, K., Bickelhaupt, S. and Bach, M. (2017). **Temperature and concentration calibration of aqueous polyvinylpyrrolidone (PVP) solutions for isotropic diffusion MRI phantoms**. PLoS One *12*, e0179276, doi: 10.1371/journal.pone.0179276.

Acknowledgments

I would like to take this opportunity to extend my deepest appreciation and gratitude to all the people who have contributed to the successful completion of my doctoral journey.

First of all, I would like to express my sincere gratitude to my doctoral father Prof. Dr. Heinz-Peter Schlemmer for enabling and supporting my PhD thesis at DKFZ.

My exceptional gratitude is dedicated to PD Dr. Tristan Kuder and PD Dr. Sebastian Bickelhaupt for their supervisory roles in shaping my thesis and the support in completion of this work. Their expertise and guidance have significantly impacted the direction of my research.

I would also like to thank the colleagues from my group and other PhD students at DKFZ..

Furthermore, I would like to thank Dr. Theresa Mokry for our successful collaboration.

Lastly, my highest gratitude goes to my family, especially my husband, for their unwavering support.

Eidesstattliche Versicherung

1. Bei der eingereichten Dissertation zu dem Thema

Diffusion kurtosis imaging and diffusion-weighted imaging of suspicious breast and ovarian lesions: development of phantoms and optimized data evaluation routines

handelt es sich um meine eigenständig erbrachte Leistung.

2. Ich habe nur die angegebenen Quellen und Hilfsmittel benutzt und mich keiner unzulässigen Hilfe Dritter bedient. Insbesondere habe ich wörtlich oder sinngemäß aus anderen Werken übernommene Inhalte als solche kenntlich gemacht.

3. Die Arbeit oder Teile davon habe ich bislang nicht an einer Hochschule des In- oder Auslands als Bestandteil einer Prüfungs- oder Qualifikationsleistung vorgelegt.

4. Die Richtigkeit der vorstehenden Erklärungen bestätige ich.

5. Die Bedeutung der eidesstattlichen Versicherung und die strafrechtlichen Folgen einer unrichtigen oder unvollständigen eidesstattlichen Versicherung sind mir bekannt. Ich versichere an Eides statt, dass ich nach bestem Wissen die reine Wahrheit erklärt und nichts verschwiegen habe.

Ort und Datum

Unterschrift